Αναπαραγωγή ήχου μέσω παλμικών πηγών οπτικής διέγερσης

ΔΙΔΑΚΤΟΡΙΚΗ ΔΙΑΤΡΙΒΗ

ΚΩΝΣΤΑΝΤΙΝΟΥ ΚΑΛΕΡΗ

ΤΜΗΜΑ ΗΛΕΚΤΡΟΛΟΓΩΝ ΜΗΧΑΝΙΚΩΝ & ΤΕΧΝΟΛΟΓΙΑΣ ΥΠΟΛΟΓΙΣΤΩΝ
ΠΑΝΕΠΙΣΤΗΜΙΟ ΠΑΤΡΩΝ

ΑΡΙΘΜΟΣ ΔΙΑΤΡΙΒΗΣ 387

ΠΑΤΡΑ – ΙΟΥΛΙΟΣ 2021

Πανεπιστήμιο Πατρών, Τμήμα Ηλεκτρολόγων Μηχανικών & Τεχνολογίας Υπολογιστών
Κωνσταντίνος Καλέρης

Sound reproduction from laser-driven pulsed acoustic sources

PhD Dissertation

KONSTANTINOS KALERIS

Department of Electrical and Computer Engineering
University of Patras

Patras – July 2021

Πιστοποίηση

Πιστοποιείται ότι η παρούσα διατριβή με θέμα:

«Αναπαραγωγή ήχου μέσω παλμικών πηγών οπτικής διέγερσης»

του Κωνσταντίνου Καλέρη, διπλωματούχου του Τμήματος Ηλεκτρολόγων Μηχανικών και Τεχνολογίας Υπολογιστών του Πανεπιστημίου Πατρών, παρουσιάστηκε δημοσίως στο Τμήμα Ηλεκτρολόγων Μηχανικών και Τεχνολογίας Υπολογιστών του Πανεπιστημίου Πατρών στις 28 Ιουλίου 2021 και εξετάστηκε και εγκρίθηκε από την ακόλουθη Εξεταστική Επιτροπή:

Ιωάννης Μουρτζόπουλος	Καθηγητής Πανεπιστημίου Πατρών, Επιβλέπων Καθηγητής
Θεόδωρος Αντωνακόπουλος	Καθηγητής Πανεπιστημίου Πατρών, Μέλος Συμβουλευτικής Επιτροπής
Νεκτάριος Παπαδογιάννης	Καθηγητής Ελληνικού Μεσογειακού Πανεπιστημίου, Τμήμα Μουσικής Τεχνολογίας και Ακουστικής, Μέλος Συμβουλευτικής Επιτροπής
Ville Pulkki	Καθηγητής Πανεπιστημίου Aalto (Φινλανδία), Τμήμα Επεξεργασίας Σήματος και Ακουστικής
Μιχαήλ Ταταράκης	Καθηγητής Ελληνικού Μεσογειακού Πανεπιστημίου, Τμήμα Ηλεκτρονικών Μηχανικών
Πηνελόπη Μενούνου	Αναπλ. Καθηγήτρια Πανεπιστημίου Πατρών, Τμήμα Μηχανολόγων και Αεροναυπηγών Μηχανικών

Ο Επιβλέπων Καθηγητής

Ιωάννης Μουρτζόπουλος

Ο Πρόεδρος του Τμήματος

Οδυσσέας Κουφοπαύλου

To my parents, Vassilios and Ekaterini and my brother Aristotelis.

Acknowledgements

This PhD Thesis was conducted in the Audio and Acoustic Technology Group (Audio Group) of the Wire Communications Laboratory of the Electrical and Computer Engineering Department of the University of Patras. I am thankful to Professor Mourjopoulos for entrusting me with his insightful scientific ideas that led to this work. I also thank him for his restless and motivating steering of my research activities and efforts, as well as for the stimulating and versatile working environment in the Audio Group. Finally, I thank him for instilling into me valuable scientific, ethical and educational principles and vision necessary to pursue a fulfilling standalone scientific or professional mission in the future. There was not a single day in these five years that he was not a great support to me.

I am thankful to Professor Nektarios Papadogiannis for entrusting me with his scientific ideas that led to parts of this work, as well as for inviting me to the facilities of the Institute of Plasma Physics and Lasers (IPPL) of the Hellenic Mediterranean University (HMU) in Crete. I mostly thank him though for the creative working atmosphere and the vast amount of time he invested in our discussions about physical aspects of my work and other projects, future research ideas and potential ventures. His dedication to the deep understanding of physical phenomena has been a constant motivation for me.

From the group of IPPL, I would like to specially thank Dr. Yannis Orphanos for his technical and scientific support that was crucial for the realization of the experiments and also for his hospitality that enabled my repeated visits to Rethymnon. Furthermore, I thank Assoc. Professor Makis Bakarezos for the useful scientific discussions and his regular assistance in the experiments carried out in the laboratories of IPPL, Assoc. Professor Vasilios Dimitriou for the discussions on computational and physical modeling aspects of this work and Professor Michael Tatarakis for the useful discussions and for enabling the access to the experimental facilities of the IPPL. Finally, I thank Stelios Petrakis for his technical and scientific support in the experiments, as well as Ioannis Tazes for his support and several sleepless nights during the development of the PIC model.

Crucial support in the experimental parts of this work was provided by the Engler Bunte Institute (EBI) of the Karlsruhe Institute of Technology (KIT). I warmly thank Professor Dimosthenis Trimis for enabling me to carry out experiments in the facilities of the EBI but also for the useful discussions and ideas on engineering aspects of the developed laser-sound system. I also thank him for his hospitality that allowed me to visit Karlsruhe for several months. Moreover, I thank Dr. Björn Stelzner for his contribution in the planning and execution of the experiments on the developed laser-sound system and for making the best possible to provide the necessary high-specifications equipment.

From the Audio Group, I thank Dr. Panagiotis Hatziantoniou for his support in signal processing aspects of this work. I also feel grateful to Dr. Photis Kontomichos, Dr. Charalampos Papadakos and Gavriil Kamaris for the great working environment, as well as for their scientific support.

I would like to thank Professor Emmanuil Psarakis for the very interesting and motivating discussions on stochastic signals and processes and his significant contribution to our ongoing common work.

I would like to thank the supervisor of my Diploma Thesis, Professor Emeritus Demetris P.K. Ghikas for closely following my scientific steps all these years and for advising me every time I asked.

I would like to thank Professor Theodore Antonakopoulos, my father Professor Emeritus Vassilios Kaleris, and Hristina Delibašić for the useful discussions on aspects of this work.

Finally, I would like to thank my parents Vassilios and Ekaterini Kaleri for introducing me to scientific thinking and ethics, due to which I feel privileged in my work. I also thank them for their immense psychological support, motivation and consistency throughout this educational phase that comes to an end with the completion of this thesis.

Contents

Chapter 3

Chapter 4

Chapter 5

Chapter 6

Chapter 7

Εκτενής ελληνική περίληψη

Στην εργασία αυτή παρουσιάζονται νέα ευρήματα σχετικά με την αναπαραγωγή ήχου από ακουστικές πηγές πλάσματος παραγόμενου από λέιζερ. Διερευνώνται θεμελιώδη θέματα φυσικής της οπτοακουστικής μετατροπής μέσω πλάσματος λέιζερ, καθώς και η αξιοποίησή της για τη ανάπτυξη ενός πρωτότυπου μετατροπέα πλάσματος-λέιζερ (laser-sound) ικανού να αναπαράγει σύνθετα ηχητικά σήματα με γραμμικό και ελεγχόμενο τρόπο.

Η διεπιστημονική προσέγγιση στην οπτοακουστική μετατροπή ήχου οδήγησε στην ανάπτυξη συμπαγών φαινομενολογικών μοντέλων για την περιγραφή της ακουστικής εκπομπής των πηγών ήχου πλάσματος λέιζερ στον ατμοσφαιρικό αέρα. Παρά την σχετική απλότητά τους, τα μοντέλα αυτά επιτρέπουν την ακριβή εκτίμηση των χαρακτηριστικών της ακτινοβολίας λέιζερ που απαιτούνται για την επίτευξη ενός συγκεκριμένου ακουστικού αποτελέσματος, αλλά και την παροχή μιας διαφορετικής, και πολλές φορές διεισδυτικής, προοπτικής στις φυσικές διαδικασίες. Επιπλέον, η μελέτη παλμικών ηχητικών σημάτων για την οδήγηση του μετατροπέα ήχου λέιζερ οδήγησε στην ανάπτυξη μιας νέας μεθόδου για τον υπολογισμό και την ανάλυση των συχνοτικών φασμάτων των σημάτων κατά Uniform-sampling Pulse Width Modulation (UPWM) διαμορφωμένων σημάτων που προέρχονται από στοχαστικά σήματα εισόδου.

Έτσι, η συμβολή της παρούσας διπλωματικής εργασίας μπορεί να χωριστεί σε τρεις κατευθύνσεις:

1. διερεύνηση και μοντελοποίηση φυσικών πτυχών της παραγωγής ήχου πλάσματος λέιζερ
2. σχεδιασμός, ανάπτυξη και αξιολόγηση ενός νέου πρωτοτύπου μορφοτροπέα ήχου λέιζερ
3. μελέτη του φάσματος DFT των σημάτων UPWM που προέρχονται από τυχαία σήματα εισόδου

Το Κεφάλαιο 1 είναι εισαγωγικό και παρέχει το επιστημονικό και τεχνολογικό πλαίσιο της εργασίας, μια περιγραφή των σύγχρονων συστημάτων αναπαραγωγής ήχου βασισμένων σε ηλεκτρομηχανικούς μετατροπείς, τα βασικά σημεία συνεισφοράς της εργασίας, τα επιστημονικά άρθρα, τις ανακοινώσεις σε συνέδρια, την ευρεσιτεχνία και τις διακρίσεις που προέκυψαν στα πλαίσια της εργασίας αυτής, καθώς και την δομή της.

Στο Κεφάλαιο 2 παρουσιάζονται οι βασικές αρχές της παραγωγής πλάσματος λέιζερ στον αέρα ή σε στερεά. Για το σκοπό αυτό, σκιαγραφείται ένα μαθηματικό μοντέλο που περιγράφει τη διάδοση παλμών λέιζερ και την απορρόφηση οπτικής ενέργειας, μαζί με τις εξισώσεις ρυθμού που περιγράφουν τη δημιουργία ελεύθερων ηλεκτρονίων. Για τη διάδοση του παλμού θεωρείται γραμμική Γκαουσιανή εστίαση από φακό, ενώ τα μη-γραμμικά φαινόμενα της απο-εστίασης πλάσματος και της αυτο-εστίασης λόγω του οπτικού φαινομένου Kerr περιλαμβάνονται επίσης μέσω του μη-γραμμικού δείκτη διάθλασης. Επίσης, συζητούνται οι διαφορετικοί μηχανισμοί διάσπασης αερίων υπό την επίδραση βραχέων (νανοδευτερολέπτων) και υπερβραχέων (φεμτοδευτερολέπτων) παλμών λέιζερ ενώ αποτυπώνεται και η επίδρασή τους στις εξισώσεις ρυθμού παραγωγής ηλεκτρονίων. Επιπλέον, σε αυτό το κεφάλαιο περιγράφονται οι μηχανισμοί πίσω από τα δευτερεύοντα φαινόμενα ακτινοβολίας μετά από διάσπαση αερίων από λέιζερ, και συγκεκριμένα η εκπομπή ενός ηχητικού και ενός οπτικού παλμού. Τονίζεται η θερμοελαστική φύση της παραγωγής ήχου κατά τη διάσπαση λέιζερ και περιγράφονται οι διαδικασίες που εμπλέκονται στη μεταφορά ενέργειας από τα ελεύθερα ηλεκτρόνια στα βαριά σωματίδια του ιονισμένου όγκου. Αναλύονται οι διάφορες διαδικασίες εκπομπής φωτεινής ακτινοβολίας, όπως η σκέδαση (deflection) ηλεκτρονίων από βαριά σωματίδια (Bremsstrahlung), η επανασύνδεση και αποδιέγερση ηλεκτρονίων καθώς και η θερμική ακτινοβολία. Τέλος, παρουσιάζονται οι κύριες επιστημονικές και τεχνολογικές εφαρμογές της παραγωγής ήχου από πλάσμα λέιζερ, εστιάζοντας σε εφαρμογές που σχετίζονται με την ακουστική.

Στο Κεφάλαιο 3 καλύπτονται βασικά θέματα της τρέχουσας τεχνολογίας αναπαραγωγής ήχου καθώς και βασικές έννοιες των παλμικών διαμορφώσεων ήχου που χρησιμοποιούνται ευρέως στα σύγχρονα συστήματα αναπαραγωγής ήχου. Επιπλέον, σκιαγραφείται η δομή μιας αλυσίδας αναπαραγωγής ήχου που βασίζεται σε μορφοτροπέα πλάσματος λέιζερ και συγκρίνεται με τις σύγχρονες αλυσίδες ενίσχυσης και αναπαραγωγής ήχου κατηγορίας D (class D). Πιο συγκεκριμένα, παρουσιάζονται οι βασικές έννοιες των πλέον διαδεδομένων τύπων παλμικών διαμορφώσεων ήχου, και συγκεκριμένα της ΣΔ διαμόρφωσης της διαμόρφωσης εύρους παλμού, και της διαμόρφωσης πλάτους παλμού, οι οποίες χρησιμοποιούνται στα τρέχοντα συστήματα αναπαραγωγής ήχου που βασίζονται σε ενισχυτές κατηγορίας D, ενώ έχουν ενδιαφέρον και για την ανάπτυξη μετατροπέων ήχου πλάσματος λέιζερ. Παρουσιάζονται αναλυτικά οι αναπαραστάσεις στο πεδίο του χρόνου και της συχνότητας των διαμορφώσεων αυτών και δίνεται έμφαση στη διάκριση των συχνοτήτων εντός ζώνης και εκτός ζώνης των διαμορφωμένων σημάτων. Επιπλέον, αναπτύσσεται μια νέα μέθοδος για την ανάλυση και τον υπολογισμού των φασματικών γραμμών σημάτων PWM με ομοιόμορφης δειγματοληψίας (UPWM) που προέρχονται από τυχαία σήματα εισόδου. Ειδικότερα, αποδεικνύεται ότι οι φασματικές γραμμές τέτοιων σημάτων στην εκτός ζώνης περιοχή μπορούν να υπολογιστούν απευθείας από τα στατιστικά της γεννήτριας διαδικασίας του σήματος εισόδου. Κατά αυτόν τον τρόπο προκύπτει ότι η μέθοδος επιτρέπει την εκτίμηση των φασματικών γραμμών των UPWM σημάτων χωρίς γνώση της συγκεκριμένης χρονοσειράς του σήματος εισόδου, δεδομένου ότι η γεννήτρια τυχαία διαδικασία είναι εργοδική. Τέλος, παρουσιάζονται εκφράσεις κλειστής μορφής για τους φασματικούς συντελεστές όταν τα δείγματα του σήματος εισόδου ακολουθούν κοινές κατανομές όπως Γκαοουσιανή, Λαπλασιανή, αντίστροφου ημιτόνου και ομοιόμορφη.

Στο Κεφάλαιο 4 παρουσιάζεται μια συνδυαστική προσέγγιση βασισμένη σε πείραμα, φυσική μοντελοποίηση και επεξεργασία σήματος για τη μελέτη και περιγραφή της ηχητικής εκπομπής σφαιρικών πηγών πλάσματος λέιζερ. Αναπτύσσεται ένα νέο φαινομενολογικό μοντέλο που επιτρέπει την εκτίμηση του συχνοτικού φάσματος των ηχητικών κυμάτων που παράγουν οι ακουστικές πηγές πλάσματος από το προφίλ του θερμικού φωτός που εκπέμπεται από τον διεγερμένο όγκο του αερίου, αναδεικνύοντας με σαφή τρόπο τη συσχέτιση μεταξύ δευτερογενούς οπτικής και ηχητικής εκπομπής που ακολουθεί τη διάσπαση αερίων από λέιζερ. Για την εξαγωγή του θερμικού φωτός από τη συνολική ακτινοβολία του διεγερμένου όγκου χρησιμοποιήθηκαν τεχνικές επεξεργασίας σήματος βασισμένες στη φυσική των διαφορετικών διαδικασιών δευτερογενούς οπτικής εκπομπής. Οι προβλέψεις του μοντέλου επιβεβαιώνονται μέσω σύγκρισης με τα αποτελέσματα σχετικών ακουστικών μετρήσεων. Επιπλέον μελετάται η επίδραση της ενέργειας του παλμού λέιζερ στις χρονικές κλίμακες των φαινομένων ακτινοβολίας μέσω πειραματικών μετρήσεων και προσομοιώσεων. Από την μελέτη προκύπτει ότι ένας ισχυρότερος παλμός λέιζερ οδηγεί σε εντονότερο, και, κυρίως, μεγαλύτερο σε διάρκεια, θερμικό φαινόμενο. Το γεγονός αυτό έχει άμεσο αντίκτυπο στα φάσματα των παραγόμενων ακουστικών παλμών. Συγκεκριμένα παρατηρείται μια φασματική μετατόπιση προς τις χαμηλότερες συχνότητες με την αύξηση της ενέργειας παλμών λέιζερ, η οποία μπορεί να σχετίζεται με τη διάρκεια των διαδικασιών οπτικής ακτινοβολίας και τη συνολική θερμότητα που μεταφέρεται από το λέιζερ στον όγκο αλληλεπίδρασης με τον αέρα.

Στο Κεφάλαιο 5 μελετάται πειραματικά και αναλυτικά η εκπομπή ήχου από νήματα πλάσματος λέιζερ. Παρουσιάζονται συστηματικές μετρήσεις της ηχητικής εκπομπής νήματος πλάσματος μήκους 14 εκατοστών, δημιουργούμενου από παλμούς λέιζερ 23 φεμτοδευτερολέπτων και ενέργειας 5 mJ. Αναπτύσσεται ένα ακουστικό μοντέλο βασισμένο στο κλασικό μοντέλο γραμμικής ακουστικής πηγής (line source), μέσω του οποίου υπολογίζεται η ακουστική εκπομπή των νημάτων πλάσματος στον τρισδιάστατο χώρο συναρτήσει της χωρικής κατανομής της εναποτιθέμενης οπτικής ενέργειας. Αποδεικνύεται ότι η γεωμετρία του πλάσματος και η κατανομή της αξονικής πίεσης μπορούν να προσδιοριστούν από το χωρικό προφίλ της οπτικής ακτινοβολίας του νήματος πλάσματος. Οι προβλέψεις του μοντέλου επικυρώνονται μέσω σύγκρισης με ακουστικές μετρήσεις, δείχνοντας πολύ καλή συμφωνία. Το μοντέλο γραμμικής ακουστικής πηγής χρησιμοποιείται για τη μελέτη της εξάρτησης της ακουστικής εκπομπής νημάτων πλάσματος από τα γεωμετρικά χαρακτηριστικά του καναλιού πλάσματος, και συγκεκριμένα το μήκος του καναλιού και την αρχική κατανομή πίεσης κατά μήκος του άξονα του νήματος. Τέλος, περιγράφεται ένα φυσικό μοντέλο της ακουστικής εκπομπής νημάτων λέιζερ βάση του γραμμικού μοντέλου θερμικής πηγής του Κεφαλαίου 4. Παρουσιάζονται προκαταρκτικά αποτελέσματα από την προσομοίωση ενός υπό κλίμακα μοντέλου νήματος πλάσματος, από όπου αποδεικνύεται ότι ένα τέτοιο μοντέλο μπορεί να αποτυπώσει επιτυχώς τα κατευθυντικά χαρακτηριστικά της ακουστικής εκπομπής του νήματος.

Στο Κεφάλαιο 6 παρουσιάζονται οι βασικές αρχές καινοτόμου τεχνολογίας αναπαραγωγής ήχου από λέιζερ, ενώ περιγράφεται και αξιολογείται πειραματικά και υπολογιστικά πρωτότυπος οπτοακουστικός μετατροπέας πλάσματος λέιζερ. Ο μετατροπέας επιτυγχάνει αναπαραγωγή ηχητικών σημάτων διαμορφωμένων μέσω διαμόρφωσης ΣΔ ενός ή πολλών bit, οι οποίες μετατρέπονται σε ροές ακουστικών παλμών απευθείας στον ατμοσφαιρικό αέρα ή πάνω σε μεταλλικούς στόχους. Το πρωτότυπο έχει εύρος ζώνης 1kHz, το οποίο επαρκεί για να αποδείξει την λειτουργία του συστήματος, ενώ αποδεικνύεται επίσης ότι η επίτευξη λειτουργίας στο πλήρες ακουστικό εύρος συχνοτήτων είναι εξαρτάται μόνο από τις προδιαγραφές του λέιζερ. Παρουσιάζονται πειραματικά αποτελέσματα από την αναπαραγωγή δοκιμαστικών ηχητικών σημάτων, όπως μεμονωμένα ή πολλαπλά ημίτονα, καθώς και πραγματικά ηχητικά σήματα ομιλίας και μουσικής. Επιπλέον, αναπτύσσεται ένα υπολογιστικό μοντέλο προσομοίωσης οποιουδήποτε συστήματος αναπαραγωγής ήχου πλάσματος λέιζερ βασισμένου σε διαμόρφωση ΣΔ, συναρτήσει των παραμέτρων του λέιζερ και της διαμόρφωσης. Το μοντέλο λαμβάνει ως είσοδο το αρχικό ηχητικό σήμα και προβλέπει το αναπαραγόμενο σήμα μέσω συνέλιξης της ΣΔ αναπαράστασής του με το προφίλ πίεσης ενός ακουστικού παλμού πλάσματος λέιζερ. Οι προβλέψεις του μοντέλου επιβεβαιώνονται μέσω σύγκρισης με τις πειραματικές μετρήσεις. Επιπλέον, μέσω του μοντέλου προσομοιώνεται η ακουστική εκπομπή ενός ιδανικού συστήματος ήχου λέιζερ που καλύπτει το πλήρες ακουστό φάσμα συχνοτήτων. Το σύστημα βασίζεται σε διαμόρφωση ΣΔ 6-τάξης 5-bit με υπερδειγματοληψία x8, και ρυθμό επανάληψης λέιζερ 352,8 kHz, παρέχοντας συνολικό λόγο σήματος προς θόρυβο κβαντισμού 88,57dB. Το σύστημα περιλαμβάνει επίσης κατάλληλη προεπεξεργασία σήματος για την επίτευξη ισοσταθμισμένης απόκρισης συχνότητας μέσα στη συχνοτική ζώνη ενδιαφέροντος, αναδεικνύοντας τη δυνατότητα σχεδιασμού ιδανικών συστημάτων αναπαραγωγής ήχου μέσω πηγών πλάσματος λέιζερ. Τέλος, γίνεται ανάλυση της ενεργειακής απόδοσης του πρωτότυπου και του ιδανικού συστήματος αναπαραγωγής ήχου, και τα αποτελέσματα συγκρίνονται με την απόδοση των σύγχρονων ηλεκτρομηχανικών μετατροπέων.

Τέλος, στο Κεφάλαιο 7 συνοψίζονται τα κεντρικά αποτελέσματα και ευρήματα της εργασίας, παρουσιάζονται οι μακροπρόθεσμοι στόχοι και το όραμα της παρούσας έρευνας, ενώ επίσης αναλύονται τα επόμενα ερευνητικά βήματα και τα ανοιχτά θέματα που πρόκειται να διερευνηθούν στο άμεσο μέλλον.

Abstract

This work presents novel findings on sound reproduction from laser-generated plasma acoustic sources. It addresses fundamental aspects of the physics behind laser-based optoacoustic transduction as well as engineering aspects for the utilization of the laser-plasma transduction mechanism in the development of audio reproduction systems. It presents a joint experimental, theoretical and signal processing approach for the study and modeling of sound radiation from spherical, omnidirectional but also cylindrical, directional laser-plasma sound sources. Based on experimental findings, a novel phenomenological model is developed that allows for the estimation of the frequency spectra of the plasma-generated sound waves in terms of the thermal light emitted by the heated volume, clearly demonstrating the correlation between secondary light and sound radiation following laser-induced breakdown of gases. The model's predictions are validated by comparison with acoustic measurements, showing good agreement. Also, an acoustic model based on the classical acoustic line source model is developed that calculates the acoustic radiation of plasma filaments in 3D space in terms of the spatial distribution of the deposited optical energy. It is shown that the plasma geometry and axial pressure distribution can be determined by the spatial profile of the thread's luminescence. The model's predictions are validated by comparison with acoustic measurements, showing very god agreement. Moreover, the concepts of a novel laser-sound technology are presented and a laser-based optoacoustic transducer prototype is described and experimentally evaluated. The prototype is capable of generating 1-bit or multibit ΣΔ optical pulse streams, that are transduced into acoustic pulse streams directly in the ambient air or on metal targets. The presented prototype has an effective bandwidth of 1kHz, which is sufficient for the proof-of-concept demonstration of the technology, while it is shown that generalization of the results towards a wider frequency range, such as the audible range, is a matter of laser specifications. Experimental results from the reproduction of bandlimited test signals, such as single or multiple sine waves and sine sweeps, as well as real audio signals, particularly speech and music, are presented. Moreover, a computational model is developed that allows for the simulation of any ΣΔ-base laser-driven sound reproduction system, in terms of the laser and modulation parameters. The model takes as input the original sound signal and transforms it into the desired modulation signal via convolution of its ΣΔ representation with the pressure profile of a single laser-generated acoustic pulse. The model's predictions are validated by comparison with the experimental measurements, showing good agreement. Finally, ongoing work on a complete physical model of the energy deposition through optical breakdown of gases is outlined and a new method for the prediction of the frequency spectra of uniform-sampling Pulse Width Modulation signals originating from random modulating signals is demonstrated.

Chapter 1

Introduction

Contents

Foreword

This Thesis brings together well-established digital audio conversion techniques and the physics of sound generation via laser plasma acoustic sources to introduce a novel laser-based technology for sound reproduction from pulsed, massless plasma sound sources in the air or on solid targets. Transformations of analog or digitally sampled audio signals to digital pulse streams are combined with the strongly non-linear optoacoustic transduction mechanism of laser plasma generation to synthesise a prototype laser-sound transducer able to reproduce arbitrarily complex sound signals in a highly linear and predictable manner.

Moreover, this Thesis is the result of fruitful collaborations between three research groups with diverse scientific expertise:

- The Audio and Acoustic Technology Group (Audiogroup) of the Electrical and Computer Engineering department of the University of Patras, Greece, with expertise in audio signal processing and sound transduction
- The Institute of Plasma Physics and Lasers (IPPL) of the Hellenic Mediterranean University, Greece, with expertise in laser-plasma physics and applications
- The Verbrennungstechnik division of the Engler-Bunte Institute (EBI-vbt) of the Karlsruher Institute of Technology (KIT), Germany, with expertise in combustion shock waves and laser measurement techniques

This collaboration enabled and supported the PhD candidate to utilize the complementary expertise of these research groups via in-situ experiments, exchange of knowledge and remote cooperation.

The interdisciplinary approach to laser plasma sound transduction has led to the development of compact phenomenological models for the description of the acoustic radiation of laser plasma sound sources in ambient air. Despite their simplicity, such physical models allow for highly accurate estimations of the laser radiation characteristics required to achieve a particular acoustic result, but also to provide a different, potentially insightful, perspective on the involved physical processes themselves. Also, the study of pulsed audio signals for driving the laser-sound transducer led to the development of a novel method for the calculation and analysis of the DFT spectra of Uniform-sampling Pulse Width Modulation (UPWM) signals derived from random modulating signals.

Thus, the contribution of this Thesis can be divided in three directions:

a. The investigation and modeling of physical aspects of laser plasma sound generation
b. The engineering, implementation and evaluation of a novel laser-sound prototype transducer
c. The study of the DFT spectrum of UPWM signals derived from random input signals

The physical and technological framework, the main achievements and the structure of this Thesis are presented in the next sections of this Chapter.

1.1 Framework and motivation

Currently, sound reproduction in the audible frequency range relies on transducer technology that was established more than 100 years ago. The technology is mainly based on the electromagnetic moving coil loudspeakers [1], since alternative implementations, such as electrostatic [2], piezoelectric [3], thermoacoustic [4][5] and voltage-driven plasma loudspeakers [6], do not constitute viable solutions for most audio reproduction applications. However, the acoustic power, directivity, response, efficiency and controllability of the traditional electroacoustic loudspeakers are significantly limited, mainly due to: (a) the weak coupling of the moving-coil electromechanical driver to the low density air medium, (b) the inability to digitally control and directly transcode audio data into acoustic waves, (c) the requirement for local electric power supply to drive low-efficiency transducer units, (d) the need for multiple and distant transducers to achieve controlled spatial reproduction from distributed sound sources.

In the past, merging optics and acoustics technologies has led to important breakthroughs, such as optical disc technology (first as the Compact Disc Digital Audio) [7], thermoacoustic imaging [8] and spectroscopy [9], laser induced breakdown spectroscopy (LIBS) [10], optical wave microphone [11]. Although research prototypes of DVD and Blu-Ray optical drives needed expensive room-filling laser equipment, commercialization of such systems led to widespread, ultra-compact and inexpensive pick-up devices. In a similar manner, the proposed technological breakthroughs could allow compact laser-based devices for audio delivery at home, public spaces and over long distances in the atmosphere even potentially to generate ablation-based sound to the surface of a distant object, car, a boat or a remote target in space. Ultimately, the marriage between photonics and acoustics is envisaged to provide a novel and scalable means of generating audio signals for future consumer and professional applications.

Air breakdown by focusing of short or ultra-short laser pulses of sufficient energy leads to the generation of strong non-linear sound waves (shock waves), that progressively transform into linear sound waves as they propagate outwards the focusing area [12][13]. The particular properties of laser-generated sound waves, such as duration, energy, frequency spectrum and other, strongly depend on the characteristics of the optical excitation source, for example optical pulse duration (nanosecond to femtosecond), energy, wavelength and focusing conditions. Regardless of the possible differences, laser-generated sound waves are very abrupt and are often referred to as N-pulses, due to their shape in the time domain. The pulses exhibit high acoustic energy in the ultrasonic regime, but also have significant energy in the lower frequencies, which renders them also useful for audio applications [14][15][16][17].

Although no implementation or model for the laser-driven reproduction of complex continuous sound was presented so far, such a technology could be practically feasible. The pulsed nature of the laser-generated acoustic waves indicates the need for a digital audio modulation to transcode complex sound signals, in analogy to the well-established pulse streams used by digital audio systems. Pulse modulations such as Pulse Width Modulation (PWM) [18][19] and Sigma-Delta Modulation [20][21] (SDM or ΣΔ modulation) are extensively used in contemporary audio devices, for example in audio amplifiers [22][23], embedded audio processors [20][24] and Digital to Analog converters [24]. Particularly, ΣΔ modulation is widely used in analog-to-digital (ADC) and digital-to-analog (DAC) conversion, transmission and storage of audio data [26][27]. In the ΣΔ modulation, the analog or digital input audio signal is converted into a stream of rectangular pulses or a bit stream, when considering an analog or digital modulator output, respectively. The encoding can be either 1-bit or k-bit, the latter corresponding to pulses with $2^k - 1$ possible amplitudes. The information of the modulating audio signal, particularly the changes in its amplitude, is encoded in the ΣΔ signal as a pulse density that varies with time. ΣΔ modulation requires oversampling to distribute the quantization noise across a wide frequency range, which extends well beyond the frequency range of the input signal, hereafter referred to as inband range or band of interest). Additionally, a high-pass spectral profile of the quantization noise is achieved via noise shaping [20], resulting in a further reduction of the quantization noise energy within the band of interest. The noise shaping profile depends on the order of the modulator, where a higher order corresponds to a reduced total inband noise energy and a steeper slope of the high-pass profile (see ΣΔ modulator structure subsection).

These processes enable the generation of virtual massless sound sources, which can potentially be formed at arbitrary positions and distances from the driving laser unit with high localization precision. Moreover, modulated trains of laser pulses emitted by appropriate triggering of the laser can carry complex sound information and the optical power required for the transduction to strong acoustic waves at the desired position in space. Laser-driven sound waves can be very rapid and strong, while they enable the rendering of moving virtual sound sources in space by real-time shifting of the laser focal spot within the possible beam-focusing area. The generated acoustic pulse trains enable the direct reproduction of digital sound streams without the need for digital-to-analog conversion, allowing for all-digital audio reproduction chains. Indicative 1-bit and multibit laser-sound chains are shown in Fig. 1.1 a) and b), respectively, where EOM represents the Electro-Optic Modulation stage required for amplitude modulation of the laser pulses. The laser-sound transduction chains are further analyzed in Chapter 3. In

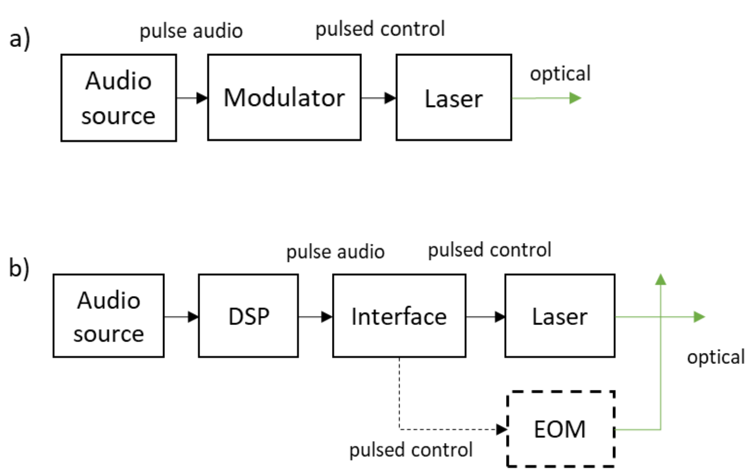

Fig. 1.1: Block diagram of typical laser-sound reproduction chain based on a) 1-bit and b) multibit ΣΔ audio modulation.

addition, laser-generated sound sources do not involve moving parts and as demonstrated in the next section, they exhibit well-defined and stable frequency response which is not subject to constructional or material defects.

1.2 Contribution

This Thesis contributes to the study and modeling of physical aspects of sound generation via laser-induced breakdown in ambient air, as well as to the technological exploitation of laser plasma generation for the development of laser-sound transducers capable of reproducing complex continuous sound via massless moving sources with potential directivity control.

1.2.1 Laser-plasma sound emission

Regarding the physical aspects, a clear experimental and analytical demonstration of the correlation between light and sound following laser induced breakdown is presented, as well as its utility in the development of qualitative phenomenological models describing the acoustic radiation of laser plasma sound sources with varying spatio-temporal energy distributions. Both the experiments and the development of the computational models was carried out in collaboration with the Institute of Plasma Physics and Lasers (IPPL) of the Hellenic Mediterranean University (HMU).

1.2.1.1 Correlation between light and sound secondary radiation

Measurements
Methodology for simultaneous measurements of the light and sound signals following LIB of the ambient air from tightly focused, few-millijoules nanosecond pulses over large observation windows that uncover the evolution of the radiative processes in their full extent, from the early times of the plasma formation until its complete relaxation.

Signal processing
Novel physics-driven signal processing technique enabling the time-domain analysis of the LIB secondary light radiation to its constituents, based on the diverse physical processes involved. The analysis provides a clear profiling of the mechanisms behind the emission of light and sound during laser-induced breakdown through their signal fingerprints.

Light-sound correlation and model
Calculation of the frequency spectra of the generated N-pulses [28] directly from the thermal radiation component of the optical signal. This is done by adopting a linear wave equation model in which the extracted thermal component is introduced as a heat source. The model's estimations on the frequency spectra of the LIB acoustic pulses show good agreement with the frequency spectra derived from

corresponding acoustic measurements. In this manner, the relation between the secondary phenomena accompanying laser-induced breakdown in gases is demonstrated.

Analysis of LIB frequency spectra

The characteristic acoustic spectrum of the N-pulses with a global spectral peak and consequent dip, followed by alternating local peaks and dips are accurately reproduced by the thermal model. Moreover, the dependence of the duration of the thermal phenomenon on the laser pulse energy and its impact on the respective acoustic spectrum, are clearly identified, with an increase in the optical energy leading to a spectral shift of the acoustic N-pulses towards the lower frequencies.

1.2.1.2 Sound emission of plasma filaments

This Thesis also demonstrates how such a correlation between light and sound following LIB can be exploited for the development of acoustic models of the sound radiation of plasma sound sources, in the case of laser filaments [29].

Adapted acoustic line source model

It is shown that the acoustic radiation of laser filaments can be effectively estimated through a modified model of the classical acoustic line source [30], in which, the pressure profile of the elementary source excitation is substituted with the pressure profile of an N-wave generated by a point-like laser plasma source. The initial pressure distribution along the axis of the line source can be derived from the luminescent light emitted by the filament. This simple model succeeds in reproducing the acoustic directivity and the frequency spectra of the radiation of plasma filaments with sufficient accuracy, as proven by comparison to experimental evaluations.

Acoustic directivity and spectrum analysis

The general characteristics of the acoustic directivity and frequency spectra of plasma filaments in ambient air are studied experimentally and analytically in both the full observation spectrum as well as in the audio range and in octave bands.

Radiation dependence on geometrical characteristics

The adapted acoustic line source model is used to systematically study the dependence of the acoustic radiation of plasma filaments on their geometrical characteristics, particularly their length and pressure distribution along the filament's axis. It is clearly demonstrated that the decisive parameter is the length of the plasma channel, while the initial pressure distribution along its axis has a mild impact within the studied parameter space.

Radiation physical model

Finally, this work proposes a complete computational model for the estimation of the acoustic radiation of plasma filaments, based on the wave equation with a heat source. It presents preliminary results from the evaluation of a scaled model of the filament, indicating the model's capability to capture the main characteristics of the filament's acoustic radiation. However, a rigorous validation of the model is left as future work.

1.2.2 Laser-sound optoacoustic transduction

In the engineering part of this Thesis, a novel optoacoustic transducer prototype is presented that is capable of reproducing arbitrarily complex, continuous and controlled sound signals via laser-induced breakdown directly in the air or via laser ablation on metal targets. The transducer was developed in the laboratories of the Engler-Bunte Institute of the Karlsruher Institute of Technology and is based on a single laser unit that can emit high-energy laser pulses at high repetition rates, consecutively causing laser breakdown in the air or on solid targets. The prototype achieves audio reproduction only within a part of the audible range due to limitations in the available laser specifications, however, without hindering the demonstration of the system's functionality at a proof-of-concept level.

1.2.2.1 Transducer prototype

Novel laser-sound transducer architecture

The general structure of a novel laser-sound transducer driven via ΣΔ pulse streams is developed and the requirements of the constituent stages are analyzed, while a real implementation of a laser-sound prototype is presented.

Laser triggering and pulse modulation

A novel method for triggering the emission of laser pulses through an audio interface is experimentally demonstrated. This simple triggering method allows for efficient direct transcoding of digital audio information into trains of laser generated N-pulses. Moreover, amplitude modulation of the emitted pulses is demonstrated through the well-established electro-optic modulation technique, based on the Kerr effect.

Acoustic performance evaluation

A method for the evaluation of the optoacoustic transducer in terms of acoustic performance, predictability and energy efficiency is presented. Results from systematic acoustic measurements of reproduced test audio signals, particularly sine waves, sine sweeps, speech and music signals are shown, while recorded audio samples from the experiments are available as complementary material for auditory evaluation. The main acoustical parameters of the system, namely, its impulse and frequency response, are calculated in the band of interest both experimentally and analytically from sine sweep inputs. This work also provides an analysis of the energy loss processes involved in the laser plasma optoacoustic transduction and preliminary estimations of the energy efficiency are carried out for both the implemented prototype and the high specifications simulated system. Finally, it discusses the advantages of a laser-sound reproduction system over the current transducer technology, while it outlines potential hazards and solutions for its adoption in commercial or end-user applications.

1.2.2.2 Signal processing techniques

Laser-sound transduction model

A specially developed mathematical model is presented and used for the simulation of the system's performance within and beyond the audible frequency range, showing good agreement with the experimental evaluations. The model constitutes a complete tool for the simulation and design of laser-sound systems, as it enables the evaluation of the acoustic response of any ΣΔ-based laser-sound system in the time and frequency domain with high precision.

Ideal laser-sound transducer simulation

This Thesis also investigates the performance and acoustical parameters of an ideal laser-sound system with a rapid impulse response and perfectly equalized frequency response in a band of interest extending through the entire audible range. Estimations of the laser and control requirements for the implementation of such a system are also provided.

1.2.3 Analysis of the DFT spectra of UPWM signals

A novel method for the analysis and derivation of the out-band Discrete Fourier Transform (DFT) coefficients of Uniform-sampling Pulse Width Modulation (UPWM) signals originating from random Pulse Code Modulation (PCM) signals is presented. It is shown that, if the input PCM signal can be modeled as a random signal with its samples being independent and identically distributed (iid) random variables (RV) generated by an ergodic random process, the DFT coefficients of the resulting UPWM signal in the out-band range can be calculated from the statistical moments of the underlying random process.

It is also demonstrated that closed-form expressions of the DFT coefficients of UPWM signals can be derived, when the samples of the random input signal are iid RVs following known distributions, such as Gaussian, Laplacian, Arcsine and Uniform. Finally, it is shown that, when statistical independence between the samples of the input signal does not hold, only the DFT components on the harmonic frequencies of the PWM carrier can be calculated from the input signal's statistics.

From the analysis it becomes evident that, the out-band DFT coefficients of the output of a UPWM modulator with such random inputs can be accurately predicted without knowledge of the particular time-series of the input signal.

1.3 Publications and awards

A list of the publications related to this Thesis can be found below. Particularly, six (6) papers were submitted to international peer-reviewed journals, two (2) additional journal papers were under preparation at the time of writing and four (4) peer-reviewed conference papers were presented and published in the proceedings. Finally, one (1) patent application was filed to the German patent office.

1.3.1 Journal papers

[1] Kaleris, K., Orfanos, Y., Bakarezos, M., Papadogiannis, N. & Mourjopoulos, J. Experimental and analytical evaluation of the acoustic radiation of femtosecond laser plasma filament sound sources in air. The Journal of the Acoustical Society of America 146, EL212-EL218 (2019).

[2] Kaleris, K., Orphanos, Y., Bakarezos, M., Dimitriou, V., M., Tatrakis, M., Mourjopoulos, J. & Papadogiannis, N. On the correlation of light and sound radiation following laser-induced breakdown in air, Journal of Physics D: Applied Physics (2020).

[3] Kaleris, K., Stelzner, B., Hatziantoniou, P., Trimis, D. & Mourjopoulos, J. Laser-sound: optoacoustic transduction from digital audio streams. Nature Scientific Reports 11, 476 (2021).

[4] Kaleris, K., Stelzner, B., Hatziantoniou, P., Trimis, D. & Mourjopoulos, J. Laser-sound: audio reproduction from digital ΣΔ streams, Journal of the Audio Engineering Society, in press (2021).

[5] Kaleris, K., Tazes, I., Orphanos, Y., Petrakis, S., Bakarezos, M., Mourjopoulos, J., Dimitriou, V. Tatarakis, M. & Papadogiannis, N. A. Experimentally validated modeling of the optical energy deposition in highly ionized ambient air by strong femtosecond laser pulses, European Journal of Physics D, in press (2021)

[6] Kaleris, K., Delibašić, H. Petrović & Papadogiannis, N., Analytical and numerical analysis of the plasma evolution in air generated by nanosecond laser pulses, ***under review*** (2021)

1.3.2 Conference papers

[7] Kaleris, K. & Mourjopoulos, J. Dual-band PWM audio coding for ultrasound artefact reduction, proceedings of the 25th European Signal Processing Conference (EUSIPCO), Kos, 2017, pp. 1829-1863 (2017).

[8] Kaleris, K., Papadakos, C. & Mourjopoulos, J. Dual-Band PWM for Filterless Class-D Audio Amplification, proceedings of the 144 AES Convention, Milan, pp. 9937 (2018).

[9] K Kaleris, J. Mourjopoulos, J. Orfanos, E. Bakarezos, N. Papadogiannis, Sound reproduction from laser-driven sound sources (Laser Audio), proceedings of the Hellenic Institute of Acoustics “ACOUSTICS2018” conference (in Greek), Patras, Greece, October (2018).

[10] Kaleris, K., Orphanos, Y. Bakarezos, M. Papadogiannis, N. & Mourjopoulos, J. The effect of plasma geometry on the acoustic radiation of laser filaments, proceedings of Forum Acusticum, Lyon (2020).

1.3.3 Patent

[11] Kaleris, K., Stelzner, B., Trimis, D. and Mourjopoulos, J., Vorrichtung und Verfahren zur Wiedergabe mindestens eines akustischen Signals (DE Patent subm. No 10 2021 200 293.5), Deutsches Patent- und Markenamt (DPMA), submitted Jan 2021.

1.3.4 Award

The paper “The effect of plasma geometry on the acoustic radiation of laser filaments” [10] presented in the Forum Acusticum international conference (December 2020) was awarded with the European Acoustics Association (EAA) best student paper and presentation Award, sponsored by the Head Genuit Foundation.

1.4 Thesis Structure

This Thesis is structured as follows. In Chapter 2, the physics principles and applications of laser-induced breakdown of gases and laser ablation of solids are presented. The general concepts of linear and non-linear laser pulse propagation, optical energy deposition, plasma generation and sound and light emission following laser-induced breakdown are discussed and a simple mathematical description of these aspects is outlined. Moreover, the utilization of laser-generated acoustic pulses in current technological and scientific applications is briefly presented.

Chapter 3 discusses the principles and applications of current sound and ultrasound reproduction technology, with emphasis on the pulsed audio modulations. Three such modulations, Sigma Delta Modulation (ΣΔ), Pulse Width Modulation (PWM) and Pulse Amplitude Modulation (PAM) are analyzed and their mathematical descriptions are presented. Moreover, Chapter 3 presents the novel method for the calculation and analysis of the DFT spectrum of UPWM signals derived from random input signals.

In Chapter 4, the work on the correlation between light and sound radiation following laser-induced breakdown in air is presented, with emphasis on the combined experimental, analytical and signal processing methodology followed.

In Chapter 5, the experimental and analytical work on the description of the acoustic radiation of laser filaments is presented, using concepts of Chapter 4. The filament's parameters affecting its acoustic radiation are determined and its directivity and frequency spectra are derived.

In Chapter 6, the theoretical and technical aspects of the novel laser-sound optoacoustic transducer are presented. The developed laser-sound prototype is presented and the methodology and results from its overall evaluation are discussed.

Finally, Chapter 7 includes a summary of the novel findings and potential impact of this work, along with a thorough description of the open topics and future tasks.

References

[1] Beranek, L. L. & Mellow, T. J. Acoustics: Sound Fields, Transducers and Vibration (Academic Press, London, 2019).

[2] Sanders, R. R. The Electrostatic Loudspeaker Design Cookbook (Audio Amateur Pr, Peterborough, NH, 2004)

[3] The Piezo-Electric Loud-Speaker. Nature 133, 184 (1934)

[4] Tian, Y. et al. Coherent generation of photo-thermo-acoustic wave from graphene sheets. Nat. Sci. Rep. 5, 10582 (2015).

[5] Kontomichos, F., Koutsioubas, A., Mourjopoulos, J., Spiliopoulos, N. & Vradis, A. A thermoacoustic device for sound reproduction. J. Acoust. Soc. Am. 123(5), 3707 (2008)

[6] Béquin, P., Castor, K., Herzog, P. & Montembault, V. Modeling plasma loudspeakers. J. Acoust. Soc. Am. 121(4), 1960–1970 (2007)

[7] *Audio recording - Compact disc digital audio system*, *IEC 60908:1999,* International Electrotechnical Commission, Switzerland (1999)

[8] Oraevsky, A.A., Jacques, S.L., Esenaliev, R.O. & Tittel, F.K. Laser-based optoacoustic imaging in biological tissues, Proc. SPIE, 2134A:122-128 (1994)

[9] Arnott, P. W., Moosmüller, H., Abbott, R. E. & Ossofsky, M. D. Thermoacoustic enhancement of photoacoustic spectroscopy: Theory and measurements of the signal to noise ratio, Review of Scientific Instruments 66, 4827-4833 (1995)

[10] Shah, S. K. H. et al. Laser induced breakdown spectroscopy methods and applications: a comprehensive review. Radiat. Phys. Chem. 170, 108666 (2020).

[11] Sonoda, Y. et al. Proposal of Optical Wave Microphone and Physical Mechanism of Sound Detection, 135th AES Convention (2013).

[12] Ghosh, S. & Mahesh, K. Numerical simulation of laser-induced breakdown in air, 46th AIAA Aerospace Sciences Meeting and Exhibit (2008)

[13] Qin, Q. & Attenborough, K. Characteristics and application of laser-generated acoustic shock waves in air. Appl. Acoust. 65(4), 325–340 (2004)

[14] Gómez Bolaños, J., Delikaris-Manias, S., Pulkki, V., Eskelinen, J. & Hæggström, E. Laser-induced acoustic point source for accurate impulse response measurements within the audible bandwidth. J. Acoust. Soc. Am. 135, EL298–EL303 (2014)

[15] Eskelinen, J., Hæggström, E., Delikaris-Manias, S., Bolaños, J. & Pulkki, V. Beamforming with a volumetric array of massless laser spark sources—application in reflection tracking. J. Acoust. Soc. Am. 137, 389–395 (2015).

[16] Kaleris, K., Orphanos, Y., Bakarezos, M., Dimitriou, V., M., Tatrakis, M., Mourjopoulos, J. & Papadogiannis, N. On the correlation of light and sound radiation following laser-induced breakdown in air. J. Phys. D: Appl. Phys. 53, 435207 (2020).

[17] Kaleris, K., Orfanos, Y., Bakarezos, M., Papadogiannis, N. & Mourjopoulos, J. Experimental and analytical evaluation of the acoustic radiation of femtosecond laser plasma filament sound sources in air. J. Acoust. Soc. Am. 146, EL212–EL218 (2019).

[18] Song, Z. & Sarwate, D. V., The Frequency Spectrum of Pulse Width Modulated Signals, Signal Processing, 83(10), 2227–2258 (2003)

[19] Sun, J. Pulse-Width Modulation, in *Dynamics and Control of Switched Electronic Systems*, Springer, pp. 25-61 (2012)

[20] Pavan, S., Schreier, R., & Temes, G. C. Understanding delta-sigma data converters. Hoboken, NJ: Wiley (2017)

[21] Janssen, E., & van Roermund, A. H. M. Basics of Sigma-Delta Modulation, in *Look-Ahead Based Sigma-Delta Modulation*. essay, Springer Netherlands (2011)

[22] Rumsey, F. Class D Power Amplification, Journal of the Audio Engineering Society, 57(12), 1087-1093 (2009)

[23] Self, D. (2009). *Audio power amplifier design handbook (5th edition)*, Elsevier Ltd, Amsterdam (2009)

[24] Norsworthy, S. R. *Delta-Sigma Data Converters: Theory, design and simulation*. IEEE Press (1997).

[25] Farina, A. Advancements in Impulse Response Measurements by Sine Sweeps, AES Convention 122, p. 7121 (2007)

[26] Melchior, V. High-resolution audio: a history and perspective. J. Audio Eng. Soc. 67(5), 246–257 (2019)

[27] Nuijten, P., Reefman, D. Why Direct Stream Digital (DSD) is the best choice as a digital audio format, AES Convention 110, 5396 (2001)

[28] Oksanen, M. & Hietanen, J., Photoacoustic breakdown sound source in air, Ultrasonics 32, 327–331 (1994)

[29] Couairon, A., & Mysyrowicz, A. Femtosecond filamentation in transparent media. Physics Reports, 441(2-4), 47–189 (2007)

[30] L. E. Kinsler, *Fundamentals of Acoustics*, John Wiley & Sons, New York (2000)

Chapter 2

Physics and applications of laser-driven sound generation: an engineering approach

Contents

Introduction

The breakdown of ambient air or other gases from short or ultrashort laser pulses (Laser Induced Breakdown – LIB) has been known since the early 60's [1][2][3], shortly after the invention of the laser in 1960 [4]. Through the years, the evolution of the laser technology has led to the development of laser systems capable of emitting high-energy short and ultrashort pulses at a broad range of wavelengths. Nowadays, nanosecond, picosecond and femtosecond laser systems capable of inducing breakdown in ambient air or other gases are rather compact and affordable and are widely available for use both in scientific laboratories and in the industry. The accessibility to such lasers and the suitability of laser-driven plasma generation for various technological and scientific applications has led to an increasing interest for the study and modeling of the phenomenon.

From an engineering perspective, laser-plasma sound generation can be treated as an optical-to-acoustic energy conversion process that takes as input a laser pulse and gives at the output an acoustic pulse, with the characteristics of the acoustic pulse depending on the laser radiation parameters and the attributes of the targeted medium, as shown in Fig. 2.1. Nevertheless, design and optimization of laser generated sound applications, such as the laser-sound transducer presented in this thesis [5][6], requires good understanding of the numerous physical processes involved in the phenomenon. In this section, the fundamental physical concepts behind laser-induced breakdown are discussed and basic mathematical formulations of the various aspects of the phenomenon are presented, particularly the laser pulse propagation in the air, the deposition of optical energy in the medium, the generation of free electrons and the formation of a plasma volume, the impact of plasma generation on the propagation of the laser pulse and finally the secondary radiative phenomena following breakdown, namely, the formation of a shock wave and the emission of light. Fundamental aspects of laser ablation of solid targets are only briefly discussed, since laser ablation was only used in this work for practical reasons (see Chapter 6). Finally, a comprehensive summary of establish or proposed scientific and industrial applications of laser-plasma sound generation is provided.

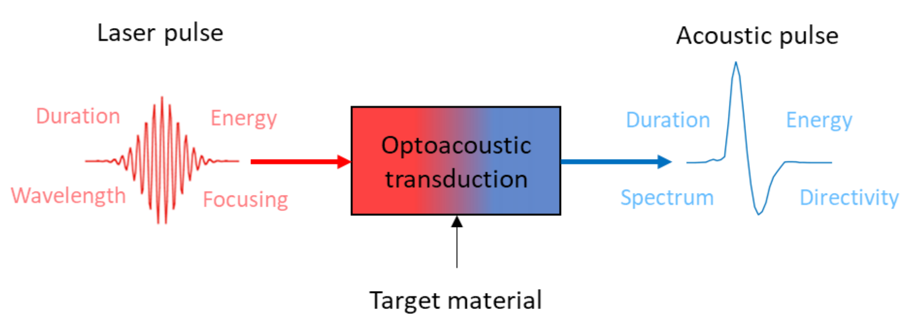

Fig. 2.1: An engineering perspective to laser plasma optoacoustic transduction: dependence of the acoustic pulse parameters on the parameters of the laser pulse and the target material.

2.1 Laser-induced breakdown of gases

Laser-induced breakdown in ambient air or other gases from short or ultrashort laser pulses is a highly complex phenomenon that involves a multitude of linear and non-linear physical processes, starting with the propagation and focusing of the laser pulse that leads to deposition of optical energy in a confined area of the targeted medium, where the conditions for the generation of free electrons are met. In this region, the optical intensity surpasses a minimum threshold beyond which, the medium becomes opaque for the particular laser wavelength. Apart from the parameters of the medium, such as consistency, humidity, pressure and temperature [7][8], this threshold depends on the duration and wavelength of the laser pulse [9][10][11][12]. With the exception of filamentation (see subsection 2.1.3), the time scales at which energy deposition takes place are comparable to the duration of the laser pulse, and in fact are a portion of it, since only part of the pulse energy is absorbed [10][13]. After the plasma formation, the free electrons interact with each other and with the heavy particles, namely, the ions, atoms and molecules, in the ionized region. From the interactions, the heavy particles gain energy, which statistically leads to a local thermalization of the medium [14]. The increased heat in the confined volume causes a rapid supersonic expansion that generates high pressure at the boundary with the surrounding air, essentially forming a shock wave initially coupled to the excited volume. The expansion leads to a progressive de-excitation of the volume and at the moment when the internal pressure is equilibrated by the pressure of the surrounding air, the shock wave decouples from the source and propagates through the medium, progressively transforming into a sound wave [15]. Finally, throughout the relaxation process, optical radiation is emitted from the excited volume, initially due to Bremsstrahlung of the free electrons and consequently due to radiative recombinations of free electrons, de-excitations of bound electrons to less excited states and blackbody-type continuous thermal radiation due to high temperature of the excited volume [14][13].

2.1.1 Pulse propagation and energy deposition

Energy deposition from short or ultrashort laser pulses in ambient air has been thoroughly investigated both experimentally and analytically. Experimentally, the amount of the deposited energy can be calculated relatively easily, by measuring the optical energy before and after the breakdown spot, as shown in Fig. 2.2. For the analytical study of energy deposition in laser breakdown of gases, complete models based on the non-linear Schrödinger equation including a wide range of linear and non-linear propagation phenomena have been presented, as for example in the works of [16][17][18][19][20][21]. Here, a simplified model is presented that provides good insight in the fundamental aspects of laser-induced breakdown. The model is based on the work of Bulgakova, Bulgakov et al. [22][23][24] and describes the optical energy deposition in ambient air through the transport equation with a sink. Thereby, the spatio-temporal evolution of the laser light flux ε is described as a result of Gaussian focusing and optical energy losses through the equation:

$$\frac{\partial(s\varepsilon)}{\partial t}+\frac{\partial(sc\varepsilon)}{\partial z}=-Q \tag{1}$$

where $c=c_0/n$ is the speed of light with n the refractive index, s is the Gaussian focusing term given by $s(z)=1+z^2/z_R^2$, with z_R the Rayleigh length expressed as $z_R=\pi\, w_0^2 n/\lambda$, where λ is the laser wavelength and w_0 is the beam waist at the focal spot, given by $w_0=2\lambda f_L/\pi D$. Finally, Q is the sink term representing the rate of energy losses per unit volume. In this model, the pulse is introduced through the flux ε at the initial point of observation z_0 and is expressed as:

$$\varepsilon=\frac{F_0\exp\left(-\frac{r^2}{w_0^2}-\frac{t^2}{t_L^2}\right)}{\sqrt{\pi}\, ct_L s(z_0)} \tag{2}$$

where F_0 is the peak laser fluence at the focal spot, which is expressed in terms of the laser pulse energy E_0 as:

$$F_0=2E_0/\pi w_0^2 \tag{3}$$

The sink term depends on the ionization mechanisms, namely, Multi-Photon Ionization (MPI), Tunneling Ionization (TI) and Over-the-Barrier Ionization (OBI), as well as on the density of the generated plasma. The dominating ionization regime is identified by the value of the Keldysh parameter γ [25][28], defined as:

$$\gamma=\frac{\omega\sqrt{2mI_p}}{eF} \tag{4}$$

where m, e are the electron mass and charge, respectively, I_p is the ionization potential of the gas atoms or molecules (N, N_2 and O, O_2 for ambient air [29]) and ω, F are the radial frequency and laser field strength of the optical pulse, respectively. For a value $\gamma \gg 1$, MPI dominates and the energy losses due to photoionization can be expressed as [24]:

$$Q_{\mathrm{MPI}}=-sW_{\mathrm{MPI}}(\rho_0-\rho_e)k\hbar\omega \tag{5}$$

where $\hbar\omega$ is the energy of a single photon, $k=\mathrm{ceil}(I_p/\hbar\omega)$ is the number of photons needed to ionize an atom or molecule (order of ionization), W_{MPI} is the ionization rate and ρ_0 and ρ_e are the particle density of neutral air and the free electron density, respectively.

In the tunneling regime ($\gamma \ll 1$), the strong field approximation applies, where the influence of the laser is treated as a potential that is superimposed on the Coulomb potential of the atom or molecule. In this regime, under conditions also in the MPI regime, plasma absorption becomes significant due to the increased free electron density. Plasma absorption is the result of inverse Bremsstrahlung, namely, the absorption of photons by free electrons during their collision with heavy particles. The sink term Q_{abs} can be evaluated via the Drude model [18]:

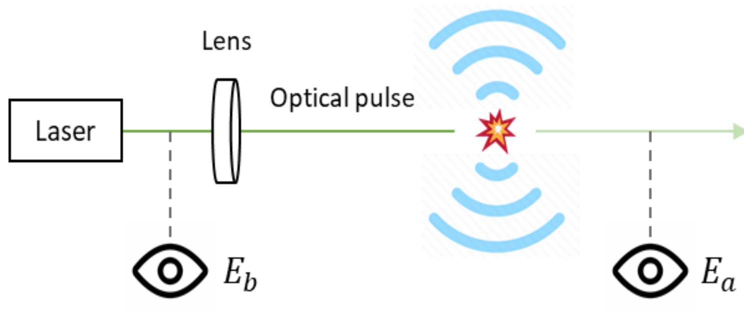

Fig. 2.2: Energy absorption in air breakdown by tightly focused femtosecond laser pulses, where E_b, E_a is the optical energy before and after breakdown, respectively.

$$Q_{\text{abs}} = \sigma_{\text{iB}} \rho_e I \tag{6}$$

where σ_{iB} is the inverse Bremsstrahlung cross-section, given by:

$$\sigma_{\text{iB}} = \frac{e^2}{\varepsilon_0 m_e c n} \cdot \frac{\tau_c}{1 + \omega^2 \tau_c^2} \tag{7}$$

ε_0 is the vacuum permittivity and τ_c is the electron collision time, which is $\sim$350 fs for the ambient air [18]. Both Q_{MPI} and Q_{abs} depend on the free electron density ρ_e, which can be calculated from the respective electron rate equation that corresponds to the particular ionization regime and the duration of the optical pulse. The rate equations of different ionization regimes are presented in the following subsection.

2.1.2 Plasma generation

In multiphoton ionization, the atom or molecule simultaneously absorbs more than one photon and loses an electron. It can be roughly considered that this mechanism dominates for intensities $I \ll 5 \times 10^{13}\ \text{W/cm}^2$ [28] which is the typical regime for air breakdown from tightly focused few-nanosecond pulses with energies of up to a few tens of millijoules. For such longer pulses, apart from photoionization, electron Cascade Ionization (CI) also is also apparent, in which, bound electrons are released due to impact with free electrons that have been accelerated under the influence of the electric field of the laser pulse. The CI process results in a rapid geometric increase of the free-electron density, significantly affecting the generated free electron density and the plasma and gas temperature, and thus also the shock wave characteristics [10][11]. Moreover, the duration of such pulses is comparable to the timescales of the relaxation processes, particularly, electron recombination, attachment and diffusion out of the interaction volume [10]. In order to accurately calculate the spatio-temporal profile of the free electron density, all these processes need to be taken into consideration in a rate equation, which can be formulated as:

$$\frac{d\rho_e}{dt} = W_{\text{MPI}}(\rho_0 - \rho_e) + W_{\text{CI}}\rho_e - D\rho_e - \eta\rho_e - R{\rho_e}^2 \tag{8}$$

where W_{CI}, D, η are the rates of cascade ionization, diffusion and attachment, while the term $R{\rho_e}^2$ accounts for the electron recombinations [10][11]. Such a rate equation has an analytical solution [11] and can be used in conjunction with Eq. (1) to estimate the spatiotemporal profile of the deposited energy from nanosecond laser pulses in the MPI regime. Analytical expressions for the equation coefficients can be found in [10].

However, for ultrashort pulses i.e. few picosecond or femtosecond duration, in the MPI regime, Eq. (8) reduces to [17][18][24]:

$$\frac{d\rho_e}{dt} = W_{\mathrm{MPI}}(\rho_0 - \rho_e) = \sigma_{\mathrm{MPI}} I^k (\rho_0 - \rho_e) \tag{9}$$

where σ_{MPI} is the MPI cross-section. CI does not take place at time ranges in the order of the laser pulse duration since the pulses are too short to accelerate the free electrons and cause a cascade phenomenon, while the electron loss processes take place at much larger time scales than the duration of the laser pulse. Of course, in order to study the breakdown throughout its complete extent, the electron loss mechanisms have to be included in the rate equation. However, such models require multiscale solutions, since the phenomena evolve at time scales extending over several orders of magnitude, i.e. from a few femtoseconds to several tens of nanoseconds.

Furthermore, for higher intensities, tunneling or over-the-barrier ionization takes place, where it can be considered that the Coulomb potential of the atom or molecule is bent under the influence of the electric field of the laser pulse, allowing the electrons to either quantum-mechanically tunnel through (TI) or simply classically diffuse (OBI) to the continuum. In this case, the photoionization rate W_{MPI} needs to be replaced with the TI rate W_{TI}, for which, several theories have been developed with main the representatives being Keldysh [25], Ammosov-Delone-Krainov (ADK) [26] and Perelemov-Popov-Terent'ev [27]. It should be noted that, since the optical intensity varies along the axis of the laser pulse, different parts of the pulse can reside in different ionization regimes. For example, the intensity of the leading and trailing edges of the pulse can lie in the MPI regime, while the intensity of the main part of the pulse lies in the TI regime. Although MPI often leads to negligible electron yields compared to TI, for ionization conditions where $\gamma \sim 1$, MPI and TI can be comparable. Analytical formulas of the ionization rate in this intermediate regime have been developed [28][30], while PPT theory also accounts for this regime as it applies to any value of γ [27]. Furthermore, a combined rate can also be considered, by selecting W_{MPI} or W_{TI} depending on the instantaneous pulse intensity:

$$W_{\mathrm{PI}} = \begin{cases} W_{\mathrm{MPI}}, & I < I_{\mathrm{thres}} \\ W_{\mathrm{TI}}, & I \geq I_{\mathrm{thres}} \end{cases} \tag{10}$$

which, however, can be inaccurate in the intermediate regime ($\gamma \sim 1$) and can lead to incorrect estimations of the free electron rate in cases where this regime has a significant role in the phenomenon.

Finally, two additional aspects need to be considered for the formulation of the appropriate rate equations. Primarily, the presented approaches apply to single ionization and do not account for multiple (double, triple, quadruple etc.) ionization of the same atom or molecule [29]. In the work of Fill et al. [12] it can be found that the intensity threshold I_q for q^{th} over the barrier ionization can be approximately estimated via:

$$I_q = 4 \cdot 10^9 \cdot \frac{1}{q^2} \cdot I_p^4 \tag{11}$$

from which the thresholds for double and triple ionization of Nitrogen and Oxygen can be easily calculated, see Table I. Such intensities are commonly reached by tightly focused few-millijoules femtosecond pules, and hence, multiple ionization has to be included in the modeling of the free electron generation rate under the influence of such pulses. However, this task requires both additional rate equations and the respective ionization rates for q^{th} ionization. An approach to the modelling of multiple ionizations can be found in the work of [31].

The second aspect is the involvement of chirp in case of non-Fourier limited laser pulses [32][33][34]. For a chirped laser pulse, the instantaneous frequency is a function of time (or space, depending on the description), so that:

$$\omega(t) = \omega_0 + \frac{2C}{\pi\, t_L^2} \cdot (t - t_0) \tag{12}$$

where ω_0 is the central frequency of the pulse, $t_L = \frac{\tau}{2\, ln(2)}$ and τ is the pulse duration at full width half maximum (FWHM), C is the chirp parameter and t_0 is the time instance corresponding to the center of the pulse.

In order to account for frequency-dependent differences of the electron yield, the ionization rate coefficients need to be frequency dependent as well. There are several such expressions for the MPI rate, for example in the works of Keldysh, Hamam [25][10], while ionization cross-sections for different number of absorbed photons can also be found, for example in [18] and used in the well-known formula $\sigma_{\text{MPI}}(k)I^k$, in which case, the frequency dependence is included in the number of photons $k(\omega)$ required for ionization. Respectively for the TI rates, the commonly used ADK formula cannot be used, as it does not account for spatio-temporal variations in the laser pulse frequency, and thus, more complex formulas, such as PPT, are required [32][35].

Table I

I (W/cm^2)	N	O
$q = 2$	7.67×10^{14}	1.52×10^{15}
$q = 3$	2.24×10^{15}	4.05×10^{15}

2.1.3 Non-linear refractive index and filamentation

2.1.3.1 Plasma defocusing

Equation (1) accounts for the Gaussian focusing induced by a focal lens but does not account for other focusing and defocusing mechanisms caused by the non-linear modulation of the refractive index due to the generated plasma or the electric field of the pulse [17][36]. Particularly, plasma generation has an impact on the real part of the refractive index of the medium as it effectively changes its consistency, i.e. from a mixture of neutral N_2 and O_2 molecules to a mixture with additional N and O atoms, N^+ and O^+ ions and free electrons.

$$n_1 = \sqrt{1 - \frac{\rho_e}{\rho_{\mathrm{cr}}}} \tag{13}$$

where ρ_{cr} is the critical plasma density. The critical density is defined as the minimum plasma density for which an electromagnetic wave of a specific wavelength can no longer propagate into the plasma, and is given by:

$$\rho_{\mathrm{cr}} = \frac{\varepsilon_0 m_e \omega^2}{e^2} \tag{14}$$

From Eq. (13) it can be easily seen that the refractive index of the plasma always has a lower value than that of the ambient air. Moreover, for a laser pulse with a typical Gaussian distribution along the radial dimension:

$$I(r) \sim \exp\left(-\frac{r^2}{w_0^2}\right) \tag{15}$$

the generated plasma density also varies in the radial dimension, and particularly, it exhibits its peak density in the core while it gradually decreases towards the wings. Hence, according to Eq. (13), also the refractive index of the ionized medium is modulated in the radial dimension, with the core having a lower refractive index than the wings, effectively acting as a negative lens. This induces a defocusing effect on the optical pulse, which is usually non-negligible and leads both to a shift of the focal spot towards the opposite direction of the pulse propagation and to a larger beam waist at the focal spot. As a result, the focused pulse never reaches the theoretical peak intensity taken by considering the theoretical beam waist in vacuum [24]:

$$I_{\mathrm{peak}} = \frac{2E_0}{\pi w_0^2 \tau} \tag{16}$$

The impact of plasma defocusing in the optical energy deposition during laser-induced breakdown can be accounted for in the presented model be substituting the refractive index of the air with the one calculated via Eq. (13).

2.1.3.2 Self-focusing

Strong electric fields can induce changes in the polarization of a medium [37][36], a non-linear phenomenon that can also manifest under the influence of the electric field of a strong laser pulse itself. This can be expressed as a change Δn of the refractive index that is proportional to the intensity of the laser pulse, so that:

$$\Delta n = n_2 I \tag{17}$$

where n_2 is the second-order non-linear refractive index of the medium. When significant i.e. for laser intensities higher than 10^{13} W/cm^2, this phenomenon, known as the optical Kerr effect, leads to self-focusing of the pulse, effectively inducing energy transfer from the pulse wings towards the pulse core. The increase in the refractive index acts in the exact opposite way of the decrease induced by plasma defocusing. Due to the Kerr effect, the refractive index is modulated in the radial dimension, taking higher values in the core of the pulse and decreasing towards the pulse wings, leading the medium to act as a positive lens. It should be noted that the optical Kerr effect also leads to self-phase modulation and modulational instability [37][18][39], which, however, are beyond the scope of this Thesis and will not be further discussed.

2.1.3.3 Filamentation

It was shown that plasma defocusing and self-focusing have opposing effects on the propagation of a laser pulse, acting as a negative and a positive lens, respectively. Under certain conditions, the two phenomena can coexist during laser-induced breakdown of gases and can lead to the generation of elongated plasma threads known as laser-plasma filaments [17][18][20][36][38][39]. The mechanism behind filamentation can be understood by examining the total refractive index of a gaseous medium under the influence of a strong ionizing pulse:

$$n = n_1 + n_2 I \tag{18}$$

The term n_1 has a rather complex inverse relation to the laser pulse intensity, since a higher intensity generally leads to a denser plasma and thus, to a lower real part of the refractive index; on the contrary, the second-order term $n_2 I$ increases proportionally to the intensity. For a high intensity pulse in the absence of dense plasma, self-focusing dominates leading to an increase of the intensity, which consequently leads to the generation of a denser plasma. This effectively leads to a decrease in the refractive n due to the decrease in n_1, and to defocusing of the pulse, which results to a lower optical intensity and, consequently, to a less dense plasma. The recurrent focusing and defocusing leads to a recurrent tightening and broadening of the plasma channel along the pulse propagation axis, as depicted in Fig. 2.3. Moreover, it results to the conservation of the breakdown process along the pulse propagation axis, as it prohibits both a beam collapse towards the core and the optical defocusing after the focal spot. Filamentation terminates when the laser pulse energy is depleted due to absorption and is insufficient to induce self-focusing.

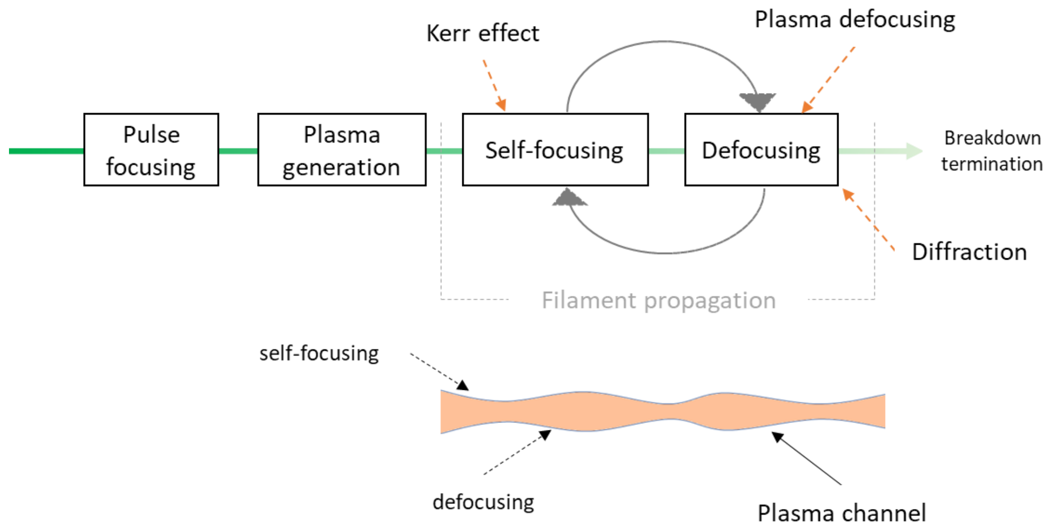

Fig. 2.3: Schematic diagram of the alternating non-linear processes leading to elongated plasma channels (filaments) during air breakdown from femtosecond laser pulses.

2.1.4 Shock-wave generation

The generation of a shock wave following laser-induced breakdown has been extensively studied in the past. In general, the modeling of shock waves stems from the studies of blast waves carried out in Los Alamos by Bethe [41], von Neumann et al. [40][41], while significant contribution was done by Zel'dovich and Raizer [14]. Pioneering experimental studies of the laser-generated shock waves were carried out by Bell and Landt [42] Tittmann et al. [43], Edwards et al. [44], while the work of Oksanen and Hietanen established the commonly accepted formulation of the laser-generated shock waves as N-pulses [45]. Ghosh and Mahesh have developed rigorous fluid dynamics models of shock wave propagation following laser-induced breakdown, based on the Navier-Stokes equations [46][47]. Temperature-based numerical models have been proposed for the simulation of the complete phenomena taking place in laser-induced breakdown, which, however, are extremely complex to develop and solve [19][20][21]. Moreover, the correlation between the generated acoustic wave and the light radiation following laser-induced breakdown has been investigated. Point et al. [36] have reported that the initial pressure distribution along the filament axis is related to the light intensity radiated from the filament, while Kaleris et al. [48][49] have adopted this relation to develop an acoustic model of the sound emission of plasma filaments. Moreover, Biagioni et al. [50] have reported a correlation between the generated plasma density and the resulting acoustic pressure, while Kaleris et al. [13] have developed a phenomenological model to derive the frequency spectrum of the laser-generated acoustic wave from the light emitted by the interaction volume.

It is known that sound generation following laser-induced breakdown of gases is the result of the thermoelastic expansion and consequent collapse of the ionized volume, which is thermalized by energy transfer from the free electrons to the heavy particles. Ionized air can be effectively seen as a mixture of an electron gas and an ion/atom/molecule gas, with the two gases initially being out of equilibrium since, while free electrons generated by strong tightly focused pulses can reach temperatures of several hundred thousand ℃ , the temperature of the heavy particles is not significantly affected by the ionization process [14][51]. The establishment of thermodynamic equilibrium between the two gases is achieved by progressive energy transfer from the electrons mainly to the ions, as the cross-section of the free electron interactions with neutral particles is generally small, with the main energy transfer mechanism being deflection [14]. Due to the huge mass difference between electrons and the heavy ions, energy transfer to the ions per collision is very low and hence, a very large number of electron-ion collisions is required for an appreciable energy transfer to take place. This can be easily seen by considering the collision between an initially still ion with mass m_i, and an electron with speed v_e. The speed v_i of the ion after the deflection cannot exceed the value:

$$v_i = \frac{2m_e}{m_i + m_e} v_e \tag{19}$$

which is extremely small considering that m_e/m_i is in the order of $\sim 10^{-4}$. The characteristic energy transfer time in air breakdown from typical tightly focused few tens of millijoules nanosecond pulses is of the order of 10^{-8} [14].

With the temperature increase, the interaction volume starts to expand due to the internal pressure difference with the ambient air. The expansion takes place at supersonic velocities, with typical initial values being in the order of 3000 m/s for strongly focused nanosecond pulses with pulse energy of several tens of millijoules [45]. The expansion leads to progressive de-excitation of the thermalized volume and, as soon as the internal pressure is equilibrated by the ambient pressure, the shock wave decouples from the interaction volume and propagates through the air.

The main attribute of shock waves is the pressure discontinuities at the edges of the wave which correspond to the shock front at the circumference of the interaction volume and the elastic reaction of the medium to the void formed by the radial acceleration of the thermalized particles. The discontinuities render the description of the propagation medium as a fluid inappropriate and are treated via the introduction of discontinuity surfaces between the shock wave and the fluid (ambient air) [14]. Nevertheless, the shock wave progressively loses energy by heating the air and ultimately transforms into a linearly propagating acoustic wave, as shown in Fig. 2.4. Laser-generated acoustic waves are generally modeled as ideal N-pulses and by adopting the approach presented in [45][48][5], the N-pulse signal $s'_{\mathrm{p}}(n)$ can be expressed as:

$$s'_{\mathrm{p}}(n) = \frac{A}{N_{\mathrm{p}}} \cdot n \cdot \left(u(n + N_{\mathrm{p}}) - u(n - N_{\mathrm{p}})\right) \tag{20}$$

where $u(n)$ is the unit step function, N_p is the number of half the samples of the pulse and A is the pulse amplitude.

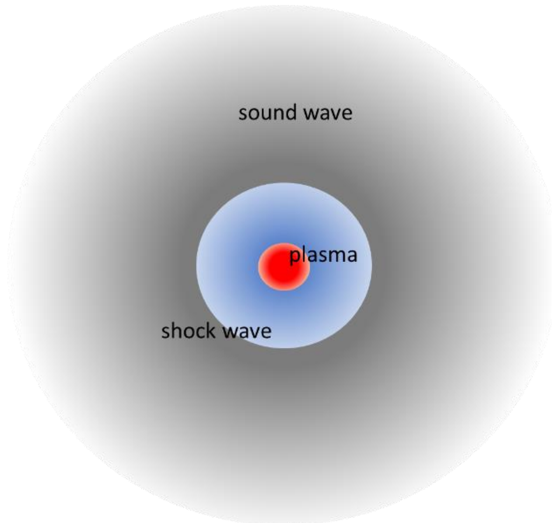

Fig. 2.4: Generation of a pressure wave following laser breakdown in the air, initially propagating at supersonic velocity as a shock wave and progressively transforming into a linear sound wave.

The frequency spectrum ${S_\mathrm{p}}'(k)$ of $s'_\mathrm{p}(n)$ obtained via DFT can be written as:

$$S'_\mathrm{p}(k) = \frac{A}{N_\mathrm{p}} \cdot \sum_{n=-N_\mathrm{p}}^{N_\mathrm{p}} n \cdot e^{-j\frac{2\pi}{N}kn} \tag{21}$$

Due to the very short duration of the N-pulse, which is typically in the order of a few up to a few tens of microseconds, N_p takes very small values compared to N, so that the spectral magnitude $|S'_\mathrm{N}(k)|$ of the laser-generated N-pulse becomes:

$$\left|S'_\mathrm{p}(k)\right| = A \cdot \left|\sin\left(\frac{2\pi N_\mathrm{p}}{N}k\right)\right| \tag{22}$$

Again, for the frequencies in the band of interest (in-band), $k \ll N$ and $\frac{N_\mathrm{p}}{N}k \ll 1$, Eq. (22) becomes:

$$\left|S'_\mathrm{p}(k)\right| \simeq \frac{2\pi A N_\mathrm{p}}{N}k \tag{23}$$

Equation (23) shows that for the in-band frequencies, the laser-generated acoustic pulses exhibit a first-order high-pass spectral profile, which holds for the vast parameter range of the generating laser pulses [45][48][5][52]. However, the frequency of the spectral peak varies with the width of the N-pulse, which depends on the characteristics of the laser radiation, such as pulse duration, wavelength and energy, as well as focusing conditions, which essentially define the spatio-temporal profile of the deposited energy. The temporal and spectral profiles described in Eq. (20) and (23), respectively, are depicted in the time and frequency domain representations of a measured N-pulse generated by a 6 ns, 40 mJ optical pulse focused with $f/8$, shown in Fig. 2.5. A more thorough analysis of the dependence of the generated acoustic wave on the laser parameters is presented in Chapter 4.

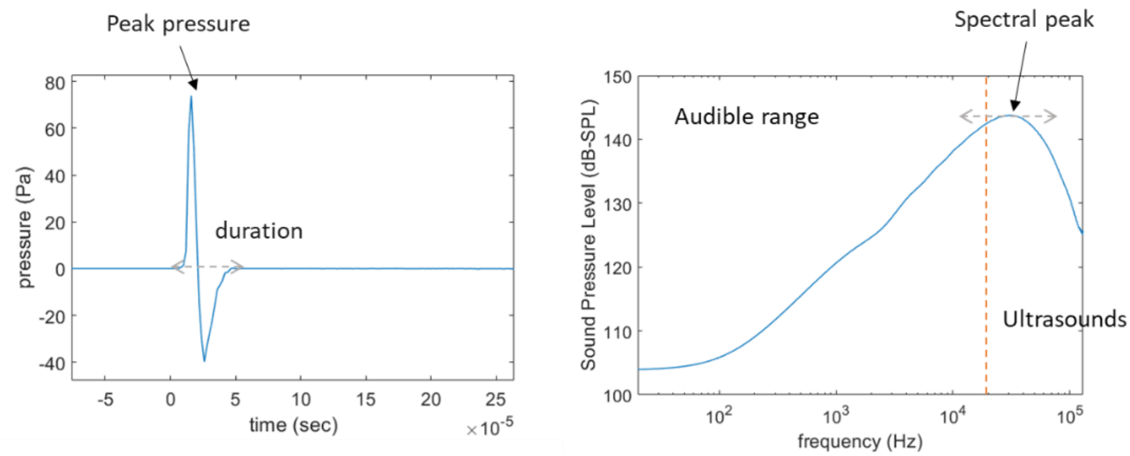

Fig. 2.5: a) Time profile and b) frequency spectrum of an acoustic N-pulse generated by a 40 mJ, 6 ns laser pulse with $f/8$ focusing.

2.1.5 Light emission

Apart from the emission of a sound wave, laser-induced breakdown is accompanied by the emission of light that originates from luminescent and thermal processes. A thorough analysis of LIB light radiation was done by Zel'dovicz et al. [14], while time-resolved and spectrally-resolved optical measurements of the emitted light following breakdown of the ambient air are presented in [13] and [53], respectively. For breakdown from nanosecond laser pulses, three distinct radiative phases can be generally defined:

a. The early phase, where light is emitted mainly due to electron Bremsstrahlung, namely, radiative deflections of free electrons from ions. These free-free radiative electron transitions have a duration comparable to the duration of the nanosecond laser pulse and produce a rapid and intense light signal.
b. The intermediate phase, where free-bound and bound-bound electron transitions due to recombination and de-excitation coexist, while at the same time, thermal radiation develops with the progressive thermalization of the medium.
c. The late phase, where the plasma has relaxed and only thermal radiation is apparent, until the complete cooldown of the excited volume.

It should be noted that, for low-temperature plasmas, such as the ones formed in laser filamentation, light radiation due to Bremsstrahlung and heat are negligible [36], and the emitted light originates exclusively from electron recombinations and de-excitations. Chapter 4 presents systematic time-resolved measurements and signal analysis of the light radiation following LIB from tightly focused nanosecond pulses, along with a more thorough analysis of the discussed radiative mechanisms.

2.2 Laser ablation of solid targets

Laser ablation of solid materials is the process of removing material from the solid surface by irradiation from a laser beam. At low laser intensities, the material is heated by the absorbed laser energy and evaporates or sublimates. At high laser intensities, the material is typically directly converted to a plasma. Laser ablation through plasma generation is the result of ionization of a solid target due to strong laser radiation that leads to material etching on the surface of the target. Laser ablation from sufficiently strong short or ultrashort laser pulses is followed by the emission of a shock wave, and hence, it is of interest for acoustics or ultrasounds applications. However, the sound generation mechanism essentially differs from that in laser breakdown of gases. In laser ablation, acoustic pressure is generated mainly due to the transfer of kinetic energy from the fragments of the ionized material to the particles of the surrounding air via collisions [54]. The fragments escaping the surface of the material form a hemispherical vapor plume, effectively pushing the surround air particles and generating a hemispherical shock wave [56] that progressively transforms into a sound wave as it propagates away from the ablated material [54][55]. Nevertheless, the temporal and spectral characteristics of the acoustic pulses generated by laser ablation are equivalent to those generated by laser breakdown of gases, as the ones presented in section 2.1.4 and shown in Fig. 2.5. The particular duration of the generated acoustic wave and its frequency spectrum depend on the parameters of the laser radiation and the characteristics of the material.

Laser ablation can be induced by laser fluences significantly lower than the ones needed for laser-induced breakdown, and particularly, in the order of $10^8 - 10^{10}\ \mathrm{W/cm^2}$, while it can also lead to high light-to-sound conversion efficiencies, potentially exceeding 30% [45][58]. This is partially due to the generally stronger optical absorption efficiency from the solid target, but also due to the strong coupling between the colliding heavy particles of the ablated material and the ambient air [57]. Interestingly, there are significant differences in the mechanisms leading to sound generation from laser ablation depending on the duration of the laser pulse, which also lead to differences in the generated sound [59][60]. Particularly, in nanosecond laser ablation, the pulse tail interacts with the fragments of the material produced by the pulse front, further heating the plasma and leading to a stronger ultrasound. This phenomenon does not take place for femtosecond pulses, as the plasma plume does not form in such short time scales and hence, there is no interaction of the plasma with the laser pulse [60]. On the other hand, shorter pulses lead to less thermal dissipation in the target since thermal dissipation evolves at longer time scales. Thus, shorter pulses lead to more efficient ablation at a given fluence, and hence to a more efficient light-to-sound conversion [59][60].

Laser ablation is utilized in this work to limit the required optical intensity for plasma optoacoustic transduction, in order to achieve multilevel audio transcoding in the laser-sound prototype. Due to the exclusively practical adoption of ablation, further details on the phenomenon will not discussed here.

2.3 Applications of laser-driven sound generation

Over the last decades, laser-driven sound and ultrasound generation have been proposed for and adopted in a variety of scientific fields and applications. One of the first and most widely spread applications of laser generated N-pulses is the triggering of ink ejection in laser jet printers [61]. Moreover, laser generated sound has been used early on for remote sensing, material diagnostics and spectroscopy in scientific and industrial applications. Laser-generated shock waves in liquids have been used for the study of cavitation bubbles [62], while ablation-generated ultrasonic waves on solids have been used for material diagnostics [63][64][65][57]. Laser ultrasound generation in the air close to a solid surface has been used as a non-destructive alternative to ablation for diagnostics but also for the measurement of the thickness of thin films [57]. An extensive review of laser plasma ultrasound generation in material diagnostics and characterisation can be found in the work of Davies et al. [57]. Furthermore, laser-generated sound has been used for remote sensing, often as a complementary method to Laser Induced Breakdown Spectroscopy (LIBS), as it provides direct information on the targeted material, such as hardness and consistency, only by auditory evaluation of the generated acoustic signal [67][68]. Interestingly, acoustic LIBS received broad attention with the incorporation of the SuperCam/Mars Microphone [69][70][71] system in NASA's Mars 2020 mission.

The broad and repeatable frequency spectrum of laser-generated N-pulses along with the very high sound pressures achieved, renders laser-generated sound suitable for acoustics applications. Cooper et al. have proposed the use of LIB N-pulses for the calibration of other ultrasonic transducers, while Hietanen [72] et al. have proposed their use for the characterisation of capacitive ultrasonic transducers . More recently, Bolaños, Eskelinen, Delikaris-Manias, Pulkki et.al. have demonstrated the suitability of LIB for acoustic measurements [73][74][75][76]. Particularly, the suitability of laser-generated N-pulses in ambient air for the evaluation of room acoustic responses has been shown in [73], while the possibility to synthesize any acoustic directivity from a point cloud of laser-generated plasma sources in a 3D layout in air (volumetric array) has been demonstrated in [75]. Moreover, such massless directional acoustic sources have been proposed for synthesizing and evaluating radiation patterns in reverberant environments [76], for example reproduced by loudspeakers, while such an application has been experimentally evaluated via a scale model in [74].

Finally laser-generated sound waves have also been investigated for military / defense applications [77][78][79], such as the development of non-lethal weapons and the laboratory study of sonic booms, while they also play a central role in Inertial Nuclear Fusion (INF) as they can be used to ignite the nuclear reaction [80][81].

Conclusions

In this Chapter, the basic physical aspects of laser plasma generation in air or on solid targets were presented. For this purpose, a simple mathematical model describing laser pulse propagation and optical energy absorption was outlined, along with the rate equations describing the generation of free electron. For the pulse propagation, linear Gaussian focusing by a lens was considered, while the influence of the non-linear phenomena of plasma defocusing and self-focusing due to the optical Kerr effect were also described through the mathematical expressions of the non-linear refractive index. The different mechanisms involved in gas breakdown under the influence of short (nanosecond) and ultrashort (femtosecond) laser pulses were discussed and their influence on the electron rate equations was formulated. The different ionization regimes, particularly multiphoton, tunneling and over the barrier ionization were described and the main theories deriving the respective photoionization rates were discussed.

Moreover, in this Chapter the mechanisms behind the secondary radiative phenomena following laser-induced breakdown of gases, namely the emission of a sound and a light pulse, were described. The thermoelastic nature of sound generation in laser breakdown was highlighted and the processes involved in the transfer of energy from the free electrons to the heavy particles in the ionized volume were outlined. Light emission was attributed to free-free, free-bound and bound-bound processes, corresponding to radiative electron deflection from heavy particles (Bremsstrahlung), electron recombinations and de-excitations as well as to thermal radiation. The time scales at which the different processes take place were also discussed, while the differences in light emission from hot and cold plasmas were also briefly mentioned.

Laser ablation on solid targets was briefly discussed in a qualitative manner, since it is not thoroughly studied in in this thesis but only utilized as a practical means for mitigating the energy required to transduce optical energy into sound in the laser-sound prototype presented in Chapter 6. Finally, the main scientific and engineering applications of sound generation via laser breakdown of gases / liquids and laser ablation of solid targets were presented, focusing on applications related to acoustics.

References

[1] Meyerand, R. G. Jr., Haught, A. F., Gas Breakdown at Optical Frequencies, Phys. Rev. Lett. 11, 401 (1963)

[2] Nelson, P., Veyrie, P., Berry, M. & Durand, Y. Experimental and theoretical studies of air breakdown by intense pulse of light. Physics Letters 13, 226-228 (1964)

[3] Korobkin, V. & Alcock, A. Self-Focusing Effects Associated with Laser-Induced Air Breakdown. Physical Review Letters 21, 1669-1669 (1968)

[4] Maiman, T. Stimulated Optical Radiation in Ruby. Nature 187, 493–494 (1960)

[5] Kaleris, K., Stelzner, B., Hatziantoniou, P., Trimis, D. & Mourjopoulos, J. Laser-sound: optoacoustic transduction from digital audio streams. Nature Scientific Reports 11, 476 (2021).

[6] Kaleris, K., Stelzner, B., Hatziantoniou, P., Trimis, D. & Mourjopoulos, J. Laser-sound: audio reproduction from digital ΣΔ streams, under review.

[7] Chylek P., Jarzembski M.A., Srivastava V. & Pinnick R.G. Pressure dependence of the laser-induced breakdown thresholds of gases and droplets, Applied Optics (1990)

[8] Bettis, J. R. Correlation Between the Laser-Induced Breakdown Threshold in Solids, Liquids, and Gases Laser-Induced Damage in Optical Materials (1990)

[9] Gao, Z., Han, L., & Li, J. Investigation of laser induced air breakdown thresholds at 1064, 532, 355, 266 and 248nm. Pacific Rim Laser Damage 2019: Optical Materials for High-Power Lasers (2019)

[10] Hamam, K., Gaabour, L. & Gamal, Y. Numerical modeling for investigating the optical breakdown threshold of laser-induced air plasmas at different laser characteristics, Physics of Plasmas 24, 073515 (2017)

[11] Kaleris, K., Delibašić H., Petrović, V. & Papadogiannis, N. A. Analytical and numerical analysis of the plasma evolution in air generated by nanosecond laser pulses, under review.

[12] Fill, E. E. Focusing limits of ultrashort laser pulses: analytical theory, Journal of the Optical Society of America B, 11(11), 2241 (1994)

[13] Kaleris, K., Orphanos, Y., Bakarezos, M., Dimitriou, V., M., Tatrakis, M., Mourjopoulos, J. & Papadogiannis, N. On the correlation of light and sound radiation following laser-induced breakdown in air, Journal of Physics D: Applied Physics (2020)

[14] Zel'dovič, J. & Rajzer, J. *Physics of shock waves and high-temperature hydrodynamic phenomena*. Acad. Pr. (1970)

[15] Sobral, H., Villagran-Muniz, M., Navarro-Gonzalez, R. & Raga, A. C. Temporal evolution of the shock wave and hot core air in laser induced plasma, Applied Physics Letters 77, 3158–3160 (2000)

[16] La Fontaine, B., Vidal, F., Jiang, Z., Chien, C. Y., Comtois, D., Desparois, A., Johnston, T. W., Kieffer, J.-C., Pépin, H., & Mercure, H. P. Filamentation of ultrashort pulse laser beams resulting from their propagation over long distances in air, Physics of Plasmas, 6(5), 1615–1621 (1999)

[17] Couairon, A., Tzortzakis, S., Bergé, L., Franco, M., Prade, B., & Mysyrowicz, A. Infrared femtosecond light filaments in air: simulations and experiments. Journal of the Optical Society of America B, 19(5), 1117 (2002)

[18] Couairon, A., & Mysyrowicz, A. Femtosecond filamentation in transparent media. Physics Reports, 441(2-4), 47–189 (2007)

[19] Shneider, M. N., Zheltikov, A. M., & Miles, R. B. Tailoring the air plasma with a double laser pulse. Physics of Plasmas, 18(6), 063509 (2011)

[20] Papeer, J. et al. Multi variable control of filamentation of femtosecond laser pulses propagating in air. J. Phys. B At. Mol. Opt. Phys. 48, 094005 (2015)

[21] Henis, Z., Milikh, G., Papadopoulos, K. & Zigler, A. Generation of controlled radiation sources in the atmosphere using a dual femtosecond/nanosecond laser pulse. J. Appl. Phys. 103, 103111 (2008)

[22] Bulgakova, N. M., Bulgakov, A. V., Zhukov, V. P., Marine, W., Vorobyev, A. Y., & Guo, C. Charging and plasma effects under ultrashort pulsed laser ablation. High-Power Laser Ablation VII (2008)

[23] Bulgakova, N., Panchenko, A., Zhukov, V., Kudryashov, S., Pereira, A., Marine, W., Mocek, T., & Bulgakov, A. Impacts of Ambient and Ablation Plasmas on Short- and Ultrashort-Pulse Laser Processing of Surfaces. Micromachines, 5(4), 1344–1372 (2014).

[24] Bulgakov, A. V., Mirza, I., Bulgakova, N. M., Zhukov, V. P., Machulka, R., Haderka, O., Campbell, E. E., & Mocek, T. Initiation of air ionization by ultrashort laser pulses: evidence for a role of metastable-state air molecules. Journal of Physics D: Applied Physics, 51(25) (2018)

[25] Keldysh, L. V. IONIZATION IN THE FIELD OF A STRONG ELECTROMAGNETIC WAVE, Soviet Physics JETP, 20(5) (1965)

[26] Ammosov, M. V., Delone, N. B., & Krainov, V. P. TUNNEL IONIZATION OF COMPLEX ATOMS AND ATOMIC IONS IN ELECTROMAGNETIC FIELD, Soviet Physics JETP (1986)

[27] Perelomov, A. M., Popov, V. S. & Terent'ev, M. V., IONIZATION OF ATOMS IN AN ALTERNATING ELECTRIC FIELD, Soviet Physics JETP (1966)

[28] Wang, R. et al. Identification of tunneling and multiphoton ionization in intermediate Keldysh parameter regime, Optics Express, 27(5), 6471 (2019)

[29] Guo, C., Li, M., Nibarger, J. P. & Gibson, G. N. Single and double ionization of diatomic molecules in strong laser fields, Physical Review A, 58(6) (1998)

[30] Tamulienė, V., Juškevičiūtė, G., Buožius, D., Vaičaitis, V., Babushkin, I. & Morgner, U. Influence of tunnel ionization to third-harmonic generation of infrared femtosecond laser pulses in air, Scientific Reports, 10(1) (2020)

[31] Liu, X.-L., Lu, X., Liu, X., Xi, T.-T., Liu, F., Ma, J.-L., & Zhang, J. Tightly focused femtosecond laser pulse in air: from filamentation to breakdown, Optics Express, 18(25), 26007 (2010)

[32] Nuter, R., & Bergé, L. Pulse chirping and ionization of O2 molecules for the filamentation of femtosecond laser pulses in air, Journal of the Optical Society of America B, 23(5), 874 (2006)

[33] Ghaforyan, H., Sadighi-Bonabi, R., & Irani, E. The Effect of Chirped Intense Femtosecond Laser Pulses on the Argon Cluster, Advances in High Energy Physics, 2016, 1–9 (2016)

[34] Tzianaki, E. Controlling nanoscale acoustic strains in silicon using chirped femtosecond laser pulses, Applied Physics Letters, 108(25), 254102 (2016)

[35] Lai, Y. H., Xu, J., Szafruga, U. B., Talbert, B. K., Gong, X., Zhang, K., Fuest, H., Kling, M. F., Blaga, C. I., Agostini, P., & DiMauro, L. F. Experimental investigation of strong-field-ionization theories for laser fields from visible to midinfrared frequencies. Physical Review A, 96(6) (2017)

[36] G. Point, Energy deposition in air from femtosecond laser filamentation for the control of high voltage spark discharges, Ph.D. thesis, Ecole Polytechnique, Laboratoire d'Optique Appliquée (2015).

[37] R. W. Boyd, Nonlinear Optics, 3rd ed. (Academic Press, Inc., Orlando, FL, 2008)

[38] Rosenthal, E. W. Energy deposition in femtosecond filamentation: measurements and applications, Ph.D thesis, University of Maryland, Department of Physics (2017)

[39] Couairon, A., Mysyrowicz, A. Femtosecond Filamentation in Air. *in: Progress in Ultrafast Intense Laser Science Volume I. Springer Series in Chemical Physics*, 84, Springer, Berlin, Heidelberg (2006)

[40] Bethe, H. A., Fuchs, K., Hirschfelder, J. O., Magee, J. L., Rudolph, E. Peierls & von Neuman, J. *Blast Wave*, laboratory report, University of California, Los Alamos, New Mexico (1947)

[41] Bethe, H.A. On the Theory of Shock Waves for an Arbitrary Equation of State. *In: Johnson J.N., Chéret R. (eds) Classic Papers in Shock Compression Science. High-Pressure Shock Compression of Condensed Matter*. Springer, New York, NY (1998)

[42] Bell, C.E. and Landh, J.A. Laser induced high-pressure shock waves in water, Appl Phys Lett, (10)2, (1967)

[43] Tittmann, B.R., Graham, L.J. and Linebarger, R. Laser-induced acoustic shock waves, Proceedings of the IEEE Ultrasonics Symposium (1987)

[44] Edwards, C., Taylor, G.S. and Palmer, S.B. Ultrasonic generation with a pulsed TEA CO 2 laser J Phys D (1989)

[45] Oksanen, M. & Hietanen, J. Photoacoustic breakdown sound source in air. Ultrasonics 32, 327-331 (1994)

[46] Ghosh, S. and Mahesh, K. Direct Numerical Simulation of the Thermal Effects in Plasma/Turbulence Interaction 45th AIAA Aerospace Sciences Meeting and Exhibit (2007)

[47] Ghosh, S. and Mahesh, K. Numerical simulation of laser-induced breakdown in air, 46th AIAA Aerospace Sciences Meeting and Exhibit (2008)

[48] Kaleris, K., Orfanos, Y., Bakarezos, M., Papadogiannis, N. & Mourjopoulos, J. Experimental and analytical evaluation of the acoustic radiation of femtosecond laser plasma filament sound sources in air. The Journal of the Acoustical Society of America 146, EL212-EL218 (2019)

[49] Kaleris, K., Orphanos, Y. Bakarezos, M. Papadogiannis, N., & Mourjopoulos, J. The effect of plasma geometry on the acoustic radiation of laser filaments, proceedings of Forum Acusticum, Lyon (2020)

[50] Biagioni, A. et al. Electron density measurement in gas discharge plasmas by optical and acoustic methods. Journal of Instrumentation, 11(08) (2016)

[51] Aguilera, J. A., & Aragón, C. Characterization of laser-induced plasma during its expansion in air by optical emission spectroscopy: Observation of strong explosion self-similar behavior. Spectrochimica Acta Part B: Atomic Spectroscopy, 97, 86–93 (2014)

[52] Gómez Bolaños, J., Delikaris-Manias, S., Pulkki, V., Eskelinen, J. & Hæggström, E. Laser-induced acoustic point source for accurate impulse response measurements within the audible bandwidth. J. Acoust. Soc. Am. 135, EL298–EL303 (2014)

[53] Harilal, S., Brumfield, B. & Phillips, M. Lifecycle of laser-produced air sparks. Physics of Plasmas 22, 063301 (2015)

[54] Chen, J. P., Ni, X. W., Lu, J., & Bian, B. M. Initial formation process of laser-induced plasma shock wave in air. Optics Communications, 176(4-6), 437–440 (2000)

[55] Hosoya, N., Kajiwara, I., Inoue, T., & Umenai, K. Non-contact acoustic tests based on nanosecond laser ablation: Generation of a pulse sound source with a small amplitude. Journal of Sound and Vibration, 333(18), 4254–4264 (2014).

[56] Vogel, A. & Venugopalan, V. Mechanisms of Pulsed Laser Ablation of Biological Tissues. Chemical Reviews, 103, 577-644 (2003).

[57] Davies, S. J., Edwards, C., Taylor, G. S., & Palmer, S. B. Laser-generated ultrasound: its properties, mechanisms and multifarious applications. Journal of Physics D: Applied Physics, 26(3), 329–348 (1993)

[58] Hutchins, D. A. Mechanisms of pulsed photoacoustic generation. Canadian Journal of Physics, 64(9), 1247–1264 (1986).

[59] Laville, S. et al. Fluid modeling of the laser ablation depth as a function of the pulse duration for conductors, Phys. Rev. E, 66, 066415 (2002)

[60] Hébert, H. et al. Ultrasound generated by a femtosecond and a picosecond laser pulse near the ablation threshold. Journal of Applied Physics, 98(3), 033104 (2005)

[61] Tam, A.C. and Gill, W.D. Photoacoustic ejection from a nozzle (PEN) for drop-on-demand ink jet printing, Applied Optics (1982)

[62] Lanterborn, W. High speed photography of laser induced breakdown in liquids, Appl Phys Lett, 21, 27-29 (1972)

[63] Bondarenko, A.N. Drobat, Yu. B., Kruglov, S.V. Optical excitation and detection of nanosecond acoustic pulses in nondestructive testing Sov J NDT, 12, 655-658 (1976)

[64] Chen, G., & Yeung, E. S. Acoustic signal as an internal standard for quantitation in laser-generated plumes. Analytical Chemistry, 60(20), 2258–2263 (1988)

[65] Orphanos, Y., Kosma, K., Kaselouris, E. et al. Integrated nanosecond laser full-field imaging for femtosecond laser-generated surface acoustic waves in metal film-glass substrate multilayer materials. Appl. Phys. A 125, 269 (2019)

[66] Dewhurst, R. J., Hutchins, D. A., Palmer, S. B., & Scruby, C. B. Quantitative measurements of laser-generated acoustic waveforms. Journal of Applied Physics, 53(6), 4064–4071 (1982)

[67] Hrdlička, A. et al. Correlation of acoustic and optical emission signals produced at 1064 and 532 nm laser-induced breakdown spectroscopy (LIBS) of glazed wall tiles. Spectrochimica Acta Part B: Atomic Spectroscopy, 64(1), 74–78 (2009)

[68] Huang, F. et al. Normalization of underwater laser-induced breakdown spectroscopy using acoustic signals measured by a hydrophone. Applied Optics, 60(6):1595-1602 (2021)

[69] Murdoch, N., Chide, B., Lasue, J., Cadu, A., Sournac, A. et al. Laser-induced breakdown spectroscopy acoustic testing of the Mars 2020 microphone. Planetary and Space Science, Elsevier, 165, 260-271 (2019)

[70] Chide, B. et al. The Mars 2020 SuperCam Microphone to constrain rock hardness and LIBS crater volume, 50th Lunar and Planetary Science Conference (2019)

[71] Chide, B. et al. Focusing a Laser Induced Breakdown Spectroscopy (LIBS) telescope with a Microphone, 50th Lunar and Planetary Science Conference (2019)

[72] Hietanen, J., & Oksanen, M. Photoacoustic testing of ultrasonic air transducers. Measurement Science and Technology, 5(8), 960–963 (1994)

[73] Gómez Bolaños, J., Delikaris-Manias, S., Pulkki, V., Eskelinen, J. & Hæggström, E. Laser-induced acoustic point source for accurate impulse response measurements within the audible bandwidth. J. Acoust. Soc. Am. 135, EL298–EL303 (2014).

[74] Gómez-Bolaños, J. et al. Benefits and applications of laser-induced sparks in real scale model measurements. J. Acoust. Soc. Am. 138, EL175–EL180 (2015).

[75] Eskelinen, J., Hæggström, E., Delikaris-Manias, S., Bolaños, J. & Pulkki, V. Beamforming with a volumetric array of massless laser spark sources—application in reflection tracking. J. Acoust. Soc. Am. 137, 389–395 (2015).

[76] Delikaris-Manias, S., Bolaños, J. G., Eskelinen, J., Huhtakallio, I., Hæggström, E., Pulkki, V., Auralization of source radiation pattern synthesized with laser spark room responses. Journal of the Audio Engineering Society, 64(10), 720-730 (2016).

[77] Jones, T., Hornstein, M., Ting, A. & Wilkes, Z. Intense underwater laser acoustic source for Navy applications. J. Acoust. Soc. Am. 125, 2556–2556 (2009).

[78] Hornstein, M., Jones, T., Ting, A. & Nicholas, M. Directivity and frequency control of an intense underwater laser acoustic source for navy applications. J. Acoust. Soc. Am. 127, 1985–1985 (2010).

[79] Radziejewska, J., Strzelec, M., Ostrowski, R., & Sarzyński, A. Experimental investigation of shock wave pressure induced by a ns laser pulse under varying confined regimes. Optics and Lasers in Engineering, 126, 105913 (2020)

[80] Eliezer, S., & Martinez Val, J. M. The comeback of shock waves in inertial fusion energy. Laser and Particle Beams, 29(2), 175–181 (2011)

[81] Kaselouris, E. et al. The importance of the laser pulse-ablator interaction dynamics prior to the ablation plasma phase in inertial confinement fusion studies. Philosophical Transactions of the Royal Society A: Mathematical, Physical and Engineering Sciences, 378(2184), 20200030 (2020)

Chapter 3

Sound reproduction and pulsed audio modulations

Contents

Introduction

As discussed in the previous Chapter, laser-induced breakdown from pulsed lasers leads to the generation of discrete acoustic pulses with an N-shaped time profile. Due to the pulsed nature of laser-plasma sound sources, the development of the proposed laser-based sound reproduction system dictates for pulsed audio signal encoding. Pulsed audio modulations are widely used in state-of-the-art sound reproduction technology, typically for: digital-to-analog (D/A) or analog-to-digital (A/D) conversion stages [1][2][3][4][5][6] and audio signal amplification, mainly in class-D audio amplifiers [7][8][9][10] while they have also been adopted in digital loudspeakers [11], MEMS-based drivers [12] and more recent systems that allow direct reconstruction of digital audio bitstreams in air, without the need for D/A conversion. A/D and D/A converters usually rely on Sigma-Delta (ΣΔ) audio modulation [1][13][14] and constitute the basic building blocks of any digital audio system. Class-D amplifiers, sometimes also referred to as digital amplifiers, are currently used in a broad spectrum of audio applications, from high-end audio systems to energy-sensitive systems such as mobile phones and hearing aids. Such amplifiers are driven from pulsed signals mainly obtained via ΣΔ and Pulse Width Modulation (PWM) [15][16][17], where ΣΔ is implemented either in a 1-bit or a multi-bit (usually up to 5-bits) scheme, while PWM can be either digital or analog.

This thesis builds upon such well-established concepts of pulsed modulations for sound reproduction to develop a novel laser-based audio reproduction technology that transcodes digital audio signals into laser-generated acoustic pulse streams. In effect, the proposed system converts digital audio low-level signal streams into a power level acoustic waveform. For this reason, in this Chapter the fundamentals of state-of-the-art sound reproduction chains are presented and compared to a conceptual representation of the laser-sound reproduction chain. Also, the main pulsed audio modulations of interest for the laser-sound technology, namely ΣΔ, PWM and additionally, analog Pulse Amplitude Modulation (PAM) [18], are presented, along with their mathematical descriptions. The main time-domain characteristics of the respective modulated signals are presented and their in-band and out-of-band frequency spectra are analyzed and compared.

Finally, a novel method for the derivation of the out-band Discrete Fourier Transform (DFT) coefficients of Uniform-sampling PWM signals originating from random input signals with independent and identically distributed samples is presented. Closed-form expressions of the UPWM DFT coefficients are derived for input signals following Gaussian, Laplacian, arcsine and uniform distributions. The findings are supported by computational evaluations of the DFT of UPWM signals via Fast Fourier Transform (FFT), showing good agreement.

3.1 Sound reproduction chains

Traditionally, sound reproduction chains consist of an audio source, often a pre-amplifier, a power amplifier and usually an electromechanical moving-coil transducer, while an additional digital-to-analog (D/A) conversion stage is added before the pre-amplifier in case of digital audio input signals [19][20]. The block diagram of such a sound reproduction chain is presented in Fig. 3.1 a). However, the development and widespread deployment of class-D amplifies, due to their simpler circuitry and high energy efficiency, has brought changes to the traditional chain. A class-D amplifier receives at the input a stream of rectangular pulses that is derived from the original input signal with the use of a modulation unit. After amplification, the pulse stream is passed through an output filter (LPF) that removes the high frequency components of the modulated signal, effectively reconstructing an amplified version of the original signal and delivers it to the loudspeakers [8].

The sound transduction chain based on a class-D amplifier is shown in Fig. 3.1 b). Note that, depending on the implementation, digital-to-analog conversion might be combined with the pre-amplification of the signals. If pre-amplification is not required, the analog or digital input can be directly routed to the modulator, as common modulators can synchronize with digital streams. Moreover, Class-D amplifiers can be efficiently driven by either pulse density signals, such as ΣΔ signals, or pulse width signals. Roughly speaking, they identify two input signal states, a high (1) state, which they amplify, and a low (0) state, which they leave unchanged, effectively acting as switches providing output pulse streams that are identical to the input streams, only with amplified pulses. Multi-bit ΣΔ implementations can also be employed, usually for D/A conversion [10], but they require more complex circuitry and often lead to less cost-efficient designs.

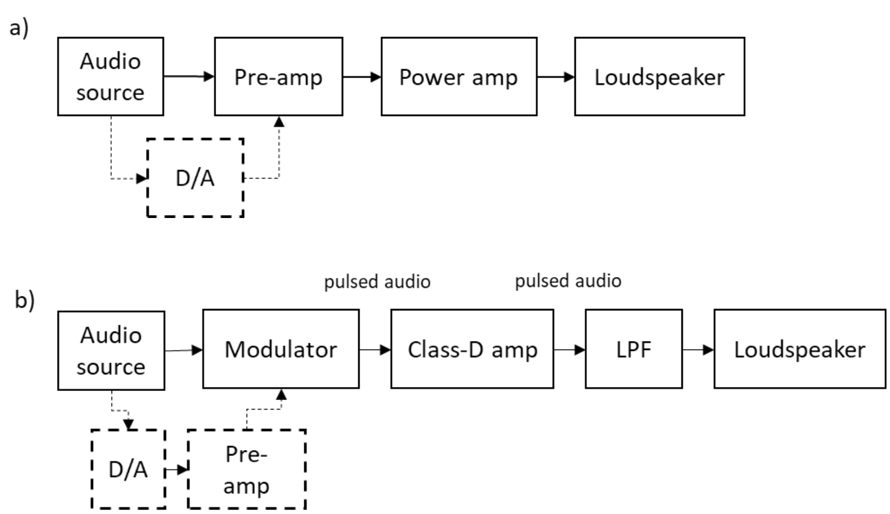

Fig. 3.1: Block diagram of typical audio reproduction chain based on a) a traditional analog amplifier and b) a class-D amplifier.

The laser-sound system developed here and presented in Chapter 6 follows a rather similar concept to class-D amplifiers, disregarding the D/A and pre-amplification stages. Indicative sound transduction chains based on 1-bit and multibit ΣΔ laser-sound transducers are shown in Fig. 3.2 a) and b) respectively [21][22]. The 1-bit, or equivalently 2-level, ΣΔ implementation is particularly simple to realize via a laser-sound system by encoding the 0 as a no-pulse and the 1 as a pulse and for this reason, but also due to the efficiency of its implementation in terms of laser pulse energy, it is used for the proof-of-concept demonstration of the transducer prototype, as shown in Chapter 6. However, the adoption of multi-bit ΣΔ, PWM or analog Pulse Amplitude Modulation (PAM) can potentially have advantages over the 1-bit ΣΔ implementation, leading to significantly reduced laser requirements in exchange for increased system complexity, non-linearities and added laser radiation control hardware [21][22]. This aspect is further discussed in Chapter 6, where experimental results are shown from a 1.5-bit (3-level) implementation of the laser-sound prototype, while simulations of a 5-bit system are also analyzed.

As extensively presented in Chapter 6, the interface is necessary in a 3-level implementation for delivering the trigger sequence to the external trigger input of the laser and the control signal to the Electro-Optical Modulation (EOM) [23]. Note that the EOM stage is only required for multi-level implementations. In 1-bit ΣΔ implementations or other possible implementations discussed in Chapter 7, the laser or the EOM can be directly driven by the modulator. Nevertheless, it can be argued that in the laser-sound system the class-D amplifier, low-pass filter and electro-mechanical speaker are replaced by a laser unit with potential optical pulse amplitude control. It becomes evident that the laser-sound transducer performs both the required power amplification of the signal and the electroacoustic energy transduction, via an intermediate conversion to optical energy. Details on the design, implementation and evaluation of the laser-sound transducer are presented in Chapter 6.

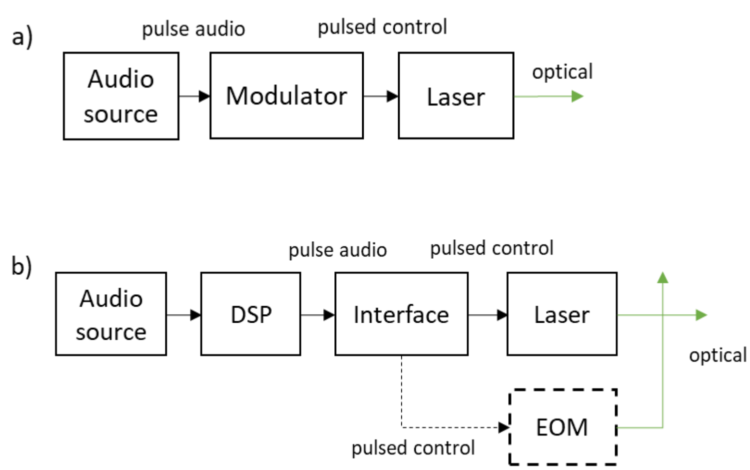

Fig. 3.2: Block diagram of typical laser-sound reproduction chain based on a) 1-bit and b) multibit ΣΔ audio modulation.

3.2 Pulsed audio modulations

Before looking into each modulation separately, it is convenient to describe a common aspect of pulsed modulations, particularly the formation of out-of-band (OoB) spectral components in the modulated signal. Starting from a band-limited modulating (or input) signal with a highest frequency component f_{in}, the frequency spectrum of the modulated signal, whether ΣΔ, PWM or PAM, extends well beyond f_{in} [14][16][18]. The frequency range $f > f_{\text{in}}$ is called out-of-band or out-band spectrum and originates from the pulsed nature of the modulation. In general terms it can be thought of as the result of the discrete and abrupt nature of the acoustic pulses, which translates in the frequency domain as high-frequency content beyond the range of the original information signal. Note that, while the characteristics of the out-of-band spectrum differ between the modulations, the spectral content in the in-band range (IB), also called the band of interest, remains unchanged – or mostly unchanged – in all modulations. This effectively means that, in all these non-linear modulations, the original signal can be reconstructed from the modulated signal via simple low-pass filtering. As shown later, this characteristic of the discussed pulsed modulations renders them appropriate for sound reproduction via laser-generated acoustic pulse streams without the need for a receiving or demodulation device, since reconstruction of the original sound signal is directly done in the human auditory system.

For the existing D/A and class D amplifier systems, the out-of-band modulation artifacts are suppressed by analogue Low Pass Filters. However, in the proposed system, such a filtering operation is not viable since the final reconstruction takes place in the air or on solid medium. Hence, an extensive and novel analysis of out-of-band artifacts – especially for PWM, is also presented in this Chapter with the view of potential signal preconditioning to control these unwanted components.

3.2.1 Sigma-Delta (ΣΔ) modulation

As mentioned in the introduction, ΣΔ modulation is widely used in analog-to-digital and digital-to-analog conversion [1][2][3][4][5][6], transmission and storage of audio data [24][25] as well as amplification and reproduction of audio signals [7][8][9][10]. It is also used for changing the bit resolution or sampling frequency of audio or other information signals, between different stages of a signal processing chain. In ΣΔ modulation, a band-limited analog or digital audio signal is converted into a stream of rectangular pulses or a bit stream, depending on whether the modulator output is analog or digital, respectively. The encoding can either be 1-bit or multibit (k-bit), the latter corresponding to $2^k - 1$ possible pulse amplitude levels. The information of the input audio signal, manifesting as changes in the signal's amplitude with time, is encoded in the ΣΔ signal as a pulse density varying with time. Particularly, a high signal amplitude is transcoded as a dense sequence of pulses, while a low signal amplitude is transcoded as a sparse sequence of pulses.

In ΣΔ, signal quantization is carried out with low-resolution quantizers, usually 1 to 5 bits, leading to high quantization noise levels [13]. The excessive in-band quantization noise of the ΣΔ signal is treated by oversampling and noise shaping, through which, a significant part of the noise energy is shifted to the out-of-band frequency range [13][14]. Particularly, oversampling extends the effective bandwidth of the ΣΔ signal well-beyond the frequency range of the input signal, thus distributing the quantisation noise energy along a wider frequency range. In addition, noise shaping provides a high-pass spectral profile to the quantization noise, leading to a further reduction of the noise energy in the in-band range. To achieve noise shaping, ΣΔ modulators entail negative feedback loops that involve integration and consequent quantization of the input signal. The number of feedback loops used in a particular ΣΔ implementation, known as the order of the modulator, determines the shape of the noise transfer function and, consequently, the SQNR in the in-band. Generally, a higher modulation order corresponds to a reduced total inband noise energy and a steeper slope of the high-pass profile (see ΣΔ modulator structure subsection).

Fig. 3.3 presents the block diagrams of the linearized models of a first-order and a second-order ΣΔ modulator in the discrete-frequency domain [14]. To mathematically describe the behavior of a linearized ΣΔ modulator, assume an oversampled Pulse-Code Modulation (PCM) input signal $x(n)$ with N number of samples. The discrete-time PCM-to-ΣΔ conversion can be described as a transformation $\mathrm{M}_{\Sigma\Delta}$ from $x(n)$ to the modulator output $y_{\Sigma\Delta}(m)$:

$$y_{\Sigma\Delta}(n) = \mathrm{M}_{\Sigma\Delta}\{x(n)\} \tag{3.1}$$

In the discrete frequency domain obtained by DFT, the output $Y_{\Sigma\Delta}(k)$ of the modulator can be written in terms of the input $X(k)$ as:

$$Y_{\Sigma\Delta}(k) = \mathrm{STF}(k) \cdot X(k) + \mathrm{NTF}(k) \cdot E(k) \tag{3.2}$$

where k is the discrete frequency index, $\mathrm{STF}(k)$ and $\mathrm{NTF}(k)$ are the noise and signal transfer functions of the modulator, respectively, and $E(k)$ is the quantization noise [13][14]. For a 1$^{\text{st}}$-order ΣΔ modulator, $\mathrm{STF}(k) = 1$ and $\mathrm{NTF}(k) = 1 - e^{-j\frac{2\pi}{N}k}$. Thus:

$$Y_{\Sigma\Delta}(k) = X(k) + (1 - e^{-j\frac{2\pi k}{N}}) \cdot E(k) \tag{3.3}$$

The spectral magnitude of the first order NTF can be written as:

$$|\mathrm{NTF}(k)| = 2 \cdot \left|\sin\left(\frac{\pi}{N}k\right)\right| \tag{3.4}$$

For the in-band frequencies, $k \ll \frac{N}{2}$ and, hence, $\frac{\pi}{N}k \ll 1$. As a result, Eq. (3.4) can be approximated by:

$$\left|\mathrm{NTF}\left(k \ll \frac{N}{2}\right)\right| \simeq \frac{2\pi}{N}k \tag{3.5}$$

Eq. (3.5) shows that the quantization noise of a first order ΣΔ modulator exhibits an approximate first order high-pass spectral profile in the in-band range. For such a modulator and with a full-scale sine wave input, the Signal-to-Quantization-Noise Ratio (SQNR) is given by:

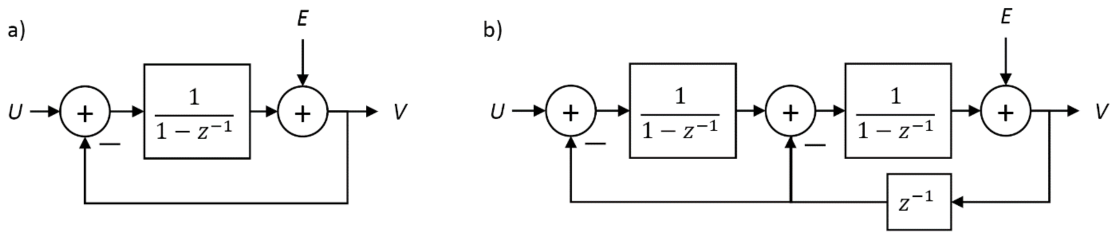

Fig. 3.3: z-domain block diagrams of the linearized models of a) a first-order and b) a second order ΣΔ modulator, where U, V the input and output signals respectively, E is the quantization error and $z = e^{-j\frac{2\pi}{N}k}$.

$$\text{SQNR} = \frac{9L^3}{2\pi^2}\ (\text{dB}) \tag{3.6}$$

where L is the oversampling ratio. The impact of the order of the modulator on the in-band quantization noise becomes apparent by comparison of the 1st-order to a 2nd-order modulator NTFs. The 2nd-order NTF takes the form:

$$\left|\text{NTF}^{(2)}(k)\right| = \left(2\sin\left(\frac{\pi}{N}k\right)\right)^2 \tag{3.7}$$

which reduces for the in-band frequencies to:

$$\left|\text{NTF}^{(2)}(k)\right| \approx \left(\frac{2\pi}{N}k\right)^2 \tag{3.8}$$

Since for f_{in}: $\frac{2\pi}{N}k \ll 1$ and by comparing Eq. (3.5) and (3.8) it becomes evident that:

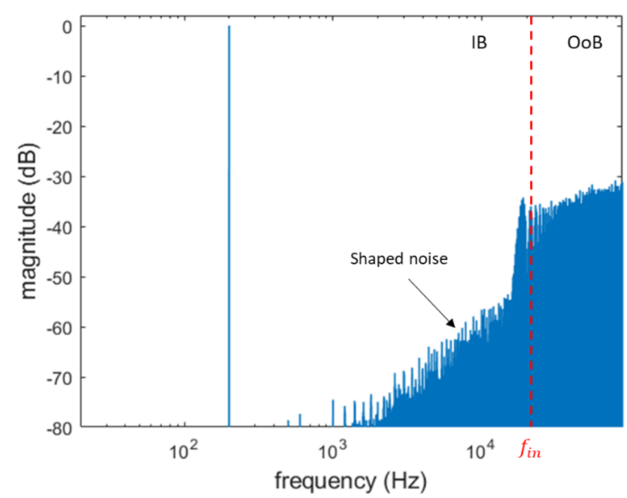

Fig. 3.4: DFT representation of a ΣΔ modulation signal generated from a sine wave input signal with frequency $f_{\text{sin}} = 200$ Hz and sampling frequency $f_s = 44.1$ kHz. The signal is modulated with a 1st-order modulator using 4x oversampling.

$$\left|\mathrm{NTF}^{(2)}(k)\right| < \left|\mathrm{NTF}^{(1)}(k)\right| \tag{3.9}$$

thus, the 2nd-order modulator achieves higher suppression of the quantization noise in the in-band range. This result can be generalized for nth-order modulators, under the assumption that the modulator's functionality is stable [13]. ΣΔ modulator stability will not be further discussed here.

As an example, Fig. 3.4 shows a $f_{\sin} = 200\ \mathrm{Hz}$ sine wave $x_{\sin}(n) = \frac{1}{2}\sin(2\pi f_{\sin} n t_s)$ with sampling frequency $f_s = 44.1\ \mathrm{kHz}$, $t_s = 1/f_s$ and quantized with 8-bit resolution, modulated using 1-bit 1st-order ΣΔ modulation and oversampling $M = 4$. In the figure, the characteristic noise shaping of 6 dB/oct slope can be seen. Moreover, the considerable noise energy residing in the in-band range is due to the low bit resolution and small oversampling factor.

3.2.2 Pulse Width Modulation

Pulse Width Modulation (PWM) is widely used in telecommunications, signal processing, digital audio technology and power systems. Common PWM applications are signal coding and transmission [26], wireless power transmission [27], electric motor control [28][29], optical data storage, audio amplifiers (Class-D digital amplifiers) [9][17][30], power electronics [31][32] and other. PWM encodes the amplitude of the modulating signal into the pulse duration of the modulated signal. Specifically, PWM signals constitute sequences of rectangular pulses with fixed amplitude but varying duty cycle, which depends on the instant amplitude of the modulating signal. In case of discrete-time and quantised modulating signals with k-bit resolution, the resulting PWM pulses are also quantised with k-bit resolution in the time domain, to account for the different signal amplitudes.

There are two main PWM categories: Natural-sampling PWM (NPWM), which is purely analog and is practically the most widely used form, and Uniform-sampling PWM (UPWM), which is mainly used in digital PWM systems and digital analysis of PWM signals. Both forms introduce strong out-of-band non-harmonic modulation products [16][17][29] which generally extend to very high frequencies. Moreover, in contrast to NPWM, UPWM exhibits harmonic distortion due to the quantisation of the pulse duration. The out-of-band modulation products constitute a problem in both NPWM and UPWM systems, since they often cause overheating and damage of components, non-linear behavior, noise through electromagnetic interference, etc. [33][34][35][36]. In many PWM applications, a low-pass filter is applied to remove the high frequency energy at the expense of increased cost, weight and dimensions of the system [8][37].

UPWM is particularly useful, due to its digital nature, in computational simulations and for this reason, this presentation focuses on UPWM signals. Nevertheless, under conditions presented in subsection 2.2.2.1, NPWM signals can be approximated by UPWM signals with sufficient precision, thus rendering UPWM suitable also for the study of analog PWM systems. To mathematically describe UPWM signals, let a discrete-time signal $x(n)\colon x(n) \in \left[-\frac{1}{2}, \frac{1}{2}\right], n \in [0, d-1]$, quantized with k-bit resolution, sampling frequency f_s, sampling period t_s and duration $t_d = d \cdot t_s$, be the input signal to a UPWM conversion process. The resulting discrete-time, double-edge uniform-sampling PWM signal $y(m): y(m) \in [0,1]$, $m \in [0, D-1]$, is a stream of square pulses of equal amplitude and varying width. A schematic representation of the conversion process from $x(n)$ to $y_{\text{PWM}}(m)$ is shown in Fig. 3.5. Each pulse of the PWM signal corresponds to a single sample of the modulating signal and is centered in the middle of the sampling interval t_s. The pulses take 2^k possible discrete widths, corresponding to the discrete amplitudes of x_n. Each pulse is represented by $M_p = 2 \cdot (2^k - 1)$ samples [17], with a sampling period $t_p = \frac{1}{2(2^\wedge k-1)} \cdot t_s$ and sampling frequency $f_p = 2 \cdot \left(2^k - 1\right) \cdot f_s = M_p\, f_s$. The total number of samples of the UPWM signal is $D = M_p d = \frac{t_d}{t_p}$ while its duration remains the same (t_d).

The UPWM pulses result from comparison of the instant amplitude of the modulating signal x_n with the amplitude of a triangular carrier s_{car} with fundamental frequency $f_{\text{car}} = f_s$ [1]. In order to be compared with s_{car}, x_n is upsampled to f_p (see Fig. 3.5)[2]. In the discrete frequency domain, x_n and y_m are described by the DFT vectors $X_k\!: k \in \left[0, \frac{d}{2} - 1\right]$ and $Y_{\text{PWM}}(k)\!: k \in \left[0, \frac{D}{2} - 1\right]$ respectively. The vectors X_k and Y_k have a frequency resolution $f_d = \frac{1}{t_d}$ and Nyquist frequencies $\frac{f_s}{2}$ and $\frac{f_p}{2}$ respectively. The frequency range up to $\frac{f_s}{2}$ is mentioned as the band of interest, or in-band range, whereas the range $\frac{f_s}{2} \leq f < \frac{f_p}{2}$ is mentioned as out-of-band range. The out-of-band components of Y_l are here treated distinctly for:

a. the **carrier frequencies**, namely the carrier fundamental frequency and its harmonics $f_c^m = m \cdot f_s$, $a \in \mathbb{N} : m \in \left[1, \frac{M_p}{2} - 1\right]$ and,

b. the **side frequencies** $f_{m,b}$, with $b \in \left(-\frac{d}{2}, \frac{d}{2}\right)$ defined as the out-of-band frequencies around the carrier harmonics (not to be confused with the modulation sidebands [16]).

To address an out-of-band frequency, the nearest carrier harmonic f_c^m and a frequency distance f^b from f_c^α is used, so that $f_{m,b} = f_c^m + f^b$. The related DFT index is written as $k_{m,b} = md + b$. Fig. 3.6 illustrates the DFT representation of the sine wave $x_{\sin}(n)$ modulated with PWM. In Fig. 3.6 a), the in-band and out-of-band components are separated by the frequency $\frac{f_s}{2}$ and the carrier components are marked with crosses. Fig. 3.6 b)-d) presents details from the spectra around the carrier fundamental $f_c = 44.1$ kHz (1^{st} harmonic) and 2^{nd} harmonic $f_c^2 = 88.2$ kHz. From [17][38], it is easy to see that the Fourier series coefficients $Y(k)$ of the UPWM signal $y(n)$ at a frequency $f = kf_p$ can be written as:

$$Y(k) = A_k \cdot \sum_{n=0}^{d-1} \sin\left(\frac{\pi k}{d} \cdot x_n + \frac{\pi k}{2d}\right) \cdot e^{-j\frac{2\pi k}{d}n} = A_k \cdot \sum_{n=0}^{d-1} \sin\left(\frac{\pi k}{d}\left(x_n + \frac{1}{2}\right)\right) \cdot e^{-j\frac{2\pi k}{d}n} \tag{3.10}$$

[1] Additional PWM oversampling is here neglected for simplicity, without loss of generality.

[2] A thorough description of the digital UPWM modulation process and signals can be found in Floros1998, Floros2007.

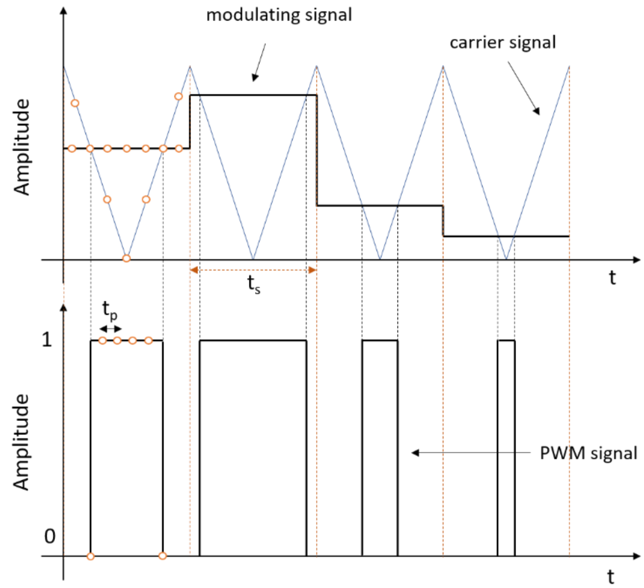

Fig. 3.5: Conversion of a digital modulating signal to a stream of discrete-time UPWM pulses by comparison to a triangular carrier [33][34].

where $A_k = \frac{1}{\pi k} e^{-j\frac{\pi k}{d}}$.

3.2.2.2 Approximating NPWM with UPWM

To understand the conditions under which UPWM signals approximate NPWM signals, the differences between the two modulations have to be analyzed. In NPWM, a time-limited analog modulating signal $x_a(t)$ has effectively an unlimited bandwidth which can potentially lead to spectral folding (aliasing) in the transition to the discrete-time domain. This issue can be addressed by limiting the energy of $x_a(t)$ within the band-of-interest, i.e. through low-pass filtering, so that the out-of-band spectral energy becomes almost negligible. It is well-known that in this case the analog signal $x_a(t)$ can be represented by a discrete-time signal x_n, with sampling frequency $f_s \geq 2f_{\text{in}}$. Moreover, the quantisation introduced in the digital representation of x_n induces quantisation error. However, with sufficiently high quantisation resolution, such errors can be negligibly small.

Most importantly, the leading and trailing edges of NPWM pulses are defined by the time instances at which the amplitude of the triangular carrier equals the amplitude of the modulating signal x_a. This, in contrast to UPWM, leads to pulses that are not centered around the middle of the sampling interval. The difference in duration between the n^{th} pulse of a UPWM and NPWM signal can be expressed as [17]:

$$E(n) = \left[\left(t_{\text{lead}}(n) - m_{\text{lead}}(n) \cdot t_p\right) + \left(t_{\text{trail}}(n) - m_{\text{trail}}(n) \cdot t_p\right)\right] \tag{3.11}$$

where $t_{\text{lead}}(n), t_{\text{trail}}(n)$ are the time instances of the leading and trailing edges of the n^{th} NPWM pulse and $m_{\text{lead}}(n), m_{\text{trail}}(n)$ the time indices of the respective UPWM pulse.

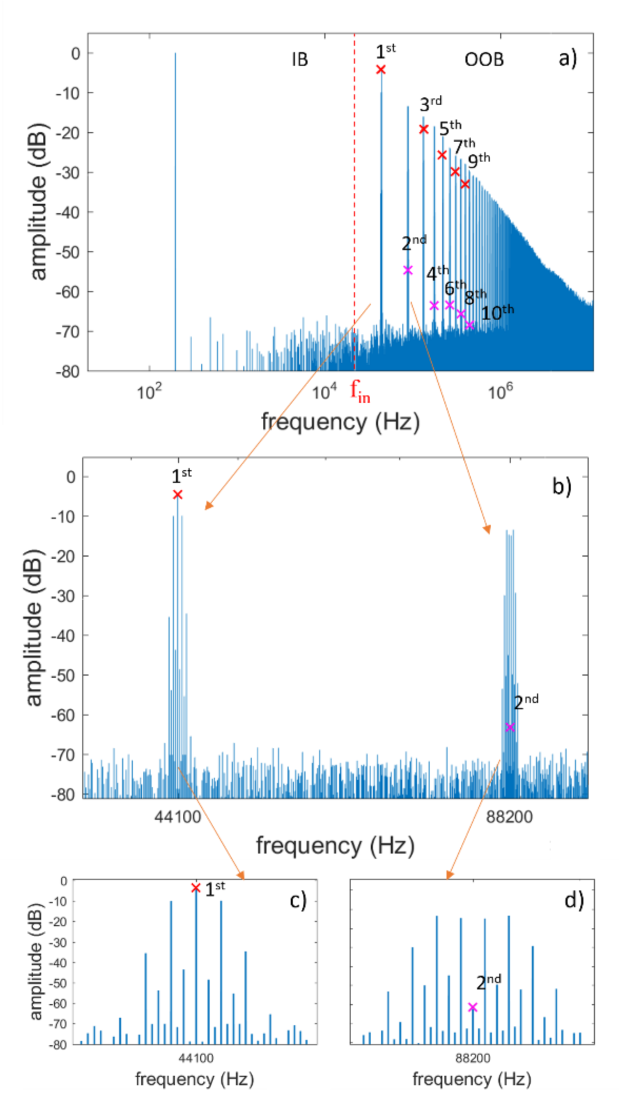

Fig. 3.6: DFT representation of a sinewave modulating signal with $f_{\sin} = 200\text{Hz}$, $f_s = 44.1\text{kHz}$ and 8-bit resolution. a) full DFT spectrum, b) detail from 1st and 2nd carrier harmonic, c) carrier fundamental and surrounding side frequencies and d) carrier 2nd harmonic and surrounding side frequencies. Odd/even harmonics marked with crosses.

Several methods have been proposed for the suppression of artefacts introduced by digital UPWM [17][39][40]. Here, a method based on the Asymmetric UPWM (A-UPWM) is briefly outlined. A-UPWM partially suppresses harmonic distortion, eliminating the even harmonics and effectively doubling the PWM carrier frequency without increase of the oversampling factor. This is achieved by using two consecutive instances of the input signal to calculate a virtual intermediate sample x_n^R that will define the trailing edge of the n^{th} UPWM pulse. It is easy to deduce that for A-UPWM, Eq. (3.11) can be written in terms of the digital modulating signal x_n and the corresponding analog signal $x_a(t)$ as:

$$E(n) = \frac{T_p}{2} \cdot \left[\left(x_n - x_a\left(t_{\text{lead}}(n)\right)\right) + \left(x_a(t_{\text{trail}}(n)\,) \ - x_n^R\right)\right] \tag{3.12}$$

$E(n)$ can be minimized by adding appropriately calculated noise (dither) to the analog input signal. The noise signal is continuous-time, k-bit quantised and is calculated so that the difference between the resulting dithered digital signal x_n' and the dithered analog signal $x_a'(t)$ is reduced to the level of quantisation noise:

$$\left| x_n' - x_a'\left(t_{\text{lead}}(n)\right)\right| \le \frac{LSB}{2} \tag{3.13}$$

For more details on the method, see [17].

3.2.3 Pulse Amplitude Modulation

Pulse Amplitude Modulation (PAM) is a type of analog or digital modulation that is widely used in telecommunications applications and audio technology. Its most prominent uses are the Ethernet communications protocol and digital television [18], while in audio technology PAM has been adopted in class-D amplifiers [41] as well as the conversion of voice signals into PCM signals [18], among others. In Pulse Amplitude Modulation, the information of the modulating signal is encoded as a stream of pulses, whose amplitude is proportional to the instant amplitude of the input signal. PAM can exhibit either continuous (analog) or quantized (digital) amplitude levels, while it can also be continuous-time or discrete-time. Discrete-time PAM is commonly represented as a stream of impulses with varying amplitude.

The generation of a discrete-time PAM signal $y(m)$ with $m = 0,1, \ldots D - 1$ from an input signal $x(n)$, with $n = 0,1, \ldots d$ can be seen as the result of zero expansion of the signal $x(n)$ by a factor M. Mathematically, the zero expansion can be expressed in terms of a stream of impulses:

$$s_\delta(m) = \sum_p \delta(m - pM) \tag{3.14}$$

with $p = 0,1, \ldots, d$ as [42]:

$$y_{\text{PAM}}(m) = \sum_p x(p)\delta(m - pM) \tag{3.15}$$

The PAM signal $y(m)$, is itself a stream of impulses appearing every M samples, where the amplitude of the l^{th} pulse equals the amplitude of the input signal for $n = p$. As in Pulse Width Modulation, if the sampling frequency of $x(n)$ is f_s, the sampling frequency of $y_{\text{PAM}}(m)$ is $f_p = Mf_s$. Moreover, the DFT $Y_{\text{PAM}}(k) = \mathcal{F}[y_{\text{PAM}}(m)]$ of the modulated signal can be derived from Eq. (3.15):

$$
\begin{aligned}
Y_{\mathrm{PAM}}(k) &= \mathcal{F}\left[\sum_p x(p)\delta(m-pM)\right] = \sum_p x(p)\mathcal{F}[\delta(m-pM)] \\
&= \sum_p x(p)\sum_m \delta(m-pM)\cdot e^{-j\frac{2\pi}{D}mk} = \sum_p x(p)\cdot e^{-j\frac{2\pi}{D}pMk} \\
&= \sum_p x(p)\cdot e^{-j\frac{2\pi}{D}pMk}
\end{aligned} \tag{3.16}
$$

Since $D = Md$, we get:

$$
Y_{\mathrm{PAM}}(k) = \sum_p x(p)\cdot e^{-j\frac{2\pi}{d}pk} = X(k) \tag{3.17}
$$

Equation (3.17) shows that the PAM signal has the same DFT spectrum as the input signal, however, there is a difference that needs to be highlighted. Upsampling increases the sampling frequency by M times and thus leads to an M-times extended DFT spectrum. Since the DFT is periodic, images of the input signal's spectrum beyond the Nyquist frequency reside now within the Nyquist frequency range of the PAM signal.

Fig. 3.7 illustrates this aspect for a sine wave input of 10 kHz, quantized with 8-bit resolution and sampled at 44.1 kHz, thus having a Nyquist frequency of 22.05 kHz. The PAM signal is upsampled by $M = 4$ and its Nyquist frequency is 88.2 kHz. For demonstration purposes, the spectrum is shown here using linear frequency scale. It becomes evident that the spectral images residing in the out-of-band range of the input signal, appear in the spectrum of the PAM signal at the frequencies:

$$
f_{1,2} = 44.1\ \text{kHz} \pm 10\ \text{kHz} = 34.1\ \text{kHz and } 54.1\ \text{kHz}
$$

as well as:

$$
f_3 = 88.2\ \text{kHz} - 10\text{kHz} = 78.2\ \text{kHz}
$$

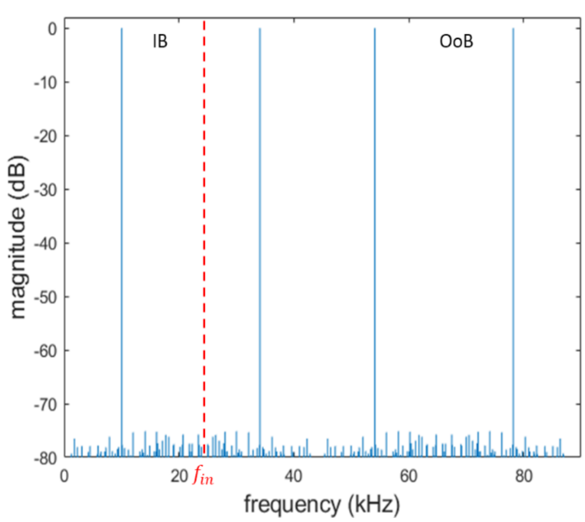

Fig. 3.7: DFT representation of a Pulse Amplitude Modulation signal generated by 4-times upsampling of a sine wave input signal with frequency $f_{\sin} = 10\ \text{kHz}$ and sampling frequency $f_s = 44.1\ \text{kHz}$.

3.3 UPWM spectra from random input signals

Here, it is demonstrated that when the input signal x_n is a random ergodic signal and its samples are independent and identically distributed (iid) random variables (RV), the expected value of the coefficients Y_k can be directly evaluated from the statistics of the amplitude distribution of x_n, without knowledge of the particular time-series of the input signal. Note that, if the input signal is random, the DFT coefficients are random variables as well, and in this respect, their statistical properties need to be identified.

In order to determine the statistical properties of the DFT coefficients of UPWM signals generated by random input signals, it is necessary to differentiate between the coefficients corresponding to the carrier harmonics and the side frequencies.

3.3.1 Carrier harmonics

Starting from the carrier harmonics for which the DFT index takes the values $k = md,\ m \in \mathbb{N}^*$, Eq. (3.10) becomes:

$$Y_m(\theta) = A_m \cdot \sum_{n=0}^{d-1} \sin\left(\pi m (x_n(\theta) + \frac{1}{2})\right) \cdot e^{-j2\pi mn} \tag{3.18}$$

where $A_m = \frac{(-1)^m}{\pi md}$ and θ denotes random variables. By adopting the vector notation for the signal samples $x_n(\theta)$:

$$\boldsymbol{X_d}(\theta) = [x_0(\theta)\ x_1(\theta) \dots x_{d-1}(\theta)]^t$$

and since $e^{-j2\pi mn} = 1$, Eq. (3.18) can be written as:

$$Y_m(\theta) = \frac{(-1)^m}{\pi m} \frac{< \mathbf{1}, \boldsymbol{V}_d^m(\theta) >}{d} \tag{3.19}$$

with <,>, **1** denoting the inner product operator and an all-ones vector of length d, respectively, and

$$\boldsymbol{V}_d^m(\theta) = [v_0^m(\theta)\ v_1^m(\theta) \dots v_{d-1}^m(\theta)]^t] = \sin\left(\pi m \left(\boldsymbol{X_d} + \frac{1}{2}\right)\right)$$

The expected value $\mu_{Y_m} = \mathbb{E}[Y_m(\theta)]$ of the DFT coefficients $Y_m(\theta)$ becomes:

$$\mu_{Y_m} = \frac{(-1)^m}{\pi m} \frac{\mathbb{E}[< \mathbf{1}, \boldsymbol{V}_d^m(\theta) >]}{d} \tag{3.20}$$

It is known that, the expected value μ_{v_c} of the linear combination v_c of d identically distributed random variables v:

$$v_c(\theta) = c_0 v_0(\theta) + c_1 v_1(\theta) + \cdots + c_{d-1} v_{d-1}(\theta)$$

is given by:

$$\mu_{v_c} = \mathbb{E}[\mu_{v_c}] = \sum_{n=0}^{d-1} c_n \mu_{v_n} = \mu_v \sum_{n=0}^{d-1} c_n \tag{3.21}$$

while the variance $\sigma_{v_c}^2$ is given by:

$$\sigma_{v_c}^2 = \mathbb{E}\left[\left(v_c(\theta) - \mu_{v_c}\right)^2\right] = \sum_{n=0}^{d-1} c_n^2 \sigma_{v_n}^2 = \sigma_{v_n}^2 \sum_{n=0}^{d-1} c_n^2 \tag{3.22}$$

Also, the inner product of $\boldsymbol{V}_d^m(\theta)$ with the unit vector $\mathbf{1},$ divided by the length d, can be written as:

$$\frac{< \mathbf{1}, \boldsymbol{V}_d^m(\theta) >}{d} = \frac{v_0^m + v_1^m + \cdots + v_{d-1}^m}{d} = \bar{v}^m \tag{3.23}$$

and hence:

$$\frac{\mathbb{E}[< \mathbf{1}, \boldsymbol{V}_d^m(\theta) >]}{d} = \mathbb{E}[\bar{v}^m] = \mu_{\bar{v}^m} \tag{3.24}$$

By using Eq. (3.21), Eq. (3.24) can be written as:

$$\frac{\mathbb{E}[< \mathbf{1}, \boldsymbol{V}_d^m(\theta) >]}{d} = \frac{1}{d} \sum_{n=0}^{d-1} \mu_{v^m} = \mu_{v^m} \tag{3.25}$$

and by substituting into Eq. (3.20), we get for the expected value μ_{Y_m} of the DFT coefficients:

$$\mu_{Y_m} = \mathbb{E}[Y_m(\theta)] = \frac{(-1)^m}{\pi m} \mu_{v^m} \tag{3.26}$$

Now, in order to investigate whether μ_{Y_m} is an unbiased estimator, the variance $\sigma_{Y_m}^2$ has to be calculated:

$$\sigma_{Y_m}^2 = \mathbb{E}[(Y_m(\theta) - \mu_{Y_m})^2] = \frac{1}{(\pi m)^2} \mathbb{E}\left[\left(\frac{< \mathbf{1}, \boldsymbol{V}_d^m(\theta) >}{d} - \mu_{v^m}\right)^2\right] \tag{3.27}$$

It can be seen that $\mathbb{E}\left[\left(\frac{<\mathbf{1}, \boldsymbol{V}_d^m(\theta)>}{d} - \mu_{v^m}\right)^2\right]$ is the variance $\sigma_{\bar{v}^m}^2$ of the random variable $\bar{v}^m$. From Eq. (3.22) it can be deduced that:

$$\sigma_{\bar{v}^m}^2 = \frac{\sigma_v^2}{d} \tag{3.28}$$

and thus, we get:

$$\sigma_{Y_m}^2 = \mathbb{E}[(Y_m(\theta) - \mu_{Y_m})^2] = \frac{1}{(\pi m)^2} \frac{\sigma_{v^m}^2}{d} \tag{3.29}$$

Since σ_v^2 is bounded, $\sigma_{Y_m}^2$ goes to zero as d goes to infinity:

$$\lim_{d \to \infty} \sigma_{Y_m}^2 = 0$$

Hence, it becomes apparent that $Y_m(\theta)$ are unbiased estimators of the mean values of the DFT coefficients of the PWM signal $y(m)$.

3.3.2 Side frequencies

On the side frequencies, Eq. (3.10) can be written by using the vector notation as:

$$Y_k(\theta) = e^{-j\frac{\pi k}{d}} \frac{d}{\pi k} \frac{< \boldsymbol{E}^k, \boldsymbol{V}_d^k(\theta) >}{d}, k = 0,1,\ldots,\frac{D}{2} - 1 \tag{3.30}$$

where $\boldsymbol{E}^k = [\varepsilon_0^k \ \varepsilon_1^k \ldots \varepsilon_{d-1}^k] = \left[1 \ e^{-j\frac{2\pi k}{d}} \ \ldots \ e^{-j\frac{2\pi k}{d}(d-1)}\right]$. According to Eq. (3.21), the expected value $\mu_{Y_k} = \mathbb{E}[Y_k(\theta)]$ of the DFT coefficient on the side frequencies takes the form:

$$\mu_{Y_k} = \mu_{v^k} \sum_{n=0}^{d-1} \varepsilon_n^k \tag{3.31}$$

where:

$$\mu_{v^k} = \mathbb{E}[v^k]$$

Moreover, the sum term is zero since:

$$\sum_{n=0}^{d-1} \varepsilon_n^k = \sum_{n=0}^{d-1} \left(e^{-j\frac{2\pi k}{d} n}\right)^k = 0$$

and hence:

$$\mu_{Y_k} = 0 \tag{3.32}$$

Again, to see if μ_{Y_k} is an unbiased estimator of the side frequency DFT coefficients, the variance $\sigma_{Y_k}^2$ has to be calculated:

$$\sigma_{Y_k}^2 = \mathbb{E}[(Y_k(\theta) - \mu_{Y_k})^2] = \mathbb{E}\left[\left|e^{-j\frac{\pi k}{d}} \frac{d}{\pi k} \frac{< \boldsymbol{E}^k, \boldsymbol{V}_d^k(\theta) >}{d}\right|^2\right] = \left(\frac{d}{\pi k}\right)^2 \mathbb{E}\left[\left|\frac{< \boldsymbol{E}^k, \boldsymbol{V}_d^k(\theta) >}{d}\right|^2\right] \tag{3.33}$$

Now, since:

$$\frac{\mathbb{E}[< \boldsymbol{E}^k, \boldsymbol{V}_d^k(\theta) >]}{d} = \mu_{w^k} = 0 \tag{3.34}$$

where $w^k = \frac{<\boldsymbol{E}^k, \boldsymbol{V}_d^k(\theta)>}{d}$, the term $\mathbb{E}\left[\left|\frac{<\boldsymbol{E}^k, \boldsymbol{V}_d^k(\theta)>}{d}\right|^2\right]$ can be written as:

$$\mathbb{E}\left[\left|\frac{< \boldsymbol{E}^k, \boldsymbol{V}_d^k(\theta) >}{d} - \mu_{w^k}\right|^2\right] = \frac{\sigma_{v^k}^2}{d^2} \sum_{n=0}^{d-1} |c_n^2| = \frac{\sigma_{v^k}^2}{d} \tag{3.35}$$

and finally:

$$\sigma_{Y_k}^2 = \frac{1}{\frac{\pi^2 k^2}{d}} \sigma_{v^k}^2 \tag{3.36}$$

However, $\frac{\pi^2 k^2}{d} = \pi^2 \left(m^2 d + 2mb + \frac{b^2}{d} \right)$ and:

$$\lim_{d \to \infty} \left(m^2 d + 2mb + \frac{b^2}{d} \right) \to \infty \tag{3.37}$$

from which it becomes evident that $Y_k(\theta)$ constitutes an unbiased estimator of the mean of $Y_k(\theta)$ since, when d goes to infinity, $Y_k(\theta)$ convergences in probability to the true mean value.

3.3.3 Closed-form formulas for common distributions

We have proved that $Y_k(\theta)$ are good estimators of the mean of the DFT coefficients of UPWM signals $\boldsymbol{Y}_D$ originating from random input signals $\boldsymbol{X}_d$ generated by iid random processes. In this subsection we show that, for particular distributions of the RVs $x_n(\theta)$ whose probability mass functions can be expressed in closed-form, the DFT coefficients $Y_m(\theta)$ can be expressed in terms of the parameters of the distribution, such as the variance. Starting from Eq. (3.18) and by using $e^{-j2\pi mn} = 1$, distinct expressions can be obtained for the odd and even values of m:

$$Y_m(\theta) = \frac{(-1)^m}{\pi m d} \cdot \begin{cases} \sum_{n=0}^{d-1} \cos\big(\pi m x_n(\theta)\big), & m_{odd} \\ \sum_{n=0}^{d-1} \sin\big(\pi m x_n(\theta)\big), & m_{even} \end{cases} \tag{3.38}$$

By Taylor expansion of the sinusoidal terms, we get:

$$Y_m(\theta) = \frac{(-1)^m}{\pi m d} \cdot \begin{cases} 1 + \sum_{n=0}^{d-1} \sum_{l=1}^{\infty} \frac{(-1)^l}{(2l)!} (\pi m)^{2l} \big(x_n(\theta)\big)^{2l}, & m_{odd} \\ \sum_{n=0}^{d-1} \sum_{k=1}^{\infty} \frac{(-1)^l}{(2l+1)!} (\pi m)^{2l+1} \big(x_n(\theta)\big)^{2l+1}, & m_{even} \end{cases} \tag{3.39}$$

and by exchanging the sums:

$$Y_m(\theta) = \frac{(-1)^m}{\pi m} \cdot \begin{cases} 1 + \sum_{l=1}^{\infty} \left(\frac{(-1)^k}{(2l)!} (\pi m)^{2l} \left(\frac{1}{d} \sum_{n=0}^{d-1} \left(x_n(\theta)\right)^{2l} \right) \right), & m_{odd} \\ \sum_{l=1}^{\infty} \left(\frac{(-1)^l}{(2l+1)!} (\pi m)^{2l+1} \left(\frac{1}{d} \sum_{n=0}^{d-1} \left(x_n(\theta)\right)^{2l+1} \right) \right), & m_{even} \end{cases}$$

$$= \frac{(-1)^m}{\pi m} \cdot \begin{cases} 1 + \sum_{l=1}^{\infty} \frac{(-1)^l}{(2l)!} (\pi m)^{2l} \mu_{x^{2l}} , & m_{odd} \\ \sum_{l=1}^{\infty} \frac{(-1)^l}{(2l+1)!} (\pi m)^{2l+1} \mu_{x^{2l+1}} , & m_{even} \end{cases} \quad (3.40)$$

where:

$$\mu_{x^j} = \frac{< \mathbf{1}, \left(x_d(\theta)\right)^j >}{d} \quad (3.41)$$

Equation (3.40) can be used to derive closed-form formulas when the RVs $x_n(\theta)$ follow normal, Laplacian, arcsine and uniform distributions. Nevertheless, the presented method is not limited to these distributions and can be applied to other distributions as well. The PMFs of the particular distributions are symmetric around the mean and have zero odd moments $\mu_{x^{2l+1}} = 0$. Thus, from Eq. (3.40) it becomes apparent that, for symmetrically distributed RVs $x_n(\theta)$, the resulting UPWM signals exhibit odd harmonics only. To derive the closed-form formulas for the odd harmonics, the even moments $\mu_{x^{2l}}$ are required, which can be approximated with the respective moments of the continuous distributions, considering fine quantization and sufficiently large observation window [43]. Note that, the amplitude of the quantized signals is effectively restricted within a limited range, thus, the present distributions are truncated in the tails. However, this aspect can be neglected considering that the vast majority of the PMF values lies within the quantization range. The adopted assumptions are also supported by the evaluation results presented in the next section, showing that the coefficients $Y_m(\theta)$ on the odd harmonics can be predicted with high accuracy from the closed-form formulas.

The n^th^ moment μ_{N^n} of the normal distribution are expressed in terms of the standard deviation as:

$$\mu_{N^{2l}} = \sigma_N^2 \cdot \ (2l-1)!!$$

and by substituting in Eq. (3.40), we get:

$$Y_m^{(N)}(\theta) = A_m d \cdot \left(1 + \sum_{l=1}^{\infty} (-1)^l \ (m\pi)^{2l} \cdot \frac{\sigma_N^2}{2l!!} \right), \qquad m_{odd} \quad (3.42)$$

which leads to:

$$Y_m^N(\theta) = \ A_m d \cdot (-1)^{\frac{m-1}{2}} \cdot e^{-\frac{m\pi\sigma_N^2}{2}}, \qquad m_{odd} \quad (3.43)$$

Respectively, for

- the Laplacian distribution: $\mu_{L^{2l}} = \sigma_L^{2l} \cdot 2l!$,
- the sinewave distribution $\mu_{S^{2l}} = \frac{(2l-1)!!}{(2l)!!}$,
- the uniform distribution $\mu_{U^{2l}} = \frac{v^{2l}}{(2l+1)!}$, where $v = (\alpha - c)/2$ and a, c the upper and lower limits of the uniform distribution.

The closed-form expressions that occur are written as:

$$Y_m^L(\theta) = A_m d \cdot (-1)^{\frac{m-1}{2}} \cdot \frac{1}{1 + (a \cdot m\pi)^2}, \qquad m_{odd} \tag{3.44}$$

$$Y_m^S(\theta) = A_m d \cdot J_0(m\pi), \qquad m_{odd} \tag{3.45}$$

$$Y_m^U(\theta) = A_m d \cdot \frac{\sin(m\pi v)}{m\pi v}, \qquad m_{odd} \tag{3.46}$$

Note that Eq. (3.45) agrees with the relation obtained by the double Fourier series method [15].

3.3.4 Simulation results

In this section, the results of the presented analysis are demonstrated and validated via computational evaluation of the DFT of UPWM signals originating from random input signals. Particularly, the effect of the statistical dependence of the input signal's samples on the UPWM signal's DFT is investigated. The effect of the size of the observation window on the side frequency components of the UPWM signal's DFT is demonstrated. Moreover, the accuracy of the closed-form formulas presented in section 3.3 is evaluated by comparison to direct computational evaluations via DFT. Ultimately, an application of the presented analysis is demonstrated where the DFT components of UPWM signals originating from different speech signals is predicted from the close-form formula of Eq. (3.44), by assuming statistical independence of the signal's samples. All signals used for the evaluations were sampled at 44.1 kHz and quantized with 8-bit resolution.

3.3.4.1 The effect of statistical dependence

We assume two signals whose samples follow the arcsine distribution, the histogram of which is shown in Fig. 3.8. The first signal $x_{\sin}$ is a sine wave with $f_{\sin} = 200$ Hz and is shown in Fig. 3.8 b). The signal $x_{\sin}$ is deterministic and thus, statistical independence between its samples does not hold. The second signal $x_r(\theta)$ is a noise signal obtained via random rearrangement of the samples of the sine wave signal $x_{\sin}$ and is shown in Fig. 3.8 c). The signal $x_r(\theta)$ has a zero autocorrelation function and its samples are statistically independent. The two signals are used as inputs in a UPWM conversion process, generating the UPWM signals $y_{\sin}$ and $y_r(\theta)$ respectively. The discrete Fourier transform of the UPWM signals are shown in Fig. 3.8 d) and e), where it becomes apparent that the DFT coefficients on the carrier harmonics are the same for both signals. This indicates that statistical dependence of the samples of the input signal does not affect the DFT coefficients of the carrier harmonics. However, the two signals differ significantly on the DFT coefficients of the side frequencies: the sinewave signal has prominent components on particular side frequencies (see also Fig. 3.6), whereas the random signal does not exhibit prominent side frequency components and has a noise-like side-frequency DFT spectrum.

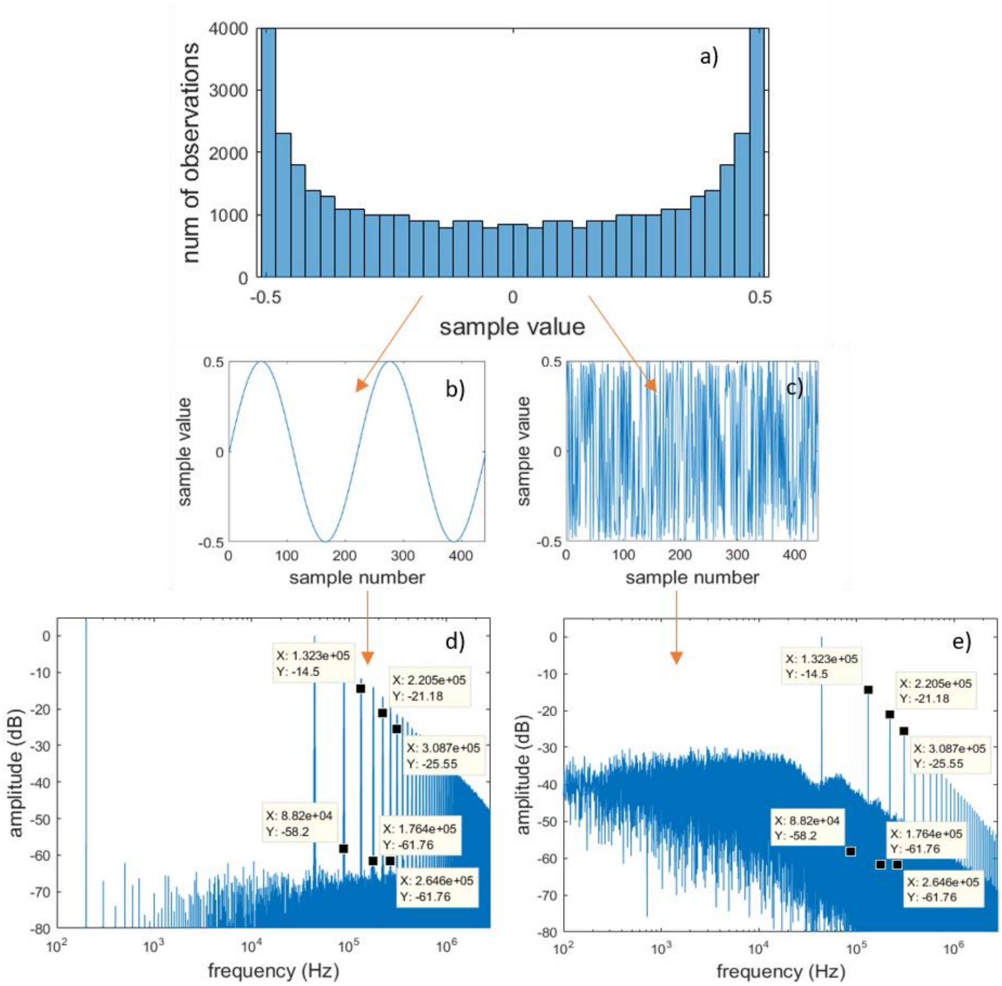

Fig. 3.8: a) Histogram of an arcsine distribution, from which b) a deterministic sine wave signal and c) a random noise signal are generated; d) and e) show the computationally evaluated discrete Fourier transforms of the sine wave and random noise signals respectively.

3.3.4.2 The effect of the observation window size

In subsection 3.3.2 it was shown that the RVs $Y_k(\theta)$ of a UPWM signal $\boldsymbol{Y}_D(\theta)$ generated from an input signal $\boldsymbol{X}_d(\theta)$ with iid RVs $x_n(\theta)$ have a zero mean (Eq. (3.32)). Moreover, it was proven that $Y_k(\theta)$ are good estimators of the DFT coefficients of $\boldsymbol{Y}_D(\theta)$ and their value tends to the mean with increasing size of the observation window. This aspect is demonstrated here by computational evaluation of the DFT of $\boldsymbol{Y}_D(\theta)$ generated from such a random input signals $\boldsymbol{X}_d(\theta)$ with different PMFs, particularly Normal, Laplacian, arcsine and uniform distributions [44]. The results are presented in Fig. 3.9, where the out-of-band DFT spectra of the signals Y_D are shown for two observation windows with $d_1 = 4410$ samples and $d_2 = 44100$ samples, corresponding to 0.1 and 1 second respectively. The energy of the signals is kept constant in order for the results to be comparable.

From Fig. 3.9 it becomes evident that for all signals the DFT coefficients $Y_m(\theta)$ on the carrier frequencies remain effectively unchanged with the change of the observation window, while the coefficients $Y_k(\theta)$ on the side frequencies are noticeably reduced. The computationally evaluated variance of the DFT coefficients on the side frequencies:

$$\sigma'_{Y_k} = \frac{2}{(M-1)d} \sum_{\substack{k=\frac{d}{2} \\ k \neq md}}^{\frac{D}{2}-1} \left(Y_k(\theta) - \bar{Y}_k(\theta)\right)^2 \tag{3.47}$$

was found to be reduced by a factor of 10 for the larger window, which is in accordance with the predictions of Eq. (3.36). To demonstrate this aspect, the mean change in the variance of the DFT

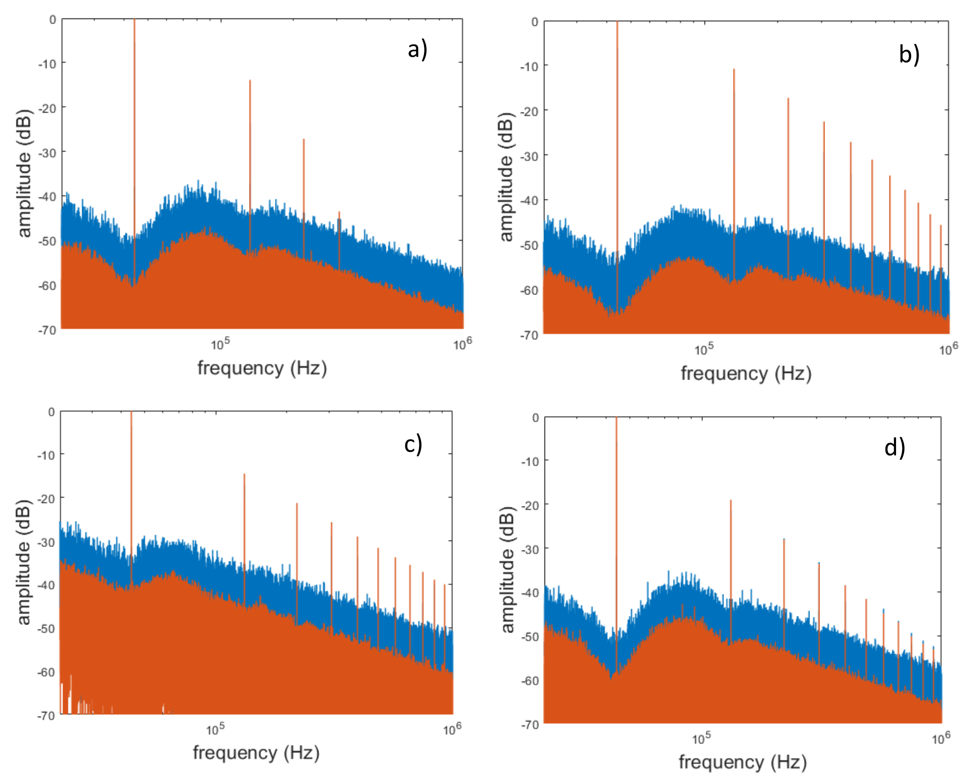

Fig. 3.9: DFT spectra of squared UPWM signals generated from input signals with a) normal, b) Laplacian, c) arcsine and d) uniform distributions, evaluated for two different observation windows, $d_1 = 4410$ (blue) and $d_2 = 44100$ samples (red).

coefficients over a frequency range $[-\frac{d}{2}, \frac{d}{2}]$ around a carrier harmonic f_m is estimated, by calculation of the integral:

$$\frac{1}{d}\int_{-\frac{d}{2}}^{\frac{d}{2}} \pi^2\left(m^2 d + 2mb + \frac{b^2}{d}\right) db = \pi^2\left(m^2 + \frac{1}{12}\right) d \tag{3.48}$$

According to Eq. (3.48), the relation of the mean variance $\bar{\sigma}_{c_l}$ of the DFT coefficients over the range $\left[-\frac{d}{2}, \frac{d}{2}\right]$ for window sizes d_1 and $d_2 = 10d_1$ becomes:

$$\frac{\bar{\sigma}_2}{\bar{\sigma}_1} = \frac{d_1}{d_2} = 0.1$$

proving that the variance of the side frequency DFT components is expected to reduce by 10 times via a tenfold increase of the observation window.

3.3.4.3 Non-symmetric distributions

In subsection 3.4.3 it was shown that the DFTs of UPWM signals originating from random input signals with symmetric probability mass functions around the mean, lack the even carrier harmonics (Eq. (3.40)). Here it is shown that asymmetry in the PMF leads to prominent even harmonics, whose magnitude depends on the level of asymmetry. To demonstrate this aspect, computational evaluations are presented for 5 different input signals with samples following different distributions of the Pearson family [45]. For the distributions, the following parameters were selected:

$$\mu = 0, \sigma = 1, \mu_{x^4} = 3$$

while the skewness μ_{x^3} took the values:

$$\mu_{x^3} = 0.2,\ \ 0.4,\ \ 0.6,\ \ 0.8,\ \ 1$$

For the signals, an observation window of 44100 samples was used, corresponding to 1 sec duration.

Fig. 3.11 a) shows the histogram of an input signal generated for $\mu_{x^3} = 0.8$ while Fig. 3.11 b) shows the DFT spectrum of the corresponding UPWM signal. It becomes evident that the skewed distribution exhibits prominent DFT coefficients on the even carrier harmonics, which were completely absent in the symmetric distributions (see Fig. 3.9).

Moreover, Fig. 3.10 shows the magnitude (in dB) of the DFT coefficients on the 4 first even harmonics for the 5 different UPWM signals, normalized with respect to the coefficient of the carrier fundamental. Generally, the coefficients are amplified with increasing skewness, with the only exception being the coefficient of the 8th harmonic for $\mu_{x^3} = 0.8$, which could potentially be due statistical error. Although the results for the particular distribution show an increase in the even harmonics with increasing skewness, no generalization can be made for other skewed distributions.

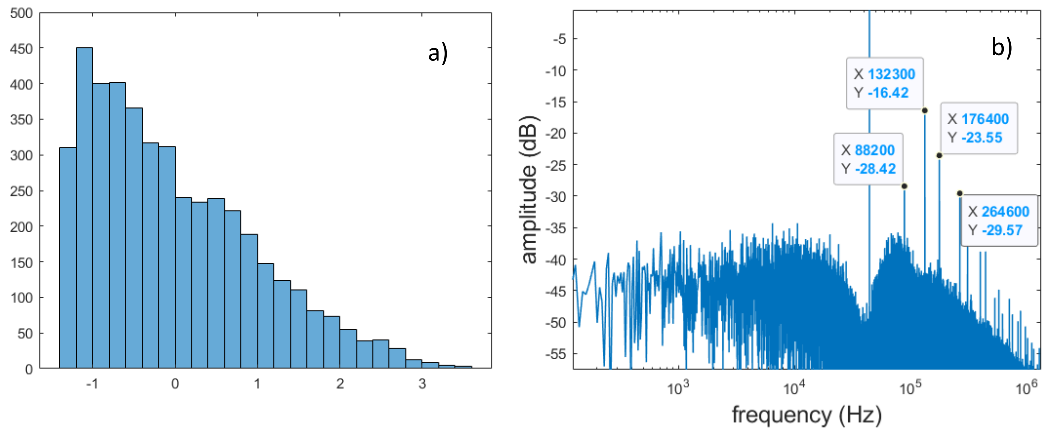

Fig. 3.11: a) histogram of a signal $\boldsymbol{X}_d$ with samples following a Pearson distribution with parameters $\mu = 0, \sigma = 1, \mu_{x^3} = 0.8,\ \mu_{x^4} = 3$ and b) DFT spectra of the UPWM signal generated from $\boldsymbol{X}_d$.

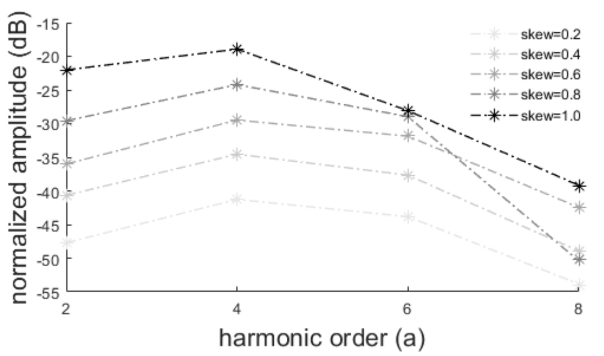

Fig. 3.10: DFT coefficients (in dB) of the even carrier harmonics of five UPWM signals generated by an equal number of random input signals whose samples follow Pearson distributions with parameters $\mu = 0, \sigma = 1, \mu_{x^4} = 3$and $\mu_{x^3} = 0.2,\ \ 0.4,\ \ 0.6,\ \ 0.8,\ \ 1.$

3.3.4.4 Closed-form formulas

Table I summarizes the results from the evaluations of the harmonic DFT components $Y_m(\theta)$ of UPWM signals originating from input signals with arcsine, normal, Laplace and uniform distributions, while the diagrams of the DFTs are also shown in Fig. 3.9. The values in the table correspond to the magnitude in dB of the DFT coefficients of the first 4 odd carrier harmonics (3, 5, 7 and 9) and are normalized for each signal with respect to the coefficient of the fundamental frequency. From the table it can be seen that the results of the DFT are almost equal to those of the closed-form formulas, with deviations less than 1 dB. The DFT evaluations are susceptible to statistical error, since they are based on a single realization of the random process, whereas the closed-form evaluations are based on the true values of the generating processes' statistical parameters, here the variance, and do not depend on the particular realization. The very good agreement between DFT and closed-form evaluations demonstrates that, when the input signal's samples are iid RVs with known distribution, the DFT spectra of the UPWM signal observed within a sufficiently large window can be calculated from the distribution's statistical parameters, given an ergodic generating process. If the input signal's samples are not iid RVs, only the DFT coefficients on the carrier harmonics can be calculated from the distribution's statistical parameters.

Moreover, UPWM signals transcoded in real PWM systems often originate from input signals with typical sample distributions. Such examples are audio signals of speech or music. Speech signal samples, in particular, are considered to be well described by the Laplacian distribution, as documented in several works [46][47]. Speech signals do not exhibit zero autocorrelation and thus, their samples cannot be considered iid RVs. As a result, Eq. (3.32) does not hold and the DFT components $Y_k(\theta)$ of the side frequencies cannot be predicted from the statistics of the input signal. Nevertheless, it is demonstrated that the DFT components $Y_m(\theta)$ on the carrier harmonics, and particularly the odd harmonics which are dominant in the out-of-band UPWM spectra of such signals, can be predicted from the Laplacian closed-form formula with sufficient accuracy.

Table 1: Amplitude (dB) of the carrier harmonics evaluated via the closed-form formulas

Signal	Harmonic Order (α)							
	3		5		7		9	
	DFT	Eq	DFT	Eq	DFT	Eq	DFT	Eq
Sine	-14.5	-14.0	-21.2	-20.7	-25.5	-25.0	-28.9	-28.3
Normal	-13.1	-13.0	-24.6	-24.4	-38.2	-37.7	-54.7	-53.8
Laplace	-10.8	-11.0	-17.3	-17.8	-22.6	-23.4	-27.1	-28.2
Uniform	-19.2	-19.1	-27.8	-28.0	-33.9	-33.8	-37.8	-38.2

To demonstrate this aspect, a female speech extract with duration of 5 sec is used, taken from the Archimedes anechoic audio library [48]. The histogram of the extract is calculated and fitted via a Laplace function, to determine the distribution's width parameter. Then, the coefficients $Y_m(\theta)$ are calculated from Eq. (3.44) and the results are compared with the direct calculation of the UPWM signal's DFT. Fig. 3.12 a) shows the histogram's envelope and the fitting curve of the first extract, while Fig. 3.12 b) shows the DFT spectrum of the respective UPWM signal. In Fig. 3.12 b), the prominence of the odd carrier harmonics becomes evident. Even carrier harmonics are also present, however, they are significantly suppressed compared to the odd harmonics. Finally, Fig. 3.12 c) presents the comparative results of the DFT coefficients via DFT of the UPWM signal and via the closed-form formula of Eq. (3.44). It can be seen that the Laplace formula predicts the coefficients $Y_m(\theta)$ of the odd carrier harmonics with high accuracy, proving that the proposed analysis can be also applied in real PWM systems.

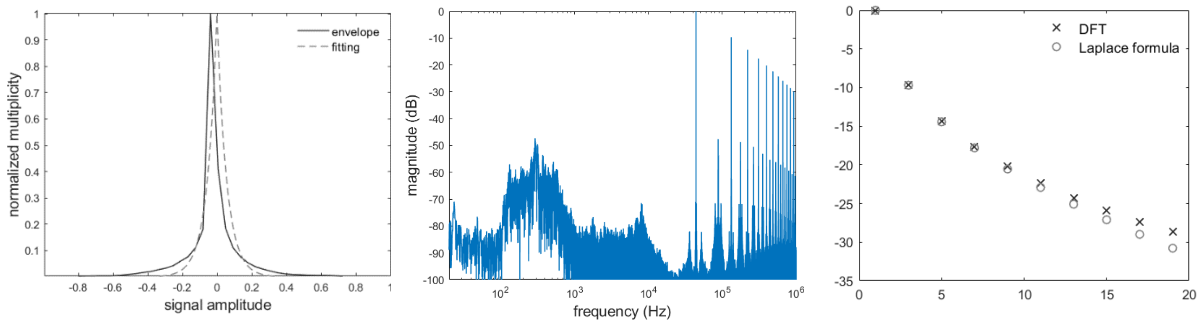

Fig. 3.12: a) Envelope and Laplace fitting curve of the histogram and b) computationally evaluated DFT spectrum of a 5s female speech extract; c) comparative estimation of the DFT coefficients via DFT of the UPWM signal and via the closed-form Laplace formula.

Conclusions

This Chapter covered fundamental aspects of current sound reproduction technology and the basic concepts of pulsed audio modulations that are widely used in modern sound reproduction systems. Moreover, it outlined the structure of a sound reproduction chain based on a laser-plasma transducer and compared it to state-of-the-art class-D amplification and reproduction chains. Particularly, the basic concepts of ΣΔ modulation, Pulse Width Modulation and Pulse Amplitude Modulation were presented, which are the most widely adopted techniques in current sound reproduction systems based on class-D amplifiers and are of interest for the development of laser-sound transducers. The time- and frequency-domain representations of these modulations were analytically presented, with emphasis to the distinction of the in-band (IB) and out-of-band (OoB) frequency range of the modulated signals. In all, three modulations, the frequency content of the input is effectively preserved in the in-band range of the modulated signal, thus requiring only low-pass filtering for the reconstruction of the original signal.

Moreover, the OoB spectral components of the ΣΔ, PWM and PAM, modulations were analyzed and compared for a sine wave, input showing significant differences. It was shown that, ΣΔ modulation, being the only purely quantized modulation among the tree, and having low-bit resolution, exhibits significant high-pass noise energy in the OoB spectrum, due to noise shaping. On the contrary, PAM being an analog modulation - although here simulated digitally - does not exhibit noise but instead exhibits mirrored images of the in-band content in the OoB spectrum. PWM exhibits modulation products in the OoB spectrum, generated by a highly complex intermodulation process. All three modulations have strong spectral components on the carrier frequencies.

Finally, a novel method for the analysis and derivation of the DFT of Uniform-sampling PWM signals originating from random PCM signals with independent and identically distributed samples was developed. Particularly, it was shown that the DFT coefficients of such UPWM signals in the out-band range can be calculated directly from the statistics of the generating random process; the obtained random variables are unbiased estimators of the true mean of the DFT coefficients, with their variance tending to zero when the signal observation window tends to infinity. Thus, it was demonstrated that the method enables the estimation of the UPWM DFT spectra without knowledge of the particular time-series of the input signal, given that the generating random process is ergodic. When the samples of the input signal are identically distributed but not independent, only the DFT coefficients on the harmonic frequencies of the PWM carrier can be calculated. Finally, it was shown that this approach allows for the derivation of closed-form expressions for the DFT coefficients when the samples of the input signal follow common distributions such as Gaussian, Laplacian, arcsine and uniform. The closed-form expression for the Laplacian inputs was used to estimate the DFT coefficients of a UPWM signal generated from a female speech excerpt, showing very high accuracy.

References

[1] Norsworthy, S. R. *Delta-Sigma Data Converters: Theory, design and simulation*. IEEE Press (1997)

[2] Harris, S. How to Achieve Optimum Performance from Delta-Sigma A/D and D/A Converters, Journal of the Audio Engineering Society, 41(10), 782-790 (1993)

[3] Gerfers, F., & Ortmanns, *M. Continuous-time sigma-delta A/D conversion: fundamentals, performance limits and robust implementations. Springer* (2011)

[4] Ritoniemi, T., Karema, T. & Tenhunen, H. A fifth order sigma-delta modulator for audio A/D-converter, International Conference on Analogue to Digital and Digital to Analogue Conversion, 153-158 (1991)

[5] Comminges, M., Dell'ova, F., Paillardet, F., Andre, E., Arndt, M. & Balestro, F. Embeddable CMOS 3.3 V 16 bits monobit and multibit delta-sigma digital to analog converter, Proceedings of International Conference on Consumer Electronics, 358-359 (1995)

[6] Wang, Y., Latency Measurements of Audio Sigma Delta Analog to Digital and Digital to Analog Converts, 131st AES Convention, Engineering Brief 25 (2011)

[7] Self, D. (2009). *Audio power amplifier design handbook (5th edition)*, Elsevier Ltd, Amsterdam (2009)

[8] *AN-1497 Filterless Class D Amplifiers*, Texas Instruments, Dallas (2013)

[9] Rumsey, F. Class D Power Amplification, Journal of the Audio Engineering Society, 57(12), 1087-1093 (2009)

[10] Kuo, C. & Lin, S. A delta-sigma modulator-based class-D amplifier, 2016 IEEE 5th Global Conference on Consumer Electronics, pp. 1-2 (2016)

[11] Tatlas, N.A., Kontomichos, F. & Mourjopoulos, J. Design and Performance of a Sigma Delta Digital Loud-speaker Array Prototype, Journal of the Audio Engineering Society, 57(1) (2009)

[12] S. Je et al., A Compact and Low-Cost MEMS Loudspeaker for Digital Hearing Aids, IEEE Transactions on Biomedical Circuits and Systems, 3(5), 348-358 (2009)

[13] Pavan, S., Schreier, R., & Temes, G. C. Understanding delta-sigma data converters. Hoboken, NJ: Wiley (2017)

[14] Janssen, E., & van Roermund, A. H. M. Basics of Sigma-Delta Modulation, in *Look-Ahead Based Sigma-Delta Modulation*. essay, Springer Netherlands (2011)

[15] Sun, J. Pulse-Width Modulation, in *Dynamics and Control of Switched Electronic Systems*, Springer, pp. 25-61 (2012)

[16] Song, Z. & Sarwate, D. V., The Frequency Spectrum of Pulse Width Modulated Signals, Signal Processing, 83(10), 2227–2258 (2003)

[17] Floros, A. & Mourjopoulos, J., Distortion-Free 1-Bit PWM Coding for Digital Audio Signals, EURASIP Journal on Advances in Signal Processing, 094386 (2007)

[18] Barry, J.R., Lee, E.A. & Messerschmitt, D.G. Pulse-Amplitude Modulation. in Digital Communication. Springer, Boston (2004)

[19] Rossing, T. D. Audio and Electroacoustics, in Springer handbook of acoustics, Springer (2007)

[20] Kleiner, M. *Electroacoustics,* Taylor & Francis (2013)

[21] Kaleris, K., Stelzner, B., Hatziantoniou, P., Trimis, D. & Mourjopoulos, J. Laser-sound: optoacoustic transduction from digital audio streams. Sci Rep 11, 476 (2021)

[22] Kaleris, K., Stelzner, B., Hatziantoniou, P., Trimis, D. & Mourjopoulos, J. Laser-sound: audio reproduction from digital ΣΔ streams, under review

[23] Boyd, R. W., *Nonlinear Optics, 3rd ed.*, Academic Press, Inc., Orlando, FL (2008)

[24] Melchior, V. High-resolution audio: a history and perspective. J. Audio Eng. Soc. 67(5), 246–257 (2019)

[25] Nuijten, P., Reefman, D. Why Direct Stream Digital (DSD) is the best choice as a digital audio format, AES Convention 110, 5396 (2001)

[26] Hausmair, K., Chi, S., Singerl, P. & Vogel, C. Aliasing-free digital pulse-width modulation for burst-mode rf transmitters, IEEE Transactions on Circuits and Systems I: Regular Papers, 60(2):415–427 (2013)

[27] Yin, M. & Ghovanloo M. Using pulse width modulation for wireless transmission of neural signals in a multichannel neural recording system. ISCAS IEEE International Symposium, 17:354–363 (2009)

[28] Wang, Y. Zhao, C., Zhang, L., Liu, C. & Li, J. High-Efficiency Pulse Width Modulation-Based Wireless Laser Power Transmission Step-Down System, in IEEE Photonics Journal, 12(2), 1-14 (2020)

[29] Guinee, R. A., & Lyden, C. A novel modulated single fourier series time function for mathematical modelling and simulation of natural sampled pulse width modulation in high performance brushless motor drives, 42nd IEEE International Conference on Decision and Control, Maui, (2003)

[30] Attwood, B. E., Design parameters important for the optimization of very-high-fidelity pwm (class d) audio amplifiers. J. Audio Eng. Soc., 31:842–853 (1983)

[31] Monmasson, E., *Power electronic converters: Pwm strategies and current control techniques*, ISTE/Wiley (2011)

[32] Do, DT & Nguyen, MK. Three-level quasi-switched boost t-type inverter: Analysis, pwm control, and verification, IEEE Trans. Ind. Electron., PP:1 (2018)

[33] Floros, A. & Mourjopoulos, J. A study of the distortions and audibility of pcm to pwm mapping, In Audio Engineering Society Convention 104 (1998)

[34] Floros, A. & Mourjopoulos, J. On the nature of digital audio pwm distortions. In Audio Engineering Society Convention 108 (2000)

[35] Kaleris, K. & Mourjopoulos, J. Dual-Band PWM for filterless class-D audio amplification, proceedings of the 144th Audio Engineering Society International Pro Audio Convention (2018)

[36] Hawksford, M. Modulation and system techniques in pwm and sdm switching amplifiers. J. Audio Eng. Soc, 54(3):107–139 (2006)

[37] He, H. Kang, Y., Yu, J., Guo, L. Ge, T. & Chang, J. A novel low-power high-efficiency 3-state filterless bang-bang class d amplifier. ICECS IEEE International Conference, 93–96 (2015)

[38] Floros, A. & Mourjopoulos, J. Analytic derivation of audio pwm signals and spectra, J. Audio Eng. Soc, 46(7/8):621–633 (1998)

[39] Mellor, P., Leigh, S. & Cheetham, B. Digital sampling process for audio class d, pulse width modulated, power amplifiers. IEE Proceedings, 138(4):441–448 (1991)

[40] Pascual, C. & Roeckner, B. Computationally efficient conversion from pulse-code modulation to naturally sampled pulse-width modulation, in Audio Engineering Society Convention 109, (2000)

[41] Ma, Tu-Hsien. Pulse Amplitude Modulation (PAM) Method and Circuit for Improving the Performance of a D-class Audio Amplifier. Princeton Technology Corp, assignee. Patent US20060103459A1. Nov.-Dec. 2004. Print

[42] Oppenheim, A. V., & Schafer, R. W. *Discrete-time signal processing,* Pearson (2014)

[43] Rapp, J. Dawson, R. M. A. & Goyal, V. K. Estimation from quantized gaussian measurements: When and how to use dither, IEEE Transactions on Signal Processing, 67, 3424–3438 (2019)

[44] Papoulis, A. *Probability and statistics* Prentice Hall (1990)

[45] King, M. *Statistics for process control engineers: a practical approach*, Wiley (2017)

[46] Gazor, S. & Zhang, W. Speech probability distribution, IEEE Signal Processing Letters, 10, 204–207 (2003)

[47] Jensen, J., Batina, I. Hendriks, R. C. & Heusdens, H. A study of the distribution of time-domain speech samples and discrete fourier coefficients, Proceedings of SPS-DARTS (2005)

[48] B&O, *Music For Archimedes,* Copenhagen: Hansen and Munch (1991)

Chapter 4

The correlation between sound and light radiation following nanosecond laser-induced breakdown in air

Contents

Introduction

In Chapter 2, the secondary emission of light and sound radiation following Laser-Induced Breakdown (LIB) in ambient air by short or ultrashort pulses was discussed, while from previous works there has been some evidence that there is a correlation between the pressure wave and the secondary light emitted from the laser-matter interaction volume following laser-induced breakdown (LIB) in the air [1][2][3]. In this Chapter, a novel experimental and computational method for the joint study of the LIB secondary radiative phenomena is presented and utilized for the development of a phenomenological model clearly demonstrating the correlation between the emitted optical and acoustic signals. Specifically, the methodology and results from simultaneous measurements of these signals generated by nanosecond laser pulses of different energies are presented. In contrast to most existing works, the measurements presented here are carried out over time windows that are long enough to cover the complete temporal behavior of the radiative phenomena starting with the plasma formation up to the complete cooldown of the interaction region. From the measured optical signal, the contribution of the thermal radiation is isolated and reconstructed using signal processing techniques. The analysis shows that the thermal optical radiation and the acoustic radiation evolve at the same time scales, a fact that demonstrates the well-known thermoelastic nature of the LIB-generated sound waves. Based on these findings, a phenomenological model is developed which allows for the calculation of the frequency spectra of a LIB acoustic pulse from the thermal radiation signal. The model's evaluations show good agreement with the experimental measurements for different energies of the laser pulse, proving that the sound wave following LIB can be directly evaluated from the respective optical radiation emitted from the interaction region.

4.1 Study of light and sound radiation following Laser-Induced Breakdown in air

The joint study of the secondary radiative phenomena following LIB combines experiments and signal processing techniques and leads to the development of a phenomenological physical model that allows for the estimation of the frequency spectra of the laser generated acoustic pulses from the light signal following LIB. Both the experiments and the model development were a result of the collaboration with the Institute of Plasma Physics and Lasers (IPPL) of the Hellenic Mediterranean University (HMU). An overview of the methodology is presented below and is schematically depicted in Fig. 4.1.

(EXP) In the experiments, the LIB light and sound signals generated by laser pulse streams of different energies are simultaneously captured and recorded. Particularly, the ***acoustic signals*** $s_{\mathrm{mic}}(t)$ are captured by a special microphone with broad frequency response and are routed to a high-sampling rate audio interface which converts them to digital streams. The streams are recorded in a Digital Audio Workstation (DAW). At the same time, the ***optical signals*** $s_{\mathrm{ph}}(t)$ are captured by an ultrafast and broadband photodiode and are routed to a digital oscilloscope, where they are digitized and stored.

(SP) The ***acoustic signals*** $s_{\mathrm{mic}}(t)$ are analyzed in order to segregate single LIB acoustic pulses from the pulse stream. For the derivation of a representative single pulse, averaging over multiple pulses can be used if appropriate. Consequently, the frequency spectra $S_{\mathrm{LIB}}(\omega)$ of single LIB acoustic pulses are calculated using the discrete Fourier transform (DFT). The same segregation approach is used for the recorded ***optical signals*** $s_{\mathrm{ph}}(t)$, where averaging can be directly imposed in the oscilloscope. From the optical signal corresponding to a single breakdown event, the thermal signal $s_{\mathrm{H}}(t)$ is estimated by removing the non-thermal optical components using signal processing techniques.

(PM) Finally, the results of the experimental and signal processing procedures are utilized for the development of the physical model that effectively correlates the light and the sound radiation that follows laser induced breakdown. The model is based on the linear wave equation and uses the derived thermal signal $s_H(t)$ as a heat source. The model's solution in the frequency domain gives the frequency spectra $S_{\mathrm{LIB}}(\omega)$ of the LIB acoustic pulses and is validated by comparison with the measured acoustic spectra. The good agreement between the model's predictions and the experimental results proves the correlation between the light and the sound emitted in LIB, demonstrating that the sound can be derived from the light signal and, vice versa, the deposited heat can be estimated from the acoustic pulse.

4.1.1 Experiments

The experimental setup used for capturing the LIB light and sound signals is also shown in Fig. 4.1. The laser system was a Quantel Brilliant-B Nd:YAG laser [4], delivering 6 ns optical pulses with energy from

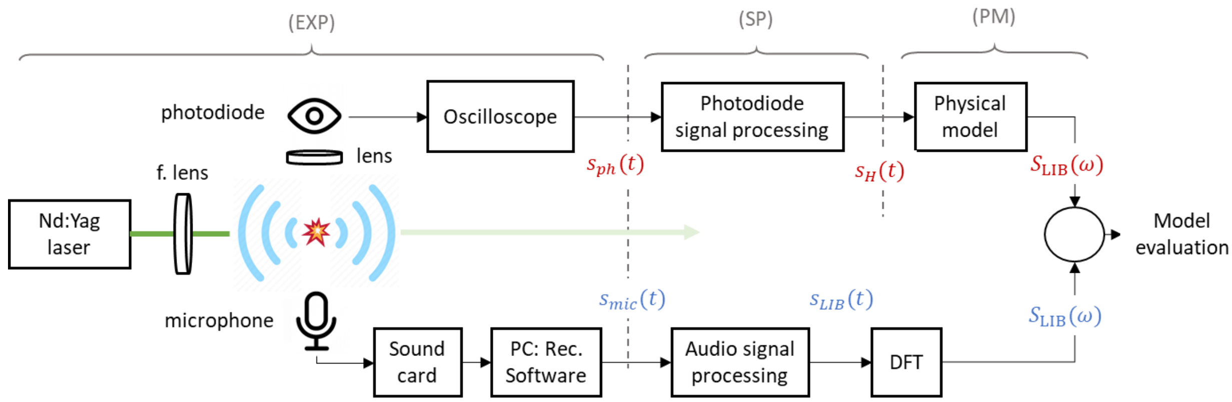

Fig. 4.1: Methodology and experimental setup for the simultaneous recording of the sound and light generated in air laser-induced breakdown, the processing of the recorded signals and the development and evaluation of the physical model.

40 mJ to 100 mJ at 532 nm wavelength (second harmonic). For the experiments, a pulse repetition rate of 2 Hz was selected, ensuring that the time window between two consecutive pulses $\Delta t = 0.5$ s is

sufficiently large for the complete phenomenon to evolve [5][6][7]. The large window also ensured that possible room reflections induced by one pulse do not interfere with the next pulse, so that they can be eliminated in post processing if required. The initial diameter of the laser beam was 9 mm and it was focused with a 75 mm lens. The estimated beam diameter at the focal spot was ~ 17 μm resulting to peak laser intensities between $\sim 3.0 \times 10^{12}$ W/cm^2 and $\sim 7.5 \times 10^{12}$ W/cm^2 for the 40 mJ and 100 mJ pulses respectively. Note that the air breakdown threshold for these conditions is approximately 4.0×10^{11} W/cm^2, which is well-below the used intensities [8][9]. The abundance of optical intensity renders the breakdown and the secondary radiative phenomena more repeatable, since close to the threshold, small deviations in the optical intensity might result to large deviations in the generated sound and light signals [9][10].

The overall ionization region was measured in the order of a few mm^3. The region exhibits a teardrop shape that is elongated in the propagation direction of the laser and becomes larger with increasing laser pulse energy. The acoustic signal was captured by a microphone (G.R.A.S 46BE [11] and power module 12AK [12]) with a broad frequency range 3 Hz-100 kHz. The microphone was placed at a distance of 1.2m from the focal region and at an angle of 90 degrees with respect to the axis of propagation of the laser pulse. It should be noted that the microphone has to be placed off the axis of propagation of the laser pulse, in order to avoid the remaining optical energy hitting the microphone membrane. This, however, does not affect the result of the acoustic measurement, since it is known that, for such small ionization volumes, the plasma acoustic source is almost omnidirectional (see also Chapter 5, subsection 5.2.3.1). Finally, the microphone was connected to a sound card (RME Fireface 802 [13]) with a bandwidth 5 Hz-

92 kHz. The digitized sound pulses were recorded with the Audacity software [14] at a sampling rate $f_s = 192\ \mathrm{kHz}$.

The light signal was captured with an ultrafast InGaAs photodiode (Alphalas UPD-40-UVIR-P [15]) which is best suited for measuring optical signals with a bandwidth from DC to 7.5GHz. The rise times of the photodiode vary from 30 to 500 ps and cover a broad light spectrum from 250 to 1700 nm. From Planck's law describing blackbody radiation, it can be derived that this photodiode can capture thermal radiation from matter with a temperature between ~1700 K and ~11600 K. The capability of the optical sensor to capture thermal radiation in a broad temperature range is critical in the presented method, as the accuracy of the physical model's estimations relies on the accuracy with which the thermal radiation is captured.

In order to enhance the optical signal, a 10mm light collecting quartz lens was placed between the breakdown spot and the photodiode, effectively increasing the stereoscopic angle over which the light was collected. It has to be noted that, under these experimental conditions, the free electron density in the laser-induced plasma is estimated in the order of $5 - 8 \times 10^{24}/\mathrm{m}^3$. Such an electron density corresponds to a plasma frequency of approximately $\omega_p \simeq 1.5 \times 10^{14}\ \mathrm{Hz}$, which is well below the maximum light frequency that can be detected in our experiments ($\omega_r = 1.1 \times 10^{15}\ \mathrm{Hz}$). As a result, the generated plasma is fully transparent for the optical radiation of interest, and thus, optical radiation generated in the core of the plasma volume reaches the photodiode without significant losses. Under this condition, it can be considered that the number of photons collected by the photodiode is proportional to the total number of photons emitted across the entire plasma volume. The optical signals were recorded with an oscilloscope at $1\ \mathrm{GHz}$ sampling frequency within a 50 μs time window. Although the high repeatability of the phenomenon did not dictate averaging over multiple pulses, both the acoustic and optical signals presented here were averaged over 25 pulses in order to reduce background noise.

4.1.2 Signal Processing

4.1.2.1 Acoustic signal analysis

In Chapter 2 it was shown that the LIB acoustic waves exhibit a broad frequency spectrum extending from the lower audible frequencies up to the ultrasounds. Due to the bandwidth limitations of the microphone and the analog-to-digital conversion system, whose combined cutoff frequency f_{cut} is approximately around 90 kHz, the signals could not be perfectly captured in the experiments. Nevertheless, the spectral peaks of the LIB acoustic pulses, which effectively denote the frequencies with the highest energy content, lie within the range between 20 kHz and 30 kHz, while a lower spectral peak appears between 60 kHz and 80 kHz. Since these frequencies are well below f_{cut}, it can be considered that the acoustic pulses are captured with sufficient accuracy for the purposes of this study. The frequency spectrum of the LIB acoustic pulses is calculated via Fast Fourier Transform (FFT) [16]. To preclude spectral folding from components beyond the system's cutoff frequency, a sampling frequency of 348 kHz was used for the recordings. The observation window for each pulse has a duration of 0.5 s corresponding to 192000 samples. The frequency resolution of the FFT vectors is 2 Hz and the maximum representable frequency is 192 kHz, however, it is practically limited to 90 kHz due to the abovementioned bandwidth limitations in the system's response.

4.1.2.2 Optical signal analysis

The emission of light following laser-induced breakdown is a complex process involving several distinct radiative phenomena that take place during ionization and consequent relaxation of the laser-matter interaction region. For the purposes of this work, the optical signal analysis and processing aim at the isolation and deduction of the thermal component from the total optical radiation, in order to use it as a heat source in the phenomenological model. The model correlates light and sound emission following LIB by proving that the LIB acoustic waves can be calculated from the thermal signal. Nevertheless, the proposed method also offers insight into the radiative phenomena, by revealing the time scales and the intensities of their manifestation and by extracting the time profile of the radiation generated by each different process. The signal analysis is based on previous understanding of the radiative phenomena in LIB, which can be attributed to free-free, free-bound and bound-bound processes and particularly: a) Bremsstrahlung, b) electron transitions, including radiative recombinations and de-excitations, and c) heating [1][9][7].

At times comparable to the laser pulse duration, the electron density in the interaction region is high due to photoionization. In this initial stage, plasma radiation is dominated by the Bremsstrahlung, namely, the radiative free-free transitions of electrons deflected by other charged particles, such as free or bound electrons and nuclei [1][9]. Immediately after the laser pulse excitation, the free electron density decreases rapidly due to electron loss processes [9][10]. The lifetime of free electrons in the air in the absence of excitation is in the order of several nanoseconds [1][6][9], and thus, Bremsstrahlung radiation is expected to fade within the first few hundred nanoseconds of the phenomenon. During this stage, light radiation produced from electron-ion recombinations (free-bound transitions) [9][6] and radiative electron de-excitations (bound-bound transitions) becomes dominant. Most importantly, these transitions lead to progressive energy transfer from the excited electrons to the heavy particles (ions, atoms, molecules) in the interaction volume, resulting to a local rapid increase in temperature. As time progresses, the free electron density is depleted and the plasma relaxes. At these later stages, radiation can be attributed solely to the increased heat in the interaction volume and to electron de-excitations. Light emission continues until the heavy particles in the excited medium cool down to ambient temperature [17][18]. A conceptual chain of processes behind laser-induced breakdown in air starting from laser energy deposition to the generation of the mechanical shock wave is shown in Fig. 4.2.

Following this analysis, the sources of light radiation in laser-induced breakdown and the respective optical signals captured by the photodiode can be categorized into 3 groups [1][9]:

1. Bremsstrahlung radiation $s_B(t)$, generated by deceleration of the free electrons in the dense plasma.

2. Radiation from electron transitions $s_{T,}(t)$, including radiative free-bound electron recombinations and bound-bound electron de-excitations.
3. Thermal radiation $s_H(t)$ due to the heating of the heavy particles in the interaction volume.

As described earlier, the rapid local heating of the air leads to thermoelastic expansion of the excited volume, which in turn leads to the formation of the LIB shock wave. In the model developed here, the thermoelastic expansion is attributed to a heat source whose time profile is estimated by the optical signal $s_H(t)$ relating to the flow of thermal energy in the interaction region. However, $s_H(t)$ is not directly accessible from the photodiode measurement and needs to be deduced from the total optical signal including also the $s_B(t)$ and $s_T(t)$ components. Fig. 4.3 shows a typical photodiode signal $s_{\mathrm{ph}}(t)$ generated by a 40mJ laser pulse energy, where the signal amplitude is in logarithmic scale. In the figure, distinct time regions can be seen that correspond to the different phases of the radiative processes following LIB. In each interval, the main sources of radiation are marked. Region (I) corresponds to the early times of the plasma lifetime where the optical signal is dominated by Bremsstrahlung radiation [19][20]. Radiation from electron transitions is also present at that time, however it is weak compared to $s_B(t)$. Region (II) marks a transitional time interval where multiple sources of radiation contribute to the total irradiance. Bremsstrahlung radiation is weakened due to the rapid decrease of the free electrons after the influence of the laser pulse [6][9] and thus, the measured signal can be mainly attributed to electron recombinations and de-excitations [1]. Note that, at these times the heavy particles in the ionized volume are still cold and there is no thermal radiation present in the optical signal. Progressively, the thermal radiation becomes significant as the heavy particles gain energy through interactions with the recombining electrons, while the electron density decays. At these later times, light radiation originates mainly from electron de-excitations and heat in the interaction volume. Finally, region (III) marks the last phase of the radiative phenomenon, where radiation from electron de-excitations fades. During this last time window, only thermal radiation remains until the air cools down to ambient temperature. For the present analysis, this interval is estimated to be around 10 to 15 µs.

The presented analysis is supported by the findings in other works [6][19]. From [6] it can be seen that, under similar experimental conditions, the spectral lines of the Nitrogen and Oxygen ions N^+ and O^+ fade completely within approximately 1 µs. This time scale coincides with the interval from the beginning of Region (II) up to the completion of the recombination process. Moreover, the times of the radiative electron transitions of the neutral Oxygen measured in [6] and [19] are in good agreement with the end

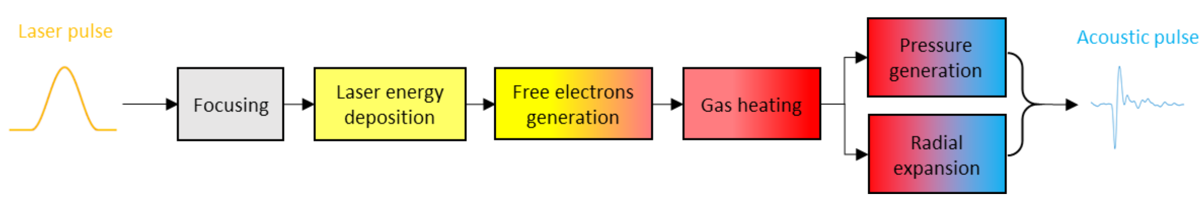

Fig. 4.2: Conceptual diagram of the physical processes behind laser-induced optoacoustic transduction

of region (II), which here signifies the decay of the electron de-excitation processes and the beginning of the purely thermal phase of the phenomenon. Note that, for comparison with [19], the much higher pulse energy used in that case must be taken into account. Finally, the time scales of the thermoelastic expansion of the interaction region measured in [6] are in perfect agreement with the time evolution of the thermal signal $s_H(t)$, further validating the proposed analysis.

Having analysed the physical aspects behind the photodiode measurement, here, the mathematical process for extracting the thermal signal $s_H(t)$ from the complete photodiode signal $s_{\mathrm{ph}}(t)$ is presented. The signal $s_{\mathrm{ph}}(t)$ can be expressed as the sum of the contributions from the different radiative processes:

$$s_{\mathrm{ph}}(t) = s_B(t) + s_T(t) + s_H(t) \tag{4.1}$$

According to Eq. (4.1), the thermal signal can be written as:

$$s_H(t) = s_{\mathrm{ph}}(t) - s_T(t) - s_B(t) \tag{4.2}$$

It becomes apparent that, in order to isolate $s_H(t)$, the transitions and Bremsstrahlung signals have to be removed from the total photodiode signal. For this purpose, estimates of the temporal profiles of $s_T(t)$ and $s_B(t)$ are required.

It is known that at the initial stages of the phenomenon the electrons gain their maximum energy and consequently exhibit the highest cross-section for deceleration and deflection by other electrons or the ions. In addition, the total Bremsstrahlung signal $s_B(t)$ is proportional to the free electron density $\rho_e(t)$ [1]. From [9][21] it can be deduced that the time evolution of the free electron density approximately follows the temporal profile of the laser pulse. Due to these characteristics, it is expected that the Bremsstrahlung signal is also a Gaussian function, a fact that is also supported by the numerical evaluations in [9].

Under these assumptions, and due to the symmetry of the Gaussian function around its peak, the complete profile of the Bremsstrahlung signal can be reconstructed by mirroring its first half as follows:

$$s_{B,r}(t) = s_{B,p}(t) + s_{B,p}(2\tau_{\mathrm{peak}} - t) \tag{4.3}$$

where $s_{B,r}(t)$ is the reconstructed Bremsstrahlung signal, τ_{peak} marks the time instance that the Bremsstrahlung signal reaches its peak value, and:

$$s_{B,p}(t) = \begin{cases} s_B(t), & 0 \leq t \leq \tau_{\mathrm{peak}} \\ 0, & \text{otherwise} \end{cases} \tag{4.4}$$

Fig. 4.4a) shows a detail of the measured photodiode signal at initial times of the plasma formation, on which the reconstructed signal of Eq. (4.3) is superimposed. In the next step, the signal $s_{B,r}(t)$ is subtracted from $s_{\mathrm{ph}}(t)$, resulting to the signal $s_{T+H}(t)$:

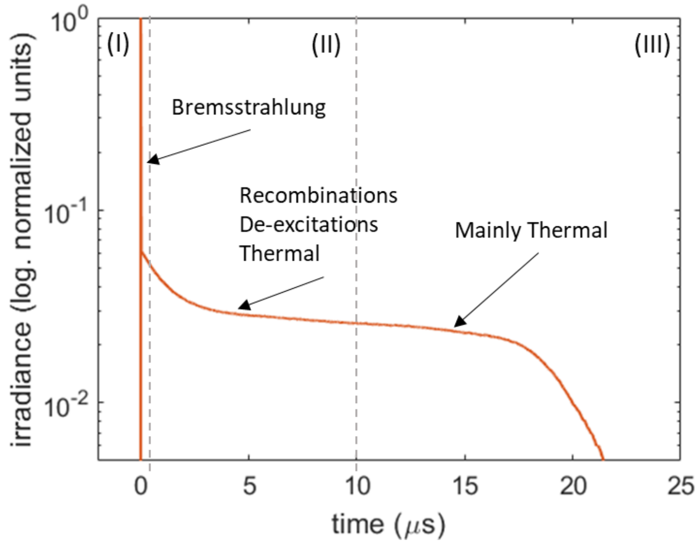

Fig. 4.3: Total captured signal of the light radiation $s_{ph}(t)$, where the three distinct regions can be distinguished: (I) Bremsstrahlung region, (II) mixed region where recombinations, de-excitations and the rising thermal radiation co-exist and (III) radiation from de-excitations fades out and mainly thermal radiation remains.

$$s_{T+H}(t) = s_{\text{ph}}(t) - s_{B,r}(t) \tag{4.5}$$

The signal $s_{T+H}(t)$ is shown in Fig. 4.4b) with red and contains only the transitions and heat components of the total radiation.

Furthermore, to approximate the electron transitions signal $s_T(t)$, the following assumptions can be made. With the arrival of the laser pulse and the initiation of breakdown, a large number of free electrons is produced. The free electrons exhibit a short lifetime in ambient air, in the order of several nanoseconds, and thus the recombination process starts approximately in the time scale of the laser pulse. This leads to a rapid increase in the irradiance from electron transitions $s_T(t)$, which is clearly distinguishable in the early times of the signal $s_{T+H}(t)$ (see Fig. 4.4b)). The transitions signal naturally decays after the influence of the pulse. However, bound-bound electron transitions from more excited to less excited electronic states also contribute to the transitions signal and for this reason, it lives on after the end of the recombinations process, extending up to a few microseconds.

The profile and time scales of the decay of $s_T(t)$ can be validated from existing spectrally resolved measurements of the plasma radiation. Harilal et al. [6] show that singly ionized Nitrogen atoms have a lifetime of several hundreds of nanoseconds, while neutral Oxygen atoms undergo radiative de-excitations for more than ten microseconds after the plasma generation. Moreover, from [6] it can be deduced that the temporal profile of the irradiance due to radiative transitions takes the form of an exponential decay. Based on these considerations, the transitions signal is modeled as:

$$s_{T,r}(t) = \begin{cases} c_1 \cdot \mathrm{e}^{-\frac{t-\tau_0}{\tau_1}}, & t \geq \tau_0 \\ 0, & \text{otherwise} \end{cases} \tag{4.6}$$

where c_1 is a scaling constant, τ_0 is the time when $s_{T,r}(t)$ takes its peak value and τ_1 is the characteristic time of the decay.

Similar considerations can be made for the thermal signal: with the initiation of the recombination process immediately after the plasma formation, energy is transferred from the free electrons to the ions and atoms, raising the thermal energy inside the ionization volume. The thermal energy builds up progressively, leading to radial expansion of the heated volume. Due to the expansion, pressure is built at the boundary with the ambient air, which is eventually equilibrated from the ambient gas pressure. At this time instance, the expansion stops and the generated pressure decouples from the excited volume and propagates in air as a shock wave. From [6] it is known that, for the range of laser pulse energies under discussion, the decoupling time is ~10 to 15 microseconds.

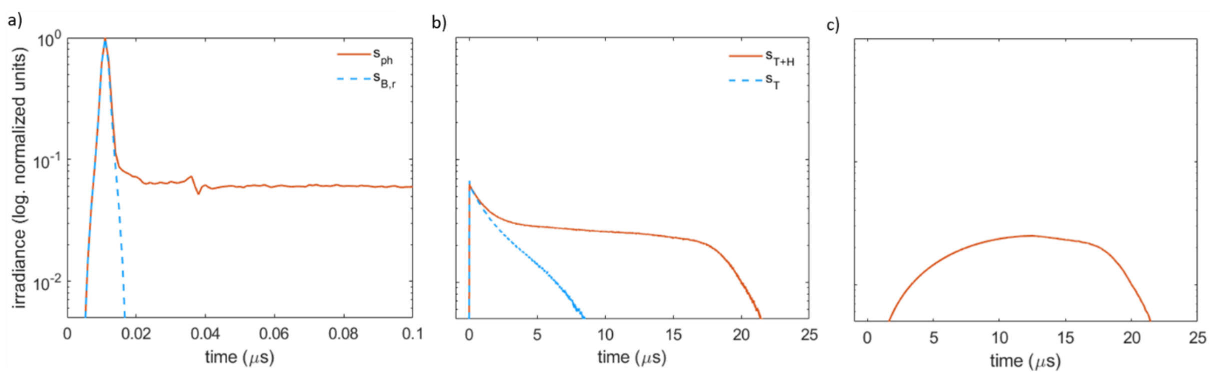

Fig. 4.4: a) Photodiode signal $s_{ph}(t)$ (red) and reconstructed Bremsstrahlung signal $s_{B,r}(t)$ (blue) at early times of the phenomenon, b) $s_{T+H}(t)$ signal (red) and estimated transitions signal $s_T(t)$ (blue) and c) reconstructed thermal signal $s_H(t)$.

It becomes evident that the thermal signal is weak at the initial times of the phenomenon and thus, the transitions signal is dominant in the optical radiation of the early times of region (II). For this reason, the early part of the exponential decay of $s_{T+H}(t)$ can be used to obtain $s_T(t)$. Based on the these considerations, the transitions signal was reconstructed by fitting the signal $s_{T+H}(t)$ of Eq. (4.5) with the exponential decay curve of Eq. (4.6). Finally, by subtraction of $s_{T,r}(t)$ from $s_{T+H}(t)$, the reconstructed thermal signal $s_{H,r}(t)$ is obtained:

$$s_{H,r}(t) = s_{T+H}(t) - s_{T,r}(t)$$

The signal $s_{H,r}(t)$ is shown in Fig. 4.4 c).

An overview of the complete chain of transformations of the measured photodiode signal leading to the derivation of the spectrum of the LIB acoustic signal is presented in Fig. 4.5. In the last step, low-pass filtering of the acoustic spectrum is carried out. This is necessary in order to precisely match the model's predictions with the experimental results for the following reasons: the acoustic wave eventually captured by the microphone undergoes acoustic absorption during its propagation in the ambient air. Air absorption exhibits a low-pass profile [22][23], since it is stronger in the higher frequencies while it practically leaves the lower frequencies unaffected. By contrast, the light emitted from the interaction region does not undergo similar low pass filtering during its propagation in the plasma or in the air. Moreover, the low-pass profile of the acoustic measurement system has also to be taken into account, since it is not apparent in the photodiode signal and thus, is not otherwise accounted for in the phenomenological model. The filter was fine-tuned so that the match between the model's predictions and the measurements is optimized.

For the analysis of the digitized photodiode signals, an expanded window was used, corresponding to 1ms (10^6 samples) and the resulting frequency resolution of the optical signals is 1 kHz. To reduce the noise in the measurement, the optical signals were averaged over 25 measurements.

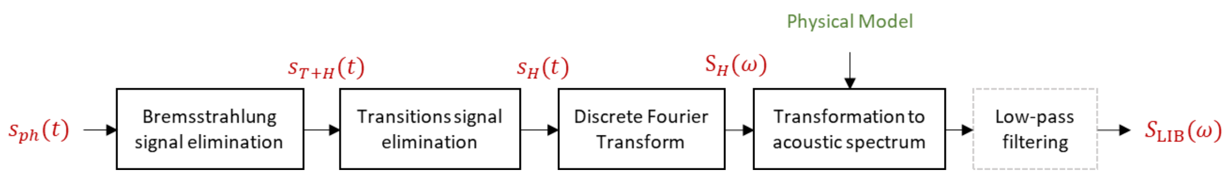

Fig. 4.5: Flow diagram of the processing steps of the measured optical signal.

4.2 Physical model

Here, the physical model demonstrating the correlation between light and sound following laser-induced breakdown is developed. The model is based on the linear wave equation with a heat source [24][25][24], and allows for the derivation of the spectra of LIB acoustic pulses from the thermal signal $s_H(t)$. The benefit of such a simple model is that the complex processes behind laser-matter interaction, i.e. energy deposition, plasma generation and relaxation etc., are not modelled in detailed in a microscopic level. Due to the multitude and complexity of the involved phenomena described in Chapter 2, this task would be extremely challenging. For this reason, here, these phenomena are represented by the macroscopic quantity of the heat source. Most importantly though, it directly demonstrates the relation between the LIB secondary phenomena of light and sound radiation, as it predicts the acoustic signals from the optical measurements.

Suppose a sphere S with radius R centered at the origin of a spherical coordinates system and surrounded by an infinite reservoir. The sphere represents the air volume where the laser energy is deposited while the infinite reservoir represents the atmospheric air. The consideration of a spherical interaction volume is valid for plasma sources generated by nanosecond lasers under strong focusing. In reality, the plasma volume exhibits an elongated geometry and an axial temperature distribution described in detail in

[5][26][27]. However, due to the small length-to-radius ratio of the plasma volume, the acoustic radiation is identical to that of a spherical source, especially at an angle of 90^o degrees with respect to the axis of the laser pulse propagation where the measurements were taken (see also [28]).

Furthermore, the increase in thermal energy inside the sphere results to a supersonic expansion of the interaction volume and to the generation of acoustic pressure at the boundary with the ambient air. Eventually, the shock wave decouples from the plasma and propagates away from the source, progressively transforming into a sound wave. In the linear wave equation approach, the initial non-linear propagation of the shock wave is neglected; however, as it is demonstrated also in the Results section, the accuracy of the proposed analysis is not compromised by this simplification. In the early stages of the acoustic phenomenon, the temporal profile of the shock wave is approximately that of an ideal N-wave, also manifesting in sonic booms or "blast waves" [29][30]. In Chapter 2 it was argued that the N-wave is an appropriate model for the LIB shock wave, as it describes the pressure discontinuity points in the shock front and tail. With the propagation of the N-wave away from the plasma, its velocity and pressure progressively decrease and its temporal profile becomes smoother around the edges. The smoothing is further enhanced by the characteristic absorption of the air, which is strong in the very high frequencies while it is negligible in the lower end of the spectrum. As a consequence, disregarding the physical aspects of propagation velocity and medium discontinuity, the shock-to-sound transformation can be seen as a suppression of the acoustic energy in the high frequencies, in proportion to the effect of a low-pass filter. However, the focus of the present analysis and experimental measurements is limited to the audible and near ultrasound frequency spectrum, which can be argued that remains unaffected by this low-pass filtering effect. Hence, the non-linearity of the acoustic phenomenon in the initial stages of the shock formation and propagation does not influence the accuracy of the presented results.

The pressure $p(r,t)$ at a distance r and time t generated due to the heat source $H(r,t)$ takes the form [24]:

$$\left(\nabla^2 - \frac{1}{c^2}\frac{\partial^2}{\partial t^2}\right) \cdot p(r,t) = -\frac{\gamma - 1}{c^2} \cdot \frac{\partial}{\partial t} H(r,t) \tag{4.7}$$

where c is the speed of sound, $\gamma = \frac{c_p}{c_v}$, where c_P, c_V the specific heat capacity of the air under constant pressure and constant volume and $H(r,t)$ is the rate of heat evolution per unit volume. Equation (4.7) is mainly used for calculations of the pressure generated due to the photoacoustic phenomenon, in which, the source term can be directly associated to the energy deposited by the laser pulse to the interaction medium. In this case, the source term maintains the temporal and spatial characteristics of the laser pulse [24]. Conversely, since sound generation following laser-induced breakdown of gases is a secondary phenomenon, the energy deposited by the laser cannot be directly used as the heat source. The signal processing methodology described in the previous subsection provides the necessary transformations to derive an appropriate source term for this particular model.

Furthermore, by taking the Fourier transform of Eq. (4.7), we get [24]:

$$\left(\nabla^2 - \frac{\omega^2}{c^2}\right) \cdot p(r,t) = i\omega \frac{(\gamma - 1)}{c^2} H(r,t) \tag{4.8}$$

The Green's function solution of Eq. (4.8) in the far field is [24]:

$$p(r,\omega) = \pi\omega \frac{(\gamma - 1)}{c^2} \cdot H_0^{(1)}(kr) \cdot \int_0^R J_0(k\rho)\, H(\rho,\omega)\rho d\rho \tag{4.9}$$

where $H_0^{(1)}(kr)$, $J_0(k\rho)$ are the zero-order Hankel and Bessel functions respectively, k is the wave number, r is the distance from source and ω is the angular frequency.

It is known that the thermal radiation exchanged between the sphere and the bath can be expressed as the radiation $P_{\mathrm{in}}(t)$ reaching the sphere from the outside and the radiation $P_{\mathrm{out}}(t)$ emitted from the sphere to the surrounding environment:

$$s_H(t) = P_{\mathrm{out}}(t) - P_{\mathrm{in}}(t) \tag{4.10}$$

According to the Stefan-Boltzmann law, the radiant intensity of the thermal radiation is proportional to the fourth power of the temperature:

$$P_{\mathrm{in}}(t) = \sigma A T_{\mathrm{air}}^4, \quad P_{\mathrm{out}}(t) = \sigma A T_S^4(t) \tag{4.11}$$

where σ the Boltzmann constant, A is the surface of the heated volume, T_S is the temperature of the sphere and T_{air} is the room temperature. At this point, the following assumptions are made:

a) the radiating volume has an emissivity equal to one, or similarly, it behaves as a black body. This assumption does not compromise the accuracy of the model, since the emissivity and the other constant factors contributing to the scaling of the generated pressure are not of interest here; the analysis aims at the derivation of the normalized frequency spectra of the acoustic pulses and not the absolute acoustic pressure.
b) the volume of the plasma in the time window of the thermal radiation does not change significantly, which is in accordance with the findings in [14].

Moreover, by definition, the temperature T_{air} of the reservoir remains constant during the phenomenon, while T_S is a function of time. Substituting P_{in} and P_{out} of Eq. (4.11) into Eq. (4.10), the rate of heat transfer becomes:

$$s_H(t) = \sigma A \left(T_S^4(t) - T_{\mathrm{air}}^4\right) \tag{4.12}$$

However, the thermal radiation of the air at room temperature ($T_{\mathrm{air}} = 300K$) is beyond the wavelength range of the measuring photodiode and, hence, it is not present in the photodiode signal $s_{\mathrm{ph}}(t)$.

Moreover, as mentioned in subsection 4.1.1, the plasma volume is transparent for the wavelengths visible by the photodiode and thus, the thermal signal $s_H(t)$ is proportional to the radiation emitted by the whole volume. Due to these facts, the signal $s_H(t)$ can be considered to be proportional to $T_S^4(t)$ and can be expressed by:

$$s_H(t) = \sigma A T_S^4(t) \tag{4.13}$$

In order to obtain the heat source $H(t)$ for the wave equation model, the time evolution of the internal energy in the interaction volume needs to be obtained from Eq. (4.13). It is known that the energy deposited by the laser in the volume is proportional to the change of its internal energy. In turn, and by treating the air as an ideal gas, the change in the internal energy can be considered proportional to the change in temperature:

$$H(t) \sim \Delta T = T_S(t) - T_{\mathrm{air}} \tag{4.14}$$

The temperature $T_S(t)$ of the volume can be found from Eq. (4.13), as:

$$T_S(t) = \sqrt[4]{\frac{s_H(t)}{\sigma A}} \tag{4.15}$$

and thus:

$$H(t) \sim \sqrt[4]{\frac{s_H(t)}{\sigma A}} - T_{\mathrm{air}} \tag{4.16}$$

Taking the Fourier transform of Eq. (4.16) and by disregarding the constant term T_{air} (DC term), we get the frequency domain heat source:

$$H_S(\omega) = \int_{-\infty}^{\infty} H(t) \cdot e^{-i\pi\omega t} = \frac{1}{b} T_S(\omega) \tag{4.17}$$

where b is a scaling constant. Now, the spatial distribution of the heating function in the radial dimension can be approached by the radial distribution of the intensity of the laser pulse. In this case, the radial heat distribution follows a Gaussian shape:

$$H_S(r, \omega) = e^{i\omega c(r)} \cdot e^{-\frac{r^2}{2R^2}} \cdot T_S(\omega) \tag{4.18}$$

where $c(r)$ is a function of the radial distance from the center of the volume. From the numerical simulations it becomes evident that, due to the very small dimensions of the source compared to the distance of evaluation, the radial distribution of the heat does not significantly affect the calculations. As a result, a homogeneous heat distribution within the volume can also be used, in which case the frequency-domain heat source $H(\rho, \omega)$ in the integral of Eq. (4.9) reduces to $H(\omega)$. However, for reasons of completeness, the Gaussian approach was used here. Furthermore, in reality, different pulse energies lead to different interaction volumes; particularly, as expected, stronger pulses lead to larger volumes. However, it was found that the exact size of the interaction volume does not significantly affect the simulation results, especially for the calculation of normalized acoustic spectra. For this reason, a radius $R = 1\ \mathrm{mm}$ was used for all the simulations, which corresponds to an average radius of the generated plasma volumes, as measured by the authors in preliminary experiments.

By substituting the heat term obtained by Eq. (4.17) and (4.18) into Eq. (4.9) and by neglecting any constant scaling factors, we get:

$$p(r,\omega) = \omega \cdot H_0^{(1)}(kr) \cdot T_S(\omega) \cdot \int_0^R J_0(k\rho) \cdot e^{i\omega c(\rho)} \cdot e^{-\frac{\rho^2}{2R^2}} \cdot \rho d\rho \qquad (4.19)$$

Equation (4.19) gives the normalized frequency spectrum of the LIB acoustic wave after propagating for a distance r away from the plasma and was solved numerically in MATLAB [16] by conversion of the integral into a sum using the rectangular integration method. The radius R of the interaction volume was discretized with 100 equal elementary intervals, although, the results were found to be insensitive to the discretization resolution. Moreover, for the light signals described in the previous subsection, a frequency resolution of 1kHz was used, with a maximum representable (Nyquist) frequency of 500 MHz.

4.3 Results

This section presents results from the experimental measurements and the simulations of the secondary radiative phenomena following laser-induced breakdown. In Section 4.3.1, the measured optical and acoustic signals $s_{\mathrm{ph}}(t)$ and $s_{\mathrm{LIB}}(t)$ are presented and compared for laser pulses of different energies. In Section 4.3.2, the frequency spectra $S_{\mathrm{LIB}}(\omega)$ of the LIB acoustic pulses are evaluated via the phenomenological model (Eq. (4.19)) and compared to the acoustic spectra derived from the acoustic measurements.

4.3.1 The effect of the laser pulse energy

As described in the previous sections, the thermoelastic expansion and consequent pressure generation in laser-induced breakdown is caused by the kinetic energy gained from the ions, atoms and molecules via the interactions with the free electrons of the plasma. The amount of deposited energy depends, among others, on the energy of the laser pulse, with the relation being highly complex and non-linear. Nevertheless, it is known that for nanosecond pulses with intensities well above the ionization threshold, an increase in the laser pulse energy leads to an increase in the absorption efficiency, until a maximum efficiency is reached. In any case, for laser pulses of the same duration and wavelength but different energies, the stronger pulse leads to more energy deposited in the interaction volume (see for example [9][10][30]). For the energy range of interest in this work, the generated free electron density in the volume is higher, while at the same time the ionization volume is larger. This can be explained by considering a minimum intensity threshold for the ionization to initiate; for the stronger pulse, the optical intensity is above the threshold in a wider length across the axial and the radial directions, leading to a larger ionization volume. As a result, the volume of the interaction region increases with increasing laser pulse energy, while it also reaches higher temperatures, due to the higher free electron density that transfers energy to the heavy particles of the gas. These combined effects lead the excited volume to a broader thermoelastic expansion; most importantly though, the broader expansion dimensions translate to longer durations of both the expansion and collapse phases. The increase in the duration of the thermoelastic phenomenon is of particular interest, as it affects the duration of the secondary phenomena of light and sound emission. This fact is reflected in the duration of the thermal radiation and the duration of the acoustic pulse, especially in the part of the negative pressure corresponding to the elastic collapse of the medium.

The aspects described above can be seen in Fig. 4.6 where the measured acoustic signals $s_{\mathrm{LIB}}(t)$ and photodiode signals $s_{\mathrm{ph}}(t)$ are presented for laser pulse energies of 40, 60, 80 and 100 mJ. It becomes apparent that the sound and light emission exhibit longer duration with increasing laser pulse energy. Also, from comparison of Fig. 4.6 a) and Fig. 4.6 b) it can be seen that both radiative phenomena have a duration in the order of several microseconds. It can be observed that the sound pulses have approximately double the duration of the respective photodiode signals. This can be understood by considering that the thermal radiation is emitted only during the expansion phase, which corresponds to the positive part of the acoustic pulses. The negative part of the pulse is generated by the reaction of the elastic medium to the expansion and takes place after the interaction volume has cooled down to temperatures close to T_{air}. For this reason, it is expected that the optical radiation will approximately coincide in time with the positive acoustic pressure, which is validated by the graphs of Fig. 4.6. Finally, the time scales of the thermoelastic phenomenon have a direct impact on the frequency spectra of the generated acoustic pulses. In the next subsection it is shown that, an increase in the laser pulse energy

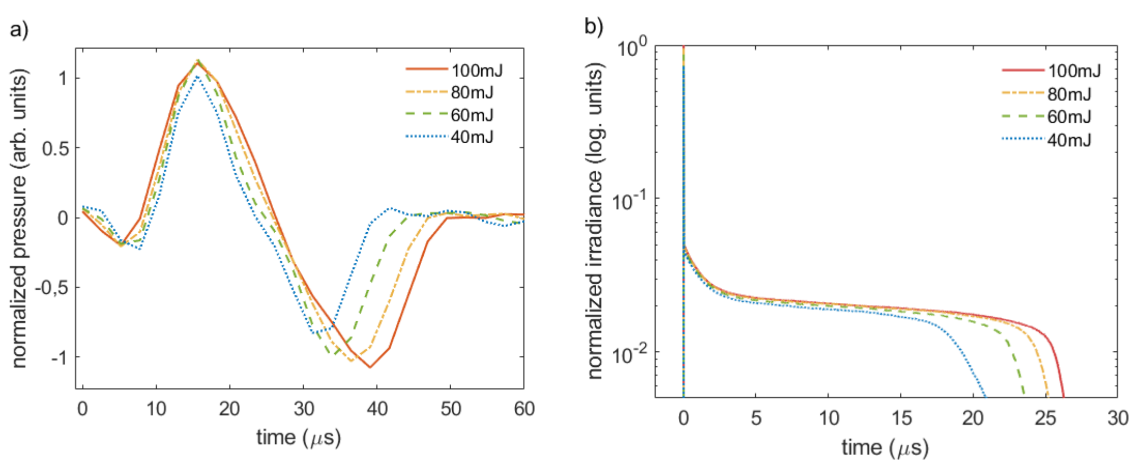

Fig. 4.6: The correlation in the duration of a) the acoustic signals $s_{\mathrm{LIB}}(t)$ and b) photodiode signals $s_{\mathrm{ph}}(t)$ and their dependence on the laser pulse energy. Note the difference in the time scales of the figures.

leads to a shifting of the acoustic frequency spectrum towards the lower frequencies. This is an immediate consequence of the increase in the duration of the thermoelastic phenomenon.

4.3.2 Frequency spectra of LIB sound waves

As described in the previous section, from the measured optical signals $s_{\mathrm{ph}}(t)$, the thermal radiation component $s_H(t)$ relating to the kinetic energy of the heavy particles in the interaction volume is deduced (Eq. (3)). The signal $s_H(t)$ is transformed using the discrete Fourier transform and produces the frequency-domain signal $S(\omega)$. The signal $S(\omega)$ is introduced into Eq. (4.19), from which the frequency spectrum $S_{\mathrm{LIB}}(\omega)$ of the acoustic pulse is calculated. The respective frequency spectrum is also calculated from the measured acoustic signal $s_{\mathrm{LIB}}(t)$ via Eq. (4.19). The comparative results of the analytically and experimentally evaluated frequency spectra for laser pulse energies of 40, 60, 80 and 100 mJ are presented in Fig. 4.7. It becomes evident that the model reproduces the shape of the LIB acoustic spectra [30][31] with high accuracy. Small deviations between the measurements and the model can be attributed to the limited optical bandwidth of the photodiode, due to which, a part of the thermal signal is not captured in the experiment. It should be noted that, preliminary spectrally resolved measurements of the thermal radiation generated with the laser energies under consideration, showed emission peaks at wavelengths significantly lower than 1000 nm. This is expected since, according to [32], the plasma can momentarily reach temperatures of 20000 K or higher. Additionally, as discussed in the previous section,

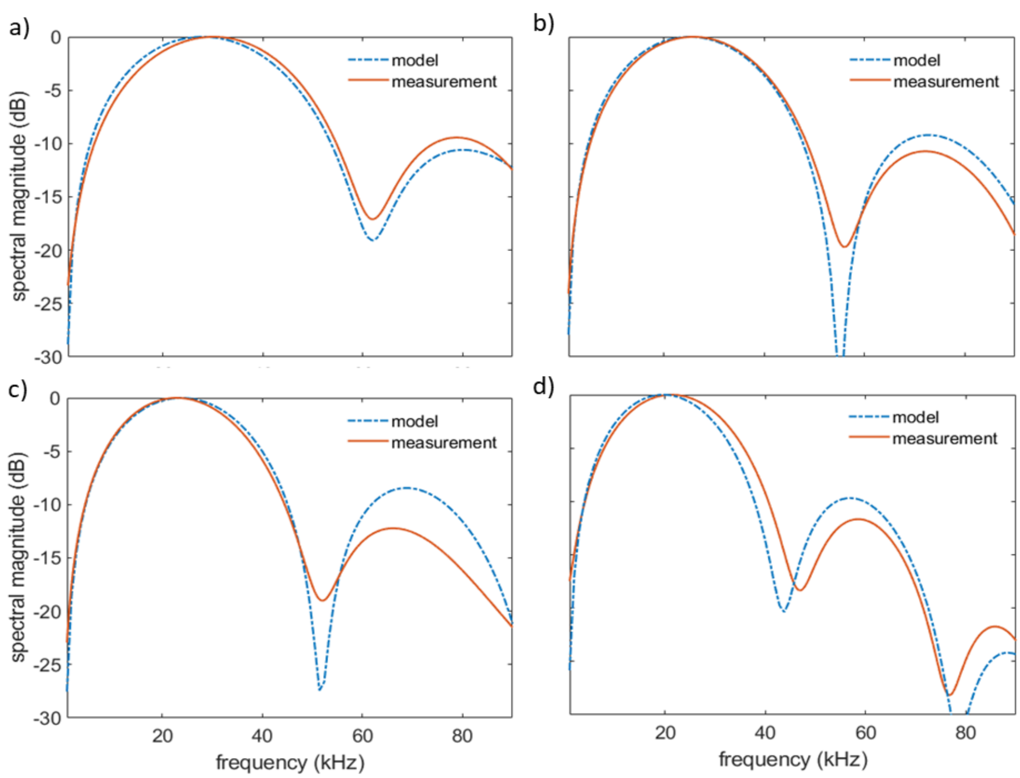

Fig. 4.7: Comparative acoustic spectra $S_{\mathrm{LIB}}(\omega)$ of the LIB sound pulses for a) 40mJ, b) 60mJ c) 80mJ and d) 100mJ laser pulses, as obtained from the proposed model and the acoustic measurements.

there is also a small contribution of narrow spectral lines superimposed on the continuum of the thermal radiation, which might affect the precision of the method, especially for higher laser pulse energies. Finally, the non-linearities of the phenomenon, which are not accounted for in the model, might also contribute to the small deviations, especially in the higher end of the frequency spectrum. Nevertheless, the comparative results demonstrate clearly that the main characteristics of the LIB acoustic spectra, namely, the overall shape and the position of the spectral peaks and dips withing the observed bandwidth are reproduced with satisfactory accuracy for the used laser pulse energies. Interestingly, by comparison of the graphs a)-d) of Fig. 4.7 it can be argued that the model's accuracy is higher for the weaker pulses. This fact highlights the role of the photodiode's bandwidth in the capturing of the thermal signal: an increasing pulse energy leads to higher temperatures in the interaction volume, causing a shift of the Blackbody radiation towards shorter wavelengths. With the lower limit of the photodiode being 250 nm, as the laser pulse energy increases, an increasing part of the thermal radiation is not captured, resulting to inaccuracies in the calculation of the generated acoustic spectrum.

From Fig. 4.7 it becomes evident that the acoustic spectrum is shifted towards the lower frequencies as the optical energy increases. For example, the spectral peak as well as the first spectral dip of the N-pulse generated by the 40 mJ laser pulse appear at 30 kHz and 60 kHz respectively, while for the 80 mJ laser pulse, the spectral peak is at 23 kHz and the spectral dip at 52 kHz. This shift is clearly shown in Fig. 4.8, where the frequencies of the spectral peaks and dips of the LIB acoustic pulses are plotted versus the energy of the generating laser pulses. As described in subsection 4.3.1, the spectral shift can be attributed to the increasing duration of the thermoelastic process leading to the acoustic emission with increasing laser pulse energy.

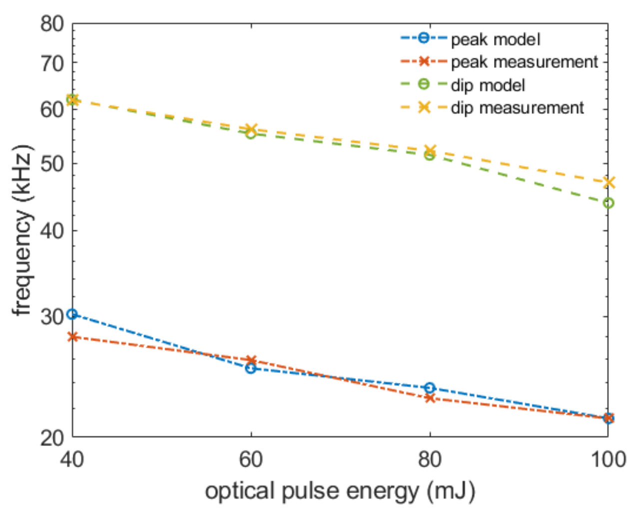

Fig. 4.8: Experimentally and analytically evaluated frequencies of the spectral peak and the first spectral dip of the LIB acoustic waves in terms of the laser pulse energy.

Conclusions

In this Chapter, a joint study of the light and sound radiation following laser-induced breakdown in ambient air is presented, demonstrating correlation between the two radiative phenomena. Simultaneous measurements of the light and sound signals were carried out using large observation windows in order to capture the complete evolution of the radiative processes from the early times of the plasma formation until the termination of the phenomenon. The measurements, and especially the correspondence in the time scales of the light and sound signals, provided evidence of the relation between the light and the sound radiation in laser-induced breakdown. To prove this aspect, a phenomenological model was developed that allows for the estimation of the frequency spectra of the acoustic signal from the measured optical signal. For this purpose, the signal component corresponding to the thermal radiation was isolated from the total optical signal, by identifying the different light radiative processes. This physics-driven signal analysis process clearly revealed the mechanisms behind the emission of light and sound during laser-induced breakdown and allowed for the isolation and reconstruction of the distinct optical components. The derived thermal signal was used as a heat term in a linear wave equation. The equation was solved computationally in the frequency domain, giving the frequency spectra of the generated sound waves. The model's predictions were compared to the experimentally evaluated acoustic spectra showing good agreement, and effectively proving the correlation between light and sound radiation following LIB.

Moreover, the impact of the laser pulse energy on the time scales of the radiative phenomena was studied through the experimental measurements and the simulation results. The study demonstrated that a stronger laser pulse leads to a stronger, and, importantly, longer in duration, thermal phenomenon. This was found to have a direct impact on the spectra of the generated acoustic pulses; a spectral shift towards the lower frequencies was observed with increasing laser pulse energy which can be associated to the duration of the optical radiative processes and the total heat transferred from the laser to the interaction volume. This association will be further studied in the near future, by developing a physical model of the laser pulse absorption and energy deposition, with detailed and quantitative description of the involved physical processes. Finally, another goal is to further study the Bremsstrahlung signal and investigate its relationship to the amplitude of the generated acoustic pressure.

References

[1] Zel'dovič, J. & Rajzer, J. *Physics of shock waves and high-temperature hydrodynamic phenomena*. Acad. Pr. (1970).

[2] Biagioni, A. et al. Electron density measurement in gas discharge plasmas by optical and acoustic methods. Journal of Instrumentation, 11(08) (2016).

[3] Point, G. Energy deposition in air from femtosecond laser filamentation for the control of high voltage spark discharges, PhD thesis, Laboratoire d'Optique Appliquée, Ecole Polytechnique, Palaiseau, France (2015).

[4] Quantel - Laser manufacturer. (n.d.). Retrieved May 14, 2021, from https://www.quantel-laser.com/home.html

[5] Harilal, S. & Harilal, B., Diagnostics of Laser Induced Spark in Air Using Fast ICCD Photography, Internal Lab Report, Laser Plasma and Laser Matter Interactions Laboratory, University of California, San Diego (2002).

[6] Harilal, S., Brumfield, B. & Phillips, M. Lifecycle of laser-produced air sparks. Physics of Plasmas 22, 063301 (2015).

[7] Kaleris, K., Orphanos, Y., Bakarezos, M., Dimitriou, V., M., Tatrakis, M., Mourjopoulos, J. & Papadogiannis, N. On the correlation of light and sound radiation following laser-induced breakdown in air, Journal of Physics D: Applied Physics (2020).

[8] Nelson, P., Veyrie, P., Berry, M. & Durand, Y. Experimental and theoretical studies of air breakdown by intense pulse of light. Physics Letters 13, 226-228 (1964).

[9] Hamam, K., Gaabour, L. & Gamal, Y. Numerical modeling for investigating the optical breakdown threshold of laser-induced air plasmas at different laser characteristics. Physics of Plasmas 24, 073515 (2017).

[10] Kaleris, K., Delibašić, H. Petrović & Papadogiannis, N., Analytical and numerical analysis of the plasma evolution in air generated by nanosecond laser pulses, under review (2021)

[11] Gras 46be 1/4" ccp free-field standard microphone set. (n.d.). Retrieved May 14, 2021, from https://www.grasacoustics.com/products/product/143-46be.html

[12] GRAS 12AK 1-Channel power module With Gain, filters AND SYSCHECK GENERATOR. (n.d.). Retrieved May 14, 2021, from https://www.grasacoustics.com/products/power-module/traditional-power-supply-lemo/product/225-12ak

[13] Fireface 802. RME Audio Interfaces | Format Converters | Preamps | Network Audio & MADI Solutions. (n.d.). https://www.rme-audio.de/fireface-802.html

[14] Audacity Team. Web site: https://audacityteam.org/. The name Audacity® is a registered trademark of Dominic Mazzoni.

[15] Ultrafast photodetectors: UPD SERIES. (n.d.). Retrieved May 14, 2021, from https://www.alphalas.com/products/laser-diagnostic-tools/ultrafast-photodetectors-upd-series.html

[16] MATLAB. 9.7.0.1190202 (R2019b). Natick, Massachusetts: The MathWorks Inc. (2019).

[17] Papeer, J., Botton, M., Gordon, D., Sprangle, P., Zigler, A., & Henis, Z. Extended lifetime of high density plasma filament generated by a dual femtosecond–nanosecond laser pulse in air. New Journal of Physics 16, 123046 (2014).

[18] Shneider, M., Zheltikov, A. & Miles, R. Tailoring the air plasma with a double laser pulse. Physics of Plasmas 18, 063509 (2011).

[19] Wang, X., Song, X., Gao, X. & Lin, J. The effect of air pressure on the IR spectral emission from laser induced air plasma. Optics Communications 456, 124603 (2020).

[20] El-Rabii, H., Victorov, S. B., & Yalin, A. P. Properties of an air plasma generated by ultraviolet nanosecond laser pulses. Journal of Physics D: Applied Physics, 42(7), 075203 (2009).

[21] Noack, J. & Vogel, A. Laser-induced plasma formation in water at nanosecond to femtosecond time scales: calculation of thresholds, absorption coefficients, and energy density. IEEE Journal of Quantum Electronics 35, 1156-1167 (1999).

[22] Kay, G.W.C., Laby, T.H. Tables of Physical and Chemical Constants, section 2.4.1, online at NPL, http://bit.ly/1rkaKGv

[23] Stuart, J. R., Craven, P. A Hierarchical Approach to Archiving and Distribution, 137th AES Convention, (2014).

[24] Diebold, G. J. "Application of the Photoacoustic Effect to Studies of Gas Phase Chemical Kinetics", *Topics in Current Physics Vol.46: Photoacoustic, Photothermal and Photochemical Processes in Gases*, edited by Peter Hess, Springer, (1989).

[25] Couairon, A. & Mysyrowicz, A. Femtosecond filamentation in transparent media, Physics Reports, Volume 441, Issues 2–4, Pages 47-189, (2007).

[26] Ghosh, S. and Mahesh, K. Direct Numerical Simulation of the Thermal Effects in Plasma/Turbulence Interaction 45th AIAA Aerospace Sciences Meeting and Exhibit (2007)

[27] Ghosh, S. and Mahesh, K. Numerical simulation of laser-induced breakdown in air, 46th AIAA Aerospace Sciences Meeting and Exhibit (2008).

[28] Kaleris, K., Orfanos, Y., Bakarezos, M., Papadogiannis, N. & Mourjopoulos, J. Experimental and analytical evaluation of the acoustic radiation of femtosecond laser plasma filament sound sources in air. The Journal of the Acoustical Society of America 146, EL212-EL218 (2019).

[29] Naugol'nykh, K. A., & Ostrovskiĭ, L. A. Nonlinear wave processes in acoustics. Cambridge: Cambridge University Press (1998).

[30] Oksanen, M. & Hietanen, J. Photoacoustic breakdown sound source in air. Ultrasonics 32, 327-331 (1994).

[31] Eskelinen, J., Hæggström, E., Delikaris-Manias, S., Bolaños, J. & Pulkki, V. Beamforming with a volumetric array of massless laser spark sources—Application in reflection tracking J. Acoust. Soc. Am. 137 389–95 (2015).

[32] Aguilera, J. A., & Aragón, C. Characterization of laser-induced plasma during its expansion in air by optical emission spectroscopy: Observation of strong explosion self-similar behavior. Spectrochimica Acta Part B: Atomic Spectroscopy, 97, 86–93 (2014).

Chapter 5

The acoustic radiation of femtosecond laser plasma filaments in air

Contents

Introduction

In Chapter 1, the possibility to create directional sound sources via multiple laser-driven acoustic point sources in 3-dimensional (volumetric) arrangements was presented [1][2][3]. This Chapter studies the sound radiation of laser plasma filaments with respect to its directional characteristics. Laser plasma filaments are elongated plasma threads generated by the non-linear propagation of ultrashort laser pulses, sufficiently strong to evoke self-focusing effects in the air [4][5][6]. Due to the cylinder-like geometry of the plasma volume, laser filaments emit cylindrical waves that are inherently directional and depend on the particular geometrical characteristics of the plasma thread. This relation of the filament acoustic radiation to the plasma thread is systematically studied here via a parallel experimental and theoretical method, mainly focusing on the audible and near ultrasounds frequency range that are of interest for audio and acoustics applications. Particularly, a new phenomenological model is presented where the filament is modeled as an acoustic line source [7][8] consisting of infinitesimally small (elementary) omnidirectional sources. The elementary sources emit acoustic N-waves in a coherent manner while the pressure amplitude of each source is weighted according to its position on the line, to account for the differences in the amount of the deposited energy along the filament's axis. In accordance with the findings of Chapter 4, the weighting is estimated from the axial distribution of the filament's light radiation intensity. The phenomenological model allows for the evaluation of the acoustic radiation of laser filaments in terms of:

a. the length of the plasma thread
b. the distribution of the deposited energy along its axis
c. the pressure profile of the elementary source excitation

The model is validated by comparison with systematic acoustic measurements of the sound generated by filaments at different angles with respect to their axes, showing good agreement. Furthermore, the model is used to evaluate the impact of the filament's characteristics, particularly the length of the plasma thread and the axial distribution of the deposited energy, on the emitted sound. Finally, a complete computational model based on the wave equation with a heat source is proposed for the evaluation of the acoustic radiation of plasma filaments and preliminary results from a scaled filament model are presented.

Again, the experiments and the development of the model were carried out in collaboration with the Institute of Plasma Physics and Lasers (IPPL) of the Hellenic Mediterranean University (HMU).

5.1 Acoustic model of laser plasma filaments

5.1.1 Laser filaments as acoustic line sources

Suppose an acoustic line source with length L residing on the x axis of the XY plane and centered at the origin. The source consists of infinitesimally small acoustic sources arranged one next to the other. The total acoustic pressure $p(r, \phi, t)$ produced by the line source at time t at any point (r, ϕ) of the polar plane, where r, φ the radius and angle of the polar coordinates respectively, is given by [8]:

$$p(r, \phi, t) = \int_{-L/2}^{L/2} \frac{H_x(x)}{r'(x)} \cdot n\left(t - \frac{r'(x)}{c}\right) dx \tag{5.1}$$

The function $n(t)$ gives the pressure excitation of the elementary sources, $H_x(x)$ is the pressure scaling, or distribution function along the axis of the source and $r'(x)$ is the distance of an elementary point source located at point x from the point (r, φ), given by:

$$r'(x) = r \cdot \sqrt{\left(\cos\phi - \frac{x}{r}\right)^2 + (\sin\phi)^2} \tag{5.2}$$

A schematic representation of the acoustic line source model is shown in Fig. 5.1. As the geometry of plasma filaments can be approximated by a line, since the radius of filaments is typically more than one order of magnitude smaller than the length, the use of the acoustic line source model is proposed here to describe their acoustic emission. To accurately model the acoustic radiation of a plasma filament as a line source, the characteristic functions $n(t)$ and $H_x(x)$ have to be determined by examination of the physical aspects of laser-induced breakdown and consequent sound generation.

It should be noted that, any physical interactions between the elementary acoustic sources as well as potential sound diffraction around the edges of the filament can be neglected [9]. Since sound generation via LIB is a purely thermo-elastic effect, the plasma acoustic source is practically massless and, as a result, filament acoustic sources can be very well approximated as having no boundary to the surrounding air.

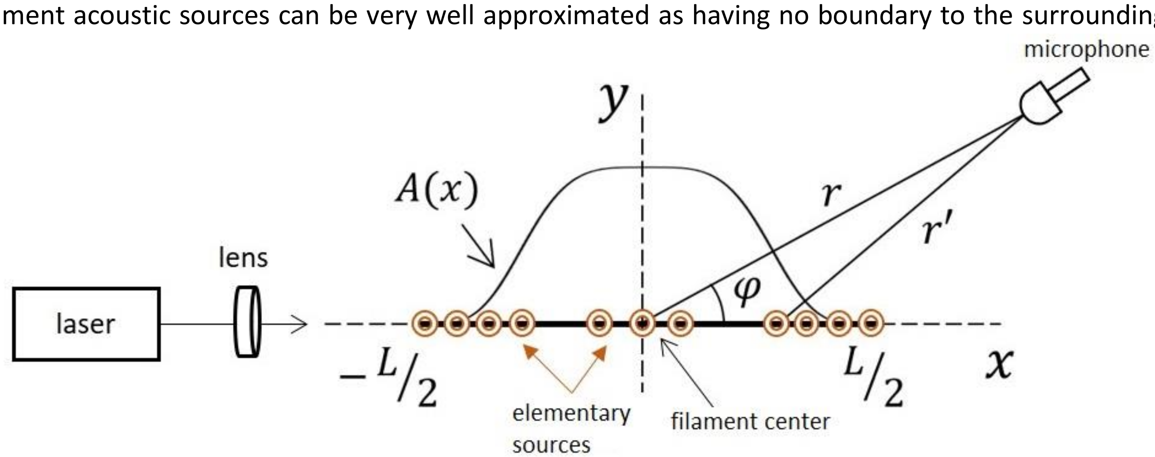

Fig. 5.1: Plasma filament acoustic source model and experimental setup.

Moreover, the assumption of coherence of the elementary sources has to be assessed in the case of plasma filaments. Since the optical pulse is progressively absorbed as it propagates through the medium, the energy deposition leading to the generation of acoustic pressure is also progressive. In this respect, the elementary sources are formed at different time instances and, therefore, their emission is not perfectly coherent. However, considering that the pulse propagates at the speed of light, the time difference in the plasma formation for the most remote points, the two edges of the plasma thread, is very small, i.e. for a 1-meter-long filament, $\Delta t = 3.33\ \mathrm{ns}$. Although such time differences could be relevant regarding ultrasounds in the MHz frequency range, they are practically negligible for the audio and near ultrasound frequencies that are of interest here.

Furthermore, the pressure excitation $n(t)$ of the elementary laser-induced plasma sources is difficult to model; femtosecond laser pulses undergo linear and non-linear transformations that depend on a multitude of optical parameters, such as optical pulse energy, duration, wavelength, as well as acoustic parameters, such as air temperature, humidity, and amplitude of the initial acoustic pressure and propagation velocity. For this reason, a phenomenological approach is adopted here. In Chapter 3 it was shown that laser-generated acoustic pulses are effectively modeled as triangular N-shaped pulses:

$$n(t) = -\frac{t}{T} \cdot [u(t+T) - u(t-T)] \tag{5.3}$$

where $u(t)$ is the unit step function and T is the half duration of the pulse. With the use of Eq. (5.3), Eq. (5.1) takes the form:

$$p(r,\phi,t) = -\int_{-L/2}^{L/2} \frac{H_x(x)}{r'(x)} \cdot \frac{t - r'(x)/c}{T} \cdot \left[u\left(t - \frac{r'(x)}{c} + T\right) - u\left(t - \frac{r'(x)}{c} - T\right)\right] dx \tag{5.4}$$

The model of Eq. (5.4) has also been proposed by Wright and Medendorp [10] for the study of sound generated by weak discharges (sparks), a phenomenon which is very similar to sound generation following laser-induced breakdown. As will be shown later, the assumption of ideal N-waves is particularly practical when the filament acoustic radiation is studied within a limited frequency range, such as the audible range, where acoustic N-pulses generally exhibit the characteristic 1st-order high pass profile.

Moreover, here, the initial pressure distribution $H_x(x)$ of the filament is estimated phenomenologically via the total irradiance of the light emitted from the plasma thread, as captured by a CCD imaging sensor. In Chapter 4 we showed that the photodiode measurements of the light signal following breakdown from nanosecond pulses consists of three main components: Bremsstrahlung, electron recombinations / deexcitations and thermal radiation. However, the plasma channels formed under the discussed experimental conditions are low-temperature and usually do not exceed temperatures in the order of 2000 K [11], in contrast to the plasmas discussed in Chapter 4, where the temperature can exceed 20000 K [12]. Therefore, there are essential differences in the light radiation following filamentation from femtosecond pulses, and particularly that the Bremsstrahlung and thermal components are almost absent [11]. As a result, the light captured by the CCD camera exclusively originates from electron recombinations; specifically, it is proportional to the time-integral of its radial intensity. In addition, Point et al. have carried out spatially resolved optical and acoustic measurements demonstrating that the filament's luminescence mainly originates from electron recombinations, which are strongly correlated to the acoustic pressure measured by a microphone [11]. Hence, the measured signal can be directly associated to the distribution of the acoustic pressure along the filament's axis [11][14].

Moreover, it is known [13][11][15] that the light intensity emitted from electron recombinations in laser plasma filaments exhibits a bell-curve or a flat-top distribution along the plasma channel, depending on the pulse energy and focusing conditions. As shown in the next subsection, for the optical parameters used in this work, the distribution adequately matches a bell curve, expressed mathematically by a Lorentzian function:

$$H_x(x) \backsim \frac{1}{1 + (x/\gamma)^2} \tag{5.5}$$

where γ is the parameter of the distribution. Note that, Eq. (5.5) gives the normalized longitudinal intensity of a Gaussian beam at zero radial distance from the core [16][17].

5.1.2 Experiments

Fig. 5.2 shows the experimental setup used to measure the acoustic waves generated by a laser plasma filament acoustic source in different angles with respect to the propagation axis of the pulse. A Ti:Sapphire laser (Amplitude Technologies, Pulsar PW [18], probe beam) delivering in these experiments 5.4 mJ optical pulses with $\sim 23\,\mathrm{fs}$ duration at Full Width at Half Maximum (FWHM) and $\lambda = \sim 800\,\mathrm{nm}$ central wavelength was used for the generation of the filament. The pulses were loosely focused using a lens of $f = 120\,\mathrm{cm}$ focal length, corresponding to $f/100$ focusing, to achieve self-guided plasma filament propagation via the interplay between Kerr self-focusing and plasma defocusing, as described in Chapter 2.

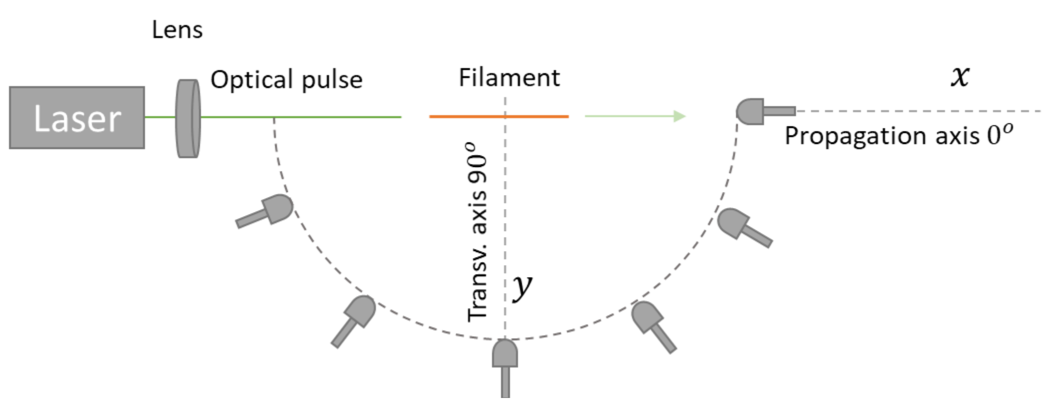

Fig. 5.2: Experimental setup of the acoustic measurements of the filament's sound radiation.

5.1.2.1 Optical measurements

An indicative plasma filament generated in the laboratory is shown in Fig. 5.3 a). The filament's luminescent light was captured with a CCD camera and the images were processed with image-processing software to extract the intensity distribution of the light emitted from the plasma thread along its axis. As illustrated in Fig. 5.3 b), the normalized plasma luminescence follows a bell-shaped curve with a single peak point which can be approximated by the Lorentz function of Eq. (5.5). By fitting the measured luminescence with Eq. (5.5), the distribution parameter was found $\gamma = 0.0149$ m. The FWHM of the filament was 3.2 cm and the total length of the thread was approximately 14 cm. These results are in agreement with the findings in [11], where measurements of the plasma luminescence from filaments generated under similar experimental conditions (5 mJ, 50 fs, $f/80$) are presented. The axial distribution of the intensity was used as the pressure scaling function $H_x(x)$ of the acoustic source, as shown in Fig. 5.3 b).

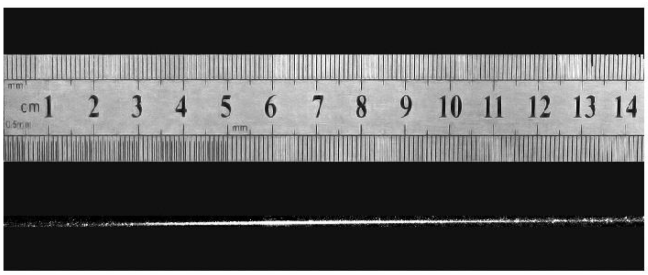

a)

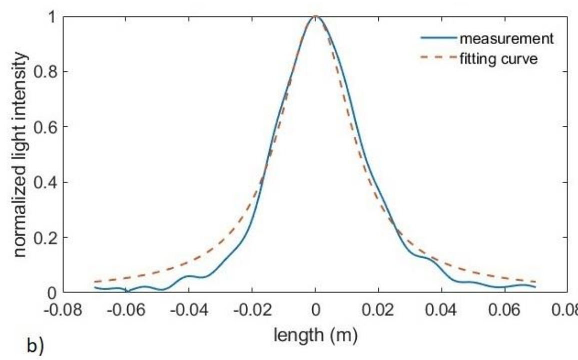

b)

Fig. 5.3: a) Plasma filament generated by 23 fs, 5.4 mJ, 800 nm laser pulses, focused with f/48, captured by a CCD camera and b) distribution of the intensity of the plasma luminescence along the filament axis extracted from a) using the ImageJ® image processing software [19].

5.1.2.2 Acoustic measurements

The acoustic signals were recorded using a GRAS 46BF-11/4-inch microphone (GRAS Sound & Vibration A/S, Holte, Denmark [20]) with a GRAS 12AA power module [21]. The data were acquired by an RME Fireface 802 sound card (Audio AG, Haimhausen, Germany [22]) at 192 kHz sampling rate and 24 bits resolution and they were recorded with the Audacity software [23]. The effective bandwidth of the measurement resulting from the combined frequency responses of the microphone and the sound card was approximately 5 Hz - 90 kHz. This bandwidth is not sufficient for the acquisition of the full frequency spectrum of the plasma filaments generated under these experimental conditions. From unofficial optical measurements carried out also in IPPL, it occurs that the acoustic spectrum extends deep into the ultrasounds, in contrast to the spectrum of the acoustic pulses generated by nanosecond lasers, whose energy is concentrated mainly in the high audible and near ultrasound range (see also Chapter 4). Nevertheless, this study focuses in the audible and near ultrasound spectrum, which is well covered by the measurement system.

To derive the acoustic directivity of the filament within the frequency range of observation, multiple measurements were carried out at different positions around the plasma thread, as shown in Fig. 5.2. The selected microphone spots formed a semicircle of $30\ \mathrm{cm}$ radius around the center of the filament, with a step of 15^{o} degrees. The measuring distance was selected to be sufficiently longer than the length of the plasma channel and at the same time short enough for the acoustic signal to be well above the noise floor of the measurement environment. Also, the measurements are in the far field of the acoustic source for the major part of the observed spectrum $(f > 2000\ \mathrm{Hz})$. The recordings at each spot contain 150 consecutive acoustic pulses; for each recording, the 150 individual pulses were isolated using Hanning windows $w_H(t)$ centered on the zero crossing of the pulse between the positive and the negative lobe. The individual pulses were averaged in order to derive representative acoustic signals $p_{\mathrm{avg}}(t, \varphi)$ for each measuring angle. This was necessary here because the filament formation under the loose focusing conditions and the relatively small pulse energy is moderately repeatable.

5.1.3 Excitation pressure modeling

As a final step, the exact profile of the elementary pressure excitation function $n(t)$ had to be determined and, particularly, the duration of the N-pulse, which has a direct impact on the distribution of the acoustic energy across the frequency spectrum. With the use of tight focusing ($f/6$), the laser pulses formed a roughly spherical plasma volume with a sub-millimeter radius. Such a plasma volume can be considered as pointlike compared to the size of the filament. With this assumption, the pressure excitation of the elementary sources of the acoustic line was acquired by fitting the ideal N-wave of Eq. (5.3) on the acoustic signal captured from these pointlike sources.

In order to derive an analytical expression for the elementary source excitation, hereafter called the modeled pulse, the following aspects have to be considered:

a. The measured acoustic signal is the result of low-pass filtering of the ideal N-pulse with the microphone response and the anti-aliasing low-pass filter of the sound card, which effectively limits the upper frequency to $90\ \mathrm{kHz}$ range.
b. The effect of the Hanning window $w_H(t)$.

The combined linear band limiting effect of point a. can be described by convolution of the ideal pulse with the impulse response $h_c(t)$ of the acoustic measurement system, while the effect of the Hanning filter corresponds to a multiplication with $w_H(t)$. Hence, the modeled pulse $n_m(t)$ is expressed by:

$$n_m(t) = w_H(t) \cdot [n(t) * h_c(t - \tau)] \tag{5.6}$$

where $*$ is the convolution operator. Fig. 5.4 a) illustrates the process followed for the derivation of the signal $n_m(t)$ from the ideal pulse $n(t)$ by fitting of the transformed pulse of Eq. (5.6) to the measured pulse. Fig. 5.4 b) shows the spectra of the measured, ideal, and modeled pulse obtained via fast Fourier transform, showing the very good agreement between the measured and the modeled pulse.

As a note, the pressure produced by the filaments in the described experiments is relatively low [11][27][28] compared to pressures from the tightly focused pulses [24][25][26]. However, quantitative analysis of the pressure amplitude generated by plasma filaments is beyond the scope of this work and will be studied in the future. Also, it can be easily seen that this precise modeling of the measured N-pulse is not necessary if the calculation of the filament's acoustic radiation is carried out for a limited frequency range where the experimental N-pulse exhibits the characteristic 1st-order N-pulse profile.

Finally, by substituting Eq. (5.5) and (5.6) into Eq. (5.7), the analytical expression of the pressure $p(r, \phi, t)$ becomes:

$$p(r, \phi, t) = \int_{-L/2}^{L/2} \frac{1}{r'(x) \cdot \left(1 + \left(\frac{x}{\gamma}\right)^2\right)} \cdot n_m\left(t - \frac{r'(x)}{c}\right) dx \quad (5.7)$$

The simple phenomenological model of Eq. (5.7) can be used to evaluate various characteristics of the acoustic emission of plasma filaments, given that their basic geometrical characteristics are known. By providing the full width of the filament and the distribution of the axial pressure distribution, the normalized acoustic pressure can be calculated at any point in the 3D space. In the next subsection it is demonstrated that the model is especially suitable for the estimation of the filament's acoustic emission in the frequency domain, but also for the calculation of its directivity.

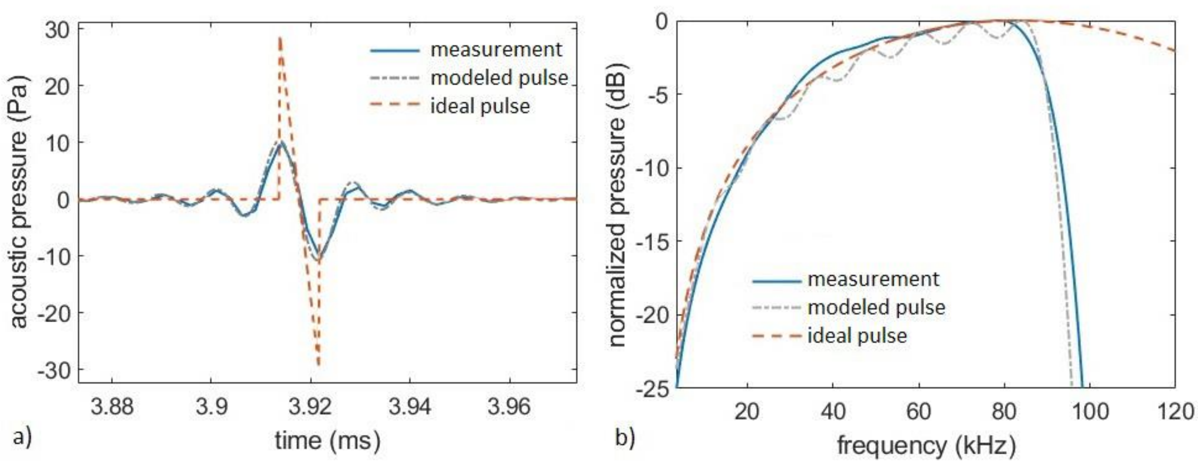

Fig. 5.4: a) Acoustic pressure in the time domain and b) frequency spectra of measured (blue line), ideal (red line), and modeled (dashed gray line) LIB acoustic pulse generated by 23 fs (FWHM) laser pulses with 5.4 mJ energy under tight focusing. The modeled pulse is used as excitation for the spherical elementary sources.

5.2 Characteristics of the filament sound emission

To validate the proposed model of Eq. (5.7), the directivity plots of the plasma filament with 14 cm length were derived via simulation and measurements and the results were compared. Since filamentation is only moderately repeatable in the parameter range of the experiments, there are pulse-to-pulse differences in the measured waveforms, rendering single acoustic pulses inappropriate for the validation process. For this reason, the comparisons were based on the acoustic energy emitted at different angles with respect to the axis of the filament. It is shown that this directivity-based approach provides concrete results, especially by averaging over a large number of acoustic pulses.

Eq. (5.7) was solved using numerical integration inside a semicircle of radius $r = 30$ cm. A time window of 10 ms was used with 200 ns time discretization, corresponding to a sampling rate of 5 MHz and a Nyquist frequency of 2.5 MHz. The spatial resolution was 200 μm, resulting for the 14 cm plasma channel to 780 elementary sources. Due to the cylindrical symmetry of the plasma filament, evaluations on the polar plane are sufficient for the deduction of the directivity in the full 3D space.

5.2.1 Model validation and acoustic directivity of laser filaments

Fig. 5.5 a) presents the directivity plot of the measured and modeled laser filament acoustic sources within the observable frequency range. As for classic acoustic sources, the acoustic directivity of laser filaments can be represented by the polar diagram of the normalized equivalent Sound Pressure Level (SPL) L_{eq} plotted on a logarithmic scale. Due to the approximately symmetric geometry of the plasma threads around the origin, the polar plots are confined to the half polar plane while a mirrored directivity is implied for the hidden half-plane. The measurements correspond to angles $90^o, 75^o, 60^o, 45^o, 30^o$ and 15^o degrees. The sound pressure levels for each emission angle were obtained by averaging over the L_{eq} of the measured 150 individual pulses. It can be seen that the simulations are in excellent agreement with the experiments, demonstrating the validity of the acoustic model.

In analogy to the acoustic line source [8][10] the radiation of the plasma filament is maximum on the y axis ($\phi = 90°$), while it significantly weakens towards the x axis ($\phi = 0°\ or\ 180°$). It is known that the high acoustic frequencies tend to be strongly directional, with classical examples being the high-frequency electromechanical transducers (tweeters) and the piezoelectric transducers. Since most of the acoustic energy of the plasma filament lies in the ultrasound range, it is expected that the source will have an overall directional emission. In order to identify the behavior of the filament in different frequency ranges, the acoustic pulses were analyzed in frequency bands.

This was done here for the audio bands with central frequencies $2\mathrm{kHz}, 4\mathrm{kHz}, 8\mathrm{kHz}$ and $16\mathrm{kHz}$. The band-related pressure $p_f(r, \phi, t)$ was taken by convolution of the total measured and evaluated pressure $p(r, \phi, t)$ with the impulse response $h_f(t)$ of a band-pass filter. Digital filters from a filterbank complying with the ANSI S1.11-2004 standard were used [29]. Fig. 5.5 b) presents the acoustic directivity of the source in distinct octave bands at the mentioned central frequencies. It becomes apparent that the filament's radiation is moderately directional in the $2\,\mathrm{kHz}$ band, with the difference between the strongest and weakest pressure level at 90^{o} and 0^{o} degrees respectively being less than $10\,\mathrm{dB}$. In contrast, for the $16\,\mathrm{kHz}$ band, the filament becomes strongly directional with a highest L_{eq} difference of $30\,\mathrm{dB}$. Fig. 5.5 b) also demonstrates the good match between the model and the measurements for all the octave bands. Finally, Fig. 5.6 presents the directivity of the $14\,\mathrm{cm}$ plasma channel in the full audible spectrum ($20\,\mathrm{Hz} - 22.05\,\mathrm{kHz}$). It can be seen that the filament is a directional source in the audio range, with a maximum L_{eq} deviation of more than $20\,\mathrm{dB}$.

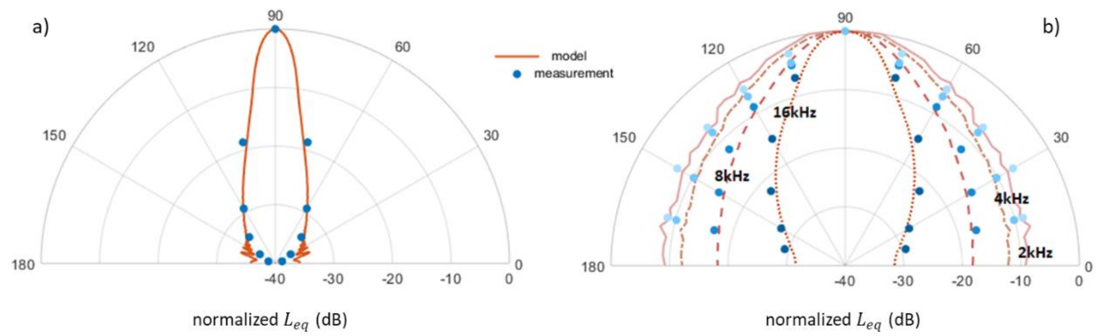

Fig. 5.5: Polar diagrams of the acoustic radiation of the 14cm laser filament: measurement and model evaluation based on: a) the total L_{eq} and b) the L_{eq} calculated in ANSI S1.11-2004 octave bands [29]. The filament lies along the horizontal axis.

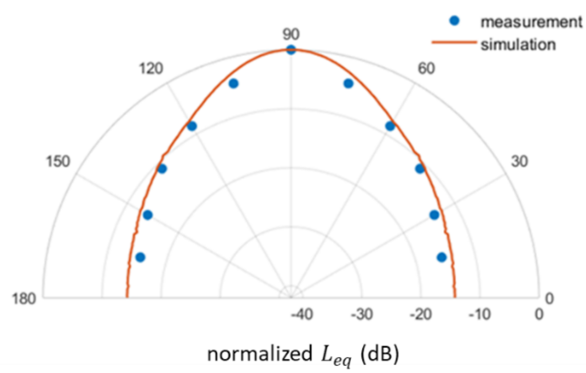

Fig. 5.6: Polar diagram of the acoustic emission of the 14cm laser filament in the audible spectrum (20Hz-20kHz).

5.2.2 Acoustic spectrum of laser filaments

As with the acoustic energy, the acoustic spectrum of laser filaments depends on the angle of emission. The polar diagrams of Fig. 5.4 b) already provide clear indications about this dependence: in the lower frequencies (i.e. $2\,\mathrm{kHz}$ octave band), the radiation is almost omnidirectional while in the higher frequencies (i.e. $16\,\mathrm{kHz}$ octave band) the radiation fades out in the directions close to the filament's axis. This can be explained by the fact that the high-frequencies are present only for larger emission angles, while the low-frequencies are omnidirectional and do not exhibit a strong dependence from the emission

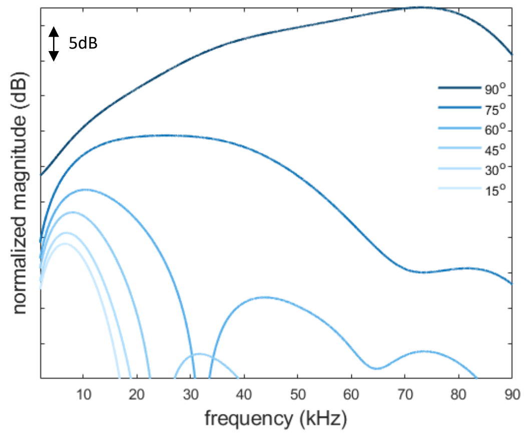

Fig. 5.7: Measured frequency spectra of the filament's acoustic radiation at different angles.

angle. This can be clearly seen in Fig. 5.7, where the acoustic spectra of the averaged pulses $p_{\mathrm{avg}}(t,\varphi)$ are plotted. It becomes evident that the high frequencies are significantly suppressed with decreasing angle of emission, while the low frequencies are less affected by the emission angle.

In the previous subsection it was shown that the presented phenomenological model is very accurate in the prediction of the acoustic energy emitted by plasma filaments, also for specific frequency bands. However, the prediction of the acoustic spectra is more challenging due to the moderate repeatability in the formation of the plasma channel that leads to significant differences in the pulse-to-pulse acoustic profiles. This can be seen in Fig. 5.8, where 3 consecutive acoustic pulses measured at 60^o are shown along with their frequency spectra. Despite the obvious differences in the time- and frequency-domain profiles of the pulses, there is consistency in the lower end of the spectrum, from the very low audible frequencies and up to the near ultrasounds. This is reflected also in the predictions of the acoustic model. Fig. 5.9 presents the normalized acoustic spectra of the averaged measured pulses $p_{\mathrm{avg}}(t)$ compared to the predictions of the model at 90°, 75°, 60° and 45° degrees. It can be seen that prominent spectral

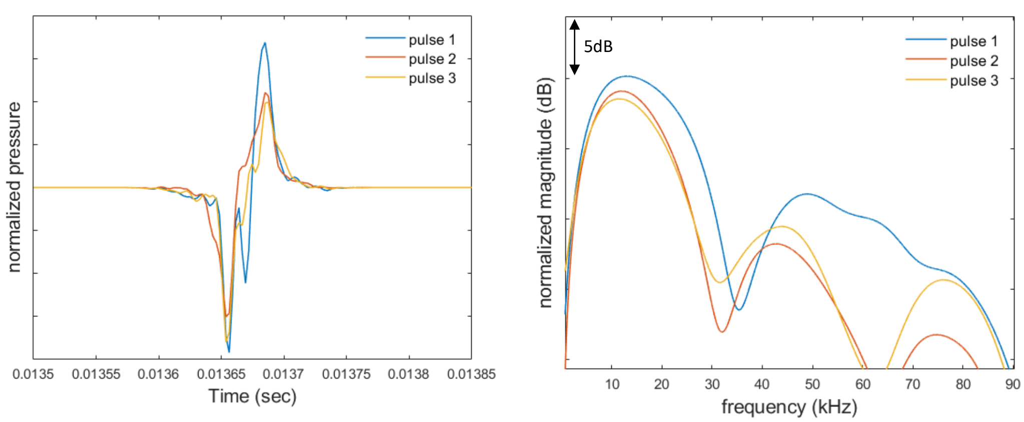

Fig. 5.8: a) Consecutive acoustic pulses following filamentation measured at an angle of 60^o and b) their frequency spectra.

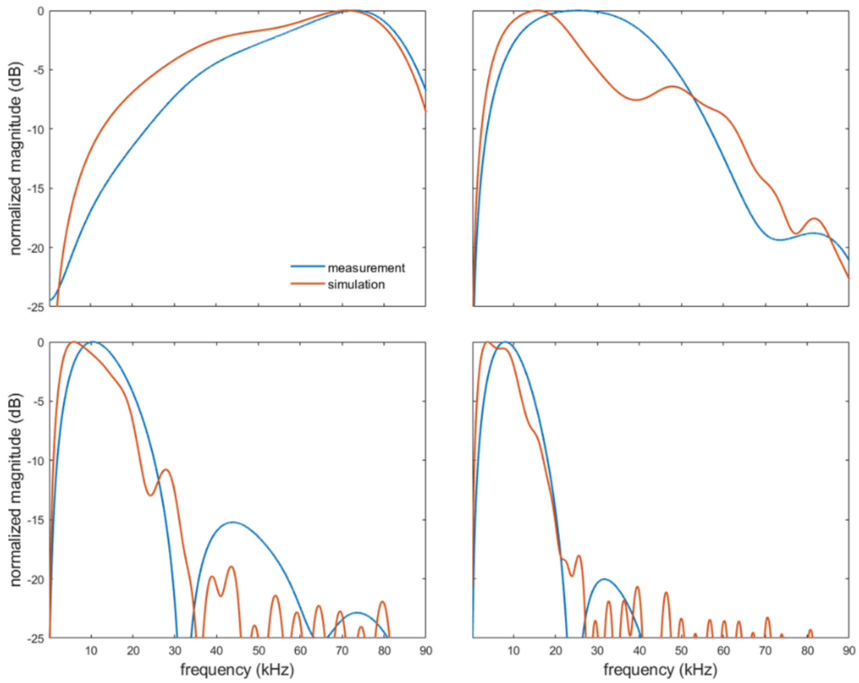

Fig. 5.9: measured and calculated normalized frequency spectra of the filament's acoustic radiation at a) 90°, b) 75°, c) 60° and d) 45° degrees.

features of the acoustic pulses, such as the main lobe in the lower end of the spectrum, are predicted with an approximate deviation of 5 dB, while in the low frequencies, some ripples appear in the model that are independent of the resolution used for the evaluation.

5.2.3 Dependence of the acoustic emission from the filament's geometry

Having proved that the acoustic model is appropriate for the estimation of the main acoustic characteristics of plasma filaments, this subsection investigates the impact of the filament's geometry on its acoustic emission. Considering that the elementary pressure excitation obtained by Eq. (5.3) and (5.6) does not depend on the characteristics of the filament, the filament's acoustic emission can be fully determined by (see Eq. (5.7)):

a. the length L of the plasma thread,
b. the axial distribution $H_x(x)$ of the deposited energy

In the following paragraphs, different lengths and distribution functions are investigated with respect to their impact on the filament's acoustic directivity and spectrum [28]. It should be noted that the study presented here is limited to computational results and will be complemented in the near future with experimental evaluations.

5.2.3.1 Length of the plasma thread

In order to study the impact of the length of the plasma thread in the filament's acoustic radiation, the directivities of four filaments with identical Lorentzian axial distributions but different lengths are evaluated through the line source model of Eq. (5.7). Table I shows the parameters of the four filaments with lengths of $3.5, 7, 14$ and $28\mathrm{cm}$ respectively. The simulation distance was increased to $70\ \mathrm{cm}$ in order to be in the far field even for the longest filament. The directivities within the audible frequency range and the full observation range are shown in Fig. 5.10 a) and b) respectively. It becomes evident that the length of the filament is a decisive factor for the filament's directivity and, as also expected from the classical acoustic line sources, the longer the filament, the more directional its acoustic emission. Interestingly, the shortest filament is almost omnidirectional within the audible frequency range while the longest filament is strongly directional. From the simulations it arises that the acoustic behavior of the filaments is highly dependent on their length.

Table I: filament parameters

Length (cm)	FWHM (cm)	γ parameter (cm)
3.5	0.75	0.37
7.0	1.49	0.75
14.0	2.98	1.49
28.0	5.96	2.98

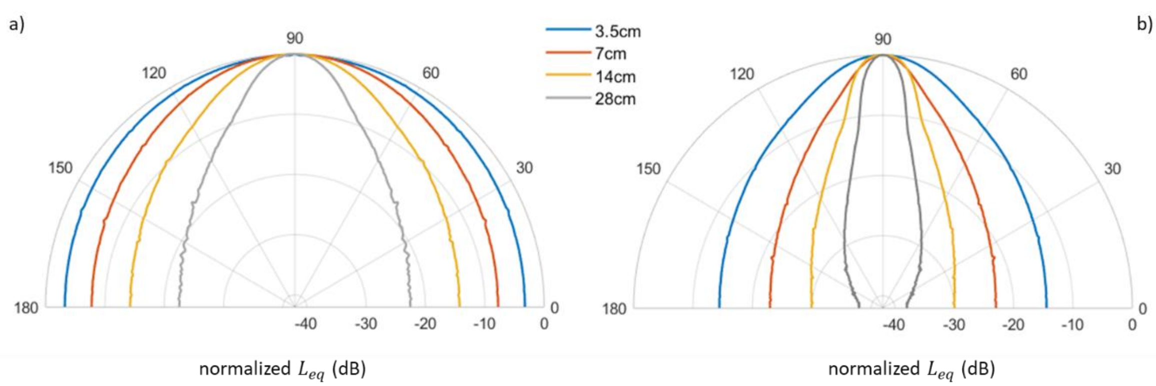

Fig. 5.10: simulated directivity plots of the acoustic radiation of plasma filaments with different lengths within: a) the audible spectrum and b) the full observation spectrum.

5.2.3.2 Distribution of the deposited energy

It was mentioned earlier that the distribution of the deposited energy along the axis of laser filaments can be approximated by bell-shaped or flat-top functions [11][13][15][28]. To evaluate the effect of the axial distribution of the deposited energy on the filament's acoustic emission, three additional plasma channels with $14\ \mathrm{cm}$ length are simulated with a) a Gaussian function:

$$H_x^N(x) \sim e^{-\frac{x}{2\sigma^2}^2} \tag{5.8}$$

which is bell-shaped and b) 4th and 6th order Super-Gaussian functions:

$$H_x^{N_n}(x) \sim e^{-\frac{x^2}{2\sigma_n^2}}, \qquad n = 4, 6 \tag{5.9}$$

which are flat-top. For the results to be comparable, the distribution parameters were calibrated so that the integral:

$$E_{tot} = \int_{-L/2}^{L/2} H_x(x)dx \tag{5.10}$$

of the normalized deposited energy over the length of the filament was equal for all the distribution functions. The distribution functions are shown in Fig. 5.11.

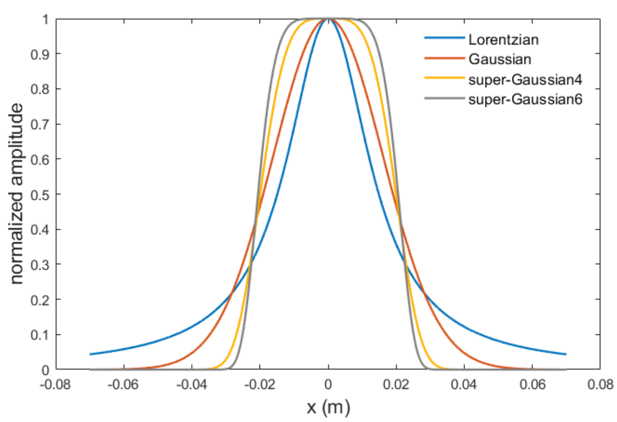

Fig. 5.11: simulated distribution functions representing the optical energy deposition along the axis of the filament.

Fig. 5.12 a) and b) show the comparative directivity plots for the audible frequency range and the full observable range, respectively. It can be seen that the distributions with heavier tails lead to more directional acoustic emission than the flat-top distributions. This is expected since the flat-top distributions effectively confine the area of the acoustic emission and lead to sound sources with smaller dimensions, which, as shown in the previous subsection, have a less directional emission. Finally, from Fig. 5.12 it becomes evident that the particular shape of the pressure distribution $H_x(x)$ has a much smaller impact on the acoustic emission of the filament, compared to the length of the plasma channel.

5.3 Enhanced filament acoustic radiation model

In this section, a more detailed physical model for the calculation of the acoustic emission of plasma filaments is outlined, based on the heat-source model presented in Chapter 4. Preliminary results from the evaluation of a scaled plasma filament show that the model captures the basic characteristics of the acoustic emission of plasma filaments and allows for the precise calculation of their acoustic spectra at any position in 3D space.

To develop such a model, the geometrical characteristics of the filament plasma channel have to be imposed on the geometry of the heat source. Due to cylindrical symmetry, the wave equation with a heat source presented in section 4.2 (Eq. (4.7)) can be written in cylindrical coordinates (x, r, φ) [30]:

$$\left(\nabla^2 - \frac{1}{c^2}\frac{\partial^2}{\partial t^2}\right) \cdot p(x, r, t) = -\frac{\gamma - 1}{c^2} \cdot \frac{\partial}{\partial t} H(x, r, t) \tag{5.11}$$

The filament heat source $H(x, r, t)$ can be expressed in terms of three functions:

$$H(x, r, t) = H_x(x) \cdot H_r(r) \cdot H_t(t) \tag{5.12}$$

where $H_x(x)$ and $H_r(r)$ describe the spatial distribution of the thermal energy along the axial x and radial r dimension and $H_t(t)$ describes the time evolution of the thermal energy in the heated volume. In order to determine the function $H(x, r, t)$, some further considerations have to be made. For the axial distribution $H_x(x)$ of the thermal energy it was demonstrated earlier in this chapter that it can be approximated by a Lorentzian function:

$$H_x(x) \sim \frac{1}{1 + (x/\gamma)^2} \tag{5.13}$$

In the radial dimension, according to Eq. (4.18) of Chapter 4, the thermal energy distribution can be considered to be a Gaussian:

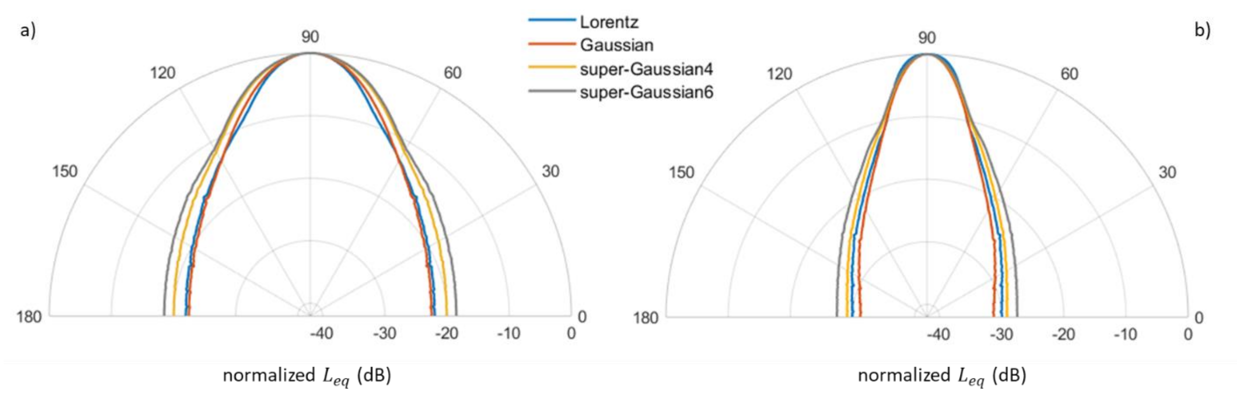

Fig. 5.12: simulated directivity plots of the acoustic radiation of four filaments with different axial pressure distributions within: a) the audible spectrum and b) the full observation spectrum.

$$H_r(r) \sim e^{-\frac{r^2}{2\sigma_r^2}} \tag{5.14}$$

with σ_r the width parameter of the distribution. Ultimately, for the time evolution of the thermal energy either a bell-shaped or a flat-top function can be used. In the presented simulations, a 4th-order super-Gaussian function was selected [13]:

$$H_y(y) \sim e^{-\left(\frac{t^2}{2\sigma_t^2}\right)^2} \tag{5.15}$$

This is in accordance with the findings presented in subsection 4.1.2.2, where the analysis of the optical signal captured by a photodiode resulted to the isolation of the component of the thermal energy. Fig. 5.13 shows a 4th-order super-Gaussian function fitted to the measured temporal profile of the thermal energy, obtained from Eq. (4.16). The good match proves that the function of Eq. (5.15) is an adequate qualitative approximation of the time evolution of the thermal energy. It should be noted that, although the thermal signal is obtained by air breakdown from nanosecond pulses, the temporal profile of the thermal energy does not significantly change in case of femtosecond lasers. This is due to the fact that the thermalization of the targeted medium is a secondary phenomenon which results from the interactions of the free electrons with the heavy particles in the interaction volume [31]. The time scales of these interactions are largely independent from the duration of the laser excitation, and thus, it can be considered that the thermal energy has qualitatively an identical temporal profile.

Under these assumptions, the heat source is finally written as:

$$H_t(x, y, t) = \frac{1}{1 + (x/\gamma\,)^2} \cdot e^{-\left(\frac{y^2}{2\sigma_y^2} + \frac{t^4}{4\sigma_t^4}\right)} \tag{5.16}$$

and Eq. (5.12) becomes:

$$\left(\nabla^2 - \frac{1}{c^2}\frac{\partial^2}{\partial t^2}\right) \cdot p(x, y, t) = \frac{\gamma - 1}{(1 + (x/\gamma)^2)c^2\sigma_t^4} t^3 e^{-\left(\frac{y^2}{2\sigma_y^2} + \frac{t^4}{4\sigma_t^4}\right)} \tag{5.17}$$

Eq. (5.17) was solved numerically in MATLAB [32]. The parameters of the scaled model used in the simulation are shown in Table II and the simulation results are shown in Fig. 5.14. Fig. 5.14 a) presents a two-dimensional heatmap of the pressure generated by the filament at the early stages of its acoustic emission. The strongly directional emission in the direction perpendicular to the axis of the filament can be clearly identified from the bright red color on the upper and lower sides of the filament and the faded red color on the right and left sides of the filament. Fig. 5.14 b) shows the frequency-domain representation of the acoustic pressure of the filament as obtained from the model at 3 different angles of the polar plane.

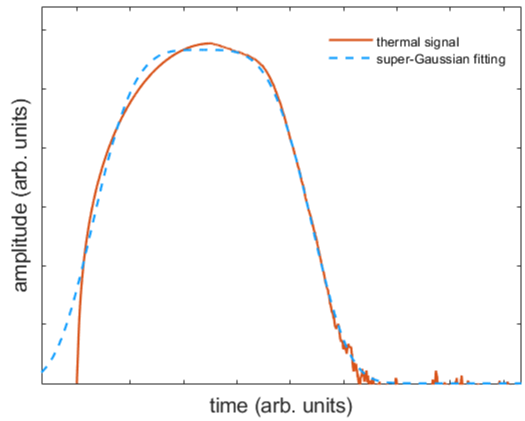

Fig. 5.13: 4th-order super-Gaussian fitting of the measured temporal profile of the thermal energy from obtained from Eq. (4.16) of Chapter 4.

Table II: scaled model parameters

parameter	value
γ	$0.081\ (m)$
σ_r	$6.910 \times 10^{-4}\ (m)$
σ_t	$2.001 \times 10^{-4}\ (s)$

As expected, the sound pressure is stronger on the transverse axis y ($\varphi = 90^o$) and fades for smaller angles with respect to the filament axis. Also, for the smaller angles, the characteristic spectral dips

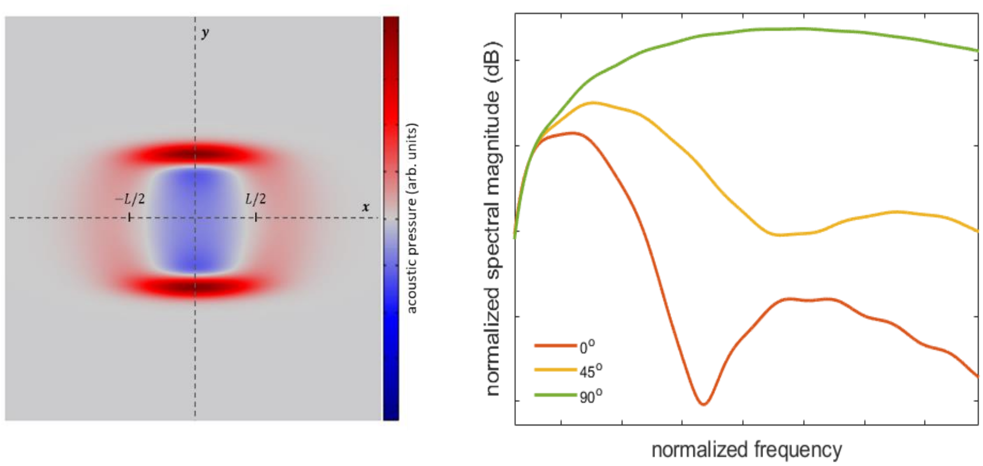

Fig. 5.14: Results from a scaled filament model, simulated via the heat source model, a) two-dimensional heatmap of the pressure generated by the filament at the early stages of its acoustic emission and b) frequency-domain representation of the acoustic pressure of the filament as obtained from the model at 3 different angles of the polar plane.

appearing in the measured frequency spectra are present (see also Fig. 5.7). These qualitative results demonstrate that the physical model of Eq. (5.17) can successfully capture the main characteristics of the filament's acoustic radiation. In the near future, a real-scale model will be developed and compared to the acoustic model and the measurements.

Conclusions

In this Chapter, the acoustic radiation of plasma filaments generated by femtosecond laser pulses was systematically studied experimentally and analytically. A set of acoustic measurements was acquired for plasma filaments of 14 cm length and 3.2 cm length at FWHM through which, the acoustic directivity of these elongated plasma sound sources was experimentally evaluated. Moreover, a simple phenomenological model was developed for the estimation of the acoustic directivity and frequency spectra of plasma filaments based on the classical acoustic line source model and utilizing concepts of the physics of laser filament generation and the correlation between light and sound following laser-induced breakdown, presented in Chapter 4. The predictions of the model on the acoustic directivity and the frequency spectra of plasma filaments at various angles were validated by comparison with the measurements, showing good agreement both within the audible frequency range and in the complete frequency range of observation. This parallel experimental and computational study demonstrated that the acoustic radiation of plasma filaments can be modeled using principles of linear acoustics.

The acoustic line source model was used to study the dependence of the acoustic radiation of plasma filaments from the geometrical characteristics of the plasma channel, particularly the initial pressure distribution along the filament's axis and the length of the channel. Typical bell-shaped (Lorentzian and Gaussian) and flat-top (super- Gaussian of 4^{th} and 6^{th} order) were used to represent the thermal energy distribution along the axis of the plasma thread. The simulations showed that the acoustic radiation of filaments with a flat-top distribution is less directional than that of filaments with bell-shaped distributions; however, the dependence was found to be relatively weak. On the contrary, it was shown that there is a strong dependence of the filament's acoustic radiation from the length of the plasma thread. As expected from the classical counterparts, longer plasma threads exhibit stronger acoustic directivity in the far field, while shorter threads are less directional, with the emission becoming omnidirectional in the audible frequency range for plasma channels in the order of a few centimeters.

Finally, a physical model describing the acoustic radiation of laser filaments based on the heat-source model of Chapter 4 was outlined. Preliminary results from the simulation of a scaled plasma thread demonstrated that such a model can successfully capture the directional characteristics of the filament's acoustic emission. In the near future, experiments with filaments of different lengths and real-scale simulations will be carried out in order to validate the physical model.

References

[1] Eskelinen, J., Hæggström, E., Delikaris-Manias, S., Bolaños, J. & Pulkki, V. Beamforming with a volumetric array of massless laser spark sources—application in reflection tracking. J. Acoust. Soc. Am. 137, 389–395 (2015).

[2] Gómez-Bolaños, J. et al. Benefits and applications of laser-induced sparks in real scale model measurements. J. Acoust. Soc. Am. 138, EL175–EL180 (2015).

[3] Delikaris-Manias, S., Bolaños, J. G., Eskelinen, J., Huhtakallio, I., Hæggström, E., & Pulkki, V., Auralization of source radiation pattern synthesized with laser spark room responses. Journal of the Audio Engineering Society, 64(10), 720-730 (2016).

[4] Couairon, A., & Mysyrowicz, A. Femtosecond filamentation in transparent media. Physics Reports, 441(2-4), 47–189 (2007).

[5] Couairon, A., Tzortzakis, S., Bergé, L., Franco, M., Prade, B. & Mysyrowicz, A. Infrared femtosecond light filaments in air: simulations and experiments. Journal of the Optical Society of America B, 19(5), 1117 (2002).

[6] Papeer, J., Botton, M., Gordon, D., Sprangle, P., Fibich, G., Herzig Sheinfux, H., Zigler, A. & Henis, Z. Multi variable control of filamentation of femtosecond laser pulses propagating in air. Journal of Physics B: Atomic, Molecular and Optical Physics, 48(9), 094005 (2015).

[7] Wolff, I. & Malter, L., Directional radiation of sound, J. Acoust. Soc. Am. 2(2), 201–241 (1930)

[8] Kinsler, L. E. *Fundamentals of Acoustics*, John Wiley & Sons, New York (2000)

[9] A. J. Rudgers, Experimental detection of boundary diffraction waves irradiated by an impulsively excited line source of finite length, J. Acoust. Soc. Am. 67(S1), S3 (1980).

[10] Wright, W. M. & Medendorp, N. W. Acoustic radiation from a finite line source with N-wave excitation, J. Acoust. Soc. Am. 43(5), 966–971 (1968).

[11] G. Point, Energy deposition in air from femtosecond laser filamentation for the control of high voltage spark discharges, Ph.D. thesis, Ecole Polytechnique, Laboratoire d'Optique Appliquée (2015).

[12] Aguilera, J. A., & Aragón, C. Characterization of laser-induced plasma during its expansion in air by optical emission spectroscopy: Observation of strong explosion self-similar behavior. Spectrochimica Acta Part B: Atomic Spectroscopy, 97, 86–93 (2014).

[13] Jukna, V. et al. Underwater acoustic wave generation by filamentation of terawatt ultrashort laser pulses, Phys. Rev. E 93, 063106 (2016).

[14] Kaleris, K., Orphanos, Y., Bakarezos, M., Dimitriou, V., M., Tatrakis, M., Mourjopoulos, J. & Papadogiannis, N. On the correlation of light and sound radiation following laser-induced breakdown in air, Journal of Physics D: Applied Physics (2020).

[15] Mysyrowicz, A., Couairon, A., & Keller, U. Self-compression of optical laser pulses by filamentation, New J. Phys. 10(2), 025023 (2008).

[16] E. Hecht, Optics (Pearson, San Francisco, 2012).

[17] R. W. Boyd, Nonlinear Optics, 3rd ed. (Academic Press, Inc., Orlando, FL, 2008).

[18] Pulsar PW. Amplitude. (2020, December 4). https://amplitude-laser.com/products/lasers-for-science/pulsar-pw/

[19] "Imagej," https://imagej.nih.gov/ij/ (Last viewed August 4, 2019)

[20] Gras 46be 1/4" ccp free-field standard microphone set. (n.d.). Retrieved May 14, 2021, from https://www.grasacoustics.com/products/product/143-46be.html

[21] GRAS 12AK 1-Channel power module With Gain, filters AND SYSCHECK GENERATOR. (n.d.). Retrieved May 14, 2021, from https://www.grasacoustics.com/products/power-module/traditional-power-supply-lemo/product/225-12ak

[22] Fireface 802. RME Audio Interfaces | Format Converters | Preamps | Network Audio & MADI Solutions. (n.d.). https://www.rme-audio.de/fireface-802.html

[23] Audacity Team. Web site: https://audacityteam.org/. The name Audacity® is a registered trademark of Dominic Mazzoni.

[24] Gomez Bolaños, J., Delikaris-Manias, S., Pulkki, V., Eskelinen, J. & Hæggström, E. Laser-induced acoustic point source for accurate impulse response measurements within the audible bandwidth, J. Acoust. Soc. Am. 135(6), EL298–EL303 (2014).

[25] Qin, Q. & Attenborough, K. Characteristics and application of laser-generated acoustic shock waves in air, Appl. Acoust. 65(4), 325–340 (2004).

[26] Oksanen, M. & Hietanen, J., Photoacoustic breakdown sound source in air, Ultrasonics 32, 327–331 (1994).

[27] Kaleris, K., Orfanos, Y., Bakarezos, M., Papadogiannis, N. & Mourjopoulos, J. Experimental and analytical evaluation of the acoustic radiation of femtosecond laser plasma filament sound sources in air. The Journal of the Acoustical Society of America 146, EL212-EL218 (2019)

[28] Kaleris, K., Orphanos, Y. Bakarezos, M. Papadogiannis, N., & Mourjopoulos, J. "The effect of plasma geometry on the acoustic radiation of laser filaments", proceedings of Forum Acusticum, Lyon (2020)

[29] ANSI S1.11-2004, Octave-band and Fractional-octave-band Analog and Digital Filters, American National Standards Institute, New York (2004).

[30] Diebold, G. J. "Application of the Photoacoustic Effect to Studies of Gas Phase Chemical Kinetics", *Topics in Current Physics Vol.46: Photoacoustic, Photothermal and Photochemical Processes in Gases*, edited by Peter Hess, Springer, (1989).

[31] Zel'dovič, J. & Rajzer, J. *Physics of shock waves and high-temperature hydrodynamic phenomena*. Acad. Pr. (1970).

[32] MATLAB, version R2018b, The MathWorks Inc., Natick, MA (2018).

Chapter 6

Laser-sound: optoacoustic transduction from digital ΣΔ audio streams

Contents

Introduction

Laser-sound is a proposed novel transduction technology for the controlled reproduction of arbitrary sound signals via virtual massless plasma sources generated by intense laser pulses in ambient air or liquids or on solid targets. It aims to provide an alternative solution and address limitations of the current moving-coil transducer technology through the realization of flexible compact sound reproduction systems with ample acoustic power, equalized frequency response, improved efficiency and potentially controllable directivity, that are suitable for generating rapid acoustic signals and for rendering moving sound sources or holographic auditory scenes.

In Chapters 1 and 2, the concepts and techniques for sound generation from laser-plasma acoustic sources were presented, including:

a. the audio encodings for sound reproduction from pulsed audio streams
b. the physics behind laser-plasma sources generated in ambient air or on solid targets

Based on these aspects, in this Chapter a novel optoacoustic transducer prototype is presented, capable of reproducing arbitrary continuous and controlled acoustic signals via laser-induced breakdown directly in the air or via laser ablation on metal targets. The transducer is based on a single laser unit emitting intense laser pulses at sufficiently high repetition rates, allowing for fast consecutive optical excitation of the target medium. The laser system is driven by Sigma-Delta (ΣΔ) or Pulse Amplitude Modulation (PAM) digital audio signals, which allow for the transcoding of complex audio information into streams of laser-generated acoustic N-waves.

Experimental evaluations of the prototype transducer were carried out at a proof-of-concept level by reproduction of test audio signals, particularly single sine waves, sine sweeps, speech and music signals. The measurements are supported by evaluations from a linear computational model, which calculates the output of the optoacoustic transducer as a function of the driving audio stream and the profile of the laser-generated acoustic N-wave. Due to limitations in the available laser repetition rate and optical power, the current prototype achieves reproduction within a restricted frequency range of the audible spectrum. However, the excellent agreement between the experiments and the predictions of the model allow for generalization of the results to the full audible range, given a laser with adequate specifications.

6.1 System overview

Laser-sound deploys well-established pulsed audio modulation techniques for the reproduction of arbitrary sound signals from laser-generated plasma sound sources. The general schematic diagram of a laser-sound optoacoustic transducer driven by digital ΣΔ streams is shown in Fig. 6.1. The core of the system constitutes a high energy, high repetition rate pulsed laser, producing intense short or ultrashort pulses capable to induce breakdown in air or on solid targets [1][3][4]. The laser unit is driven and controlled by a radiation control system which enables the modulation of the optical pulse stream over:

a. pulse-to-pulse time distance and
b. pulse energy

Through the control system, instant variation of the generated acoustic pulse density and per-pulse produced acoustic pressure is achieved, so that the appropriate pulsed audio coding is realized. For this purpose, the laser unit is driven by two control signals, namely a laser trigger signal (s_{trig}) and a radiation modulation signal (s_{mod}), which are delivered by a control interface. The s_{trig} signal evokes laser pulse emission, essentially constituting a pulse / no-pulse control, while the s_{mod} signal constitutes a real-time modulation of the emitted optical energy, achieved via an electro-optic modulator (EOM). The signals s_{trig} and s_{mod} are deduced from a ΣΔ audio bitstream ($s_{\Sigma\Delta}$) produced by ΣΔ modulation of the input audio signal s_{audio}. The signal s_{audio} can either be analog or digital (PCM) and contains the original band-limited audio stream to be reproduced by the laser-sound transducer. Potentially, signal pre-processing can be applied on s_{audio} before modulation, for equalization of the system's frequency response (see Section 6.7.2). Finally, the emitted optical pulse stream is focused by a lens on a targeted medium, which can either be ambient air or a liquid or solid material placed at the laser's focal spot.

The adoption of the ΣΔ modulation emerges naturally from the physical characteristics and requirements of the laser-sound system and its suitability to produce acoustic pulse streams. From a physics point of view, the N-shaped acoustic pulses generated by gas breakdown or ablation of solids have a duration of several tens of microseconds [5][6][7], allowing for the formation of dense acoustic pulse streams with real-time controllable pulse-to-pulse time intervals. Similarly, from a signal point of view, although the frequency spectrum of such laser-generated ΣΔ streams extends well beyond the frequency range of the input signal, the spectral content of the input signal is maintained in the in-band range of the modulated

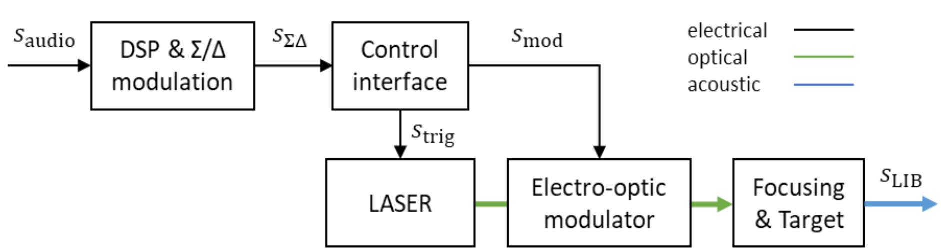

Fig. 6.1: Conceptual diagram of the laser-sound optoacoustic transducer.

signal with negligible distortion. Consequently, demodulation of the laser-generated acoustic pulse stream solely requires low-pass filtering to remove the spectral components outside the audible frequency range, a process that is naturally done by the human auditory system. This effectively enables sound reproduction directly in the air or on solid targets at any position in space by optical pulses carrying both the information signal and the power required for the transduction, without the need for in-situ receiver or demodulation devices [8][9].

6.2 Technical description of the laser sound prototype

The laser-sound prototype was developed in the laboratories of the Engler-Bunte-Institute (EBI) of the Karlsruhe Institute of Technology (KIT) [10][11][12]. The schematic diagram of the transducer prototype is shown Fig. 6.2, while photographs of the real experimental platform are shown in are shown in Fig. 6.3. Two distinct ΣΔ-based implementations of the prototype were tested:

a. 1-bit (2-level) implementation
b. 1.5-bit (3-level) implementation

The 1-bit implementation only requires pulse density control [13][14][15], which can be implemented as a pulse / no-pulse scheme through the laser triggering mechanism, without optical amplitude control. In this respect, a train of acoustic pulses with identical pressure profiles is generated, where the audio information is exclusively encoded in the variations of the pulse density. In the 3-level ΣΔ implementation, apart from the pulse / no-pulse scheme, two distinct optical pulse energies are required to transcode the three acoustic pressure levels, namely zero pressure, maximum pressure and half pressure [13][14]. For this purpose, each pulse emitted by the laser is initially directed into a polarizer (P1) which cleans the laser beam from unpolarized components by only allowing the horizontally polarized light to pass through. Then, a quarter wave plate ensures that the light entering the Pockels cell is circularly polarized. At the exit of the cell, the pulse polarization is altered to either linear, circular or elliptical, depending on the amplitude of the applied voltage V_p. Finally, the pulse is directed into a second polarizer (P2) allowing the vertical polarization component to pass, while blocking the horizontal component. As a result, the amount of light transmitted through the second polarizer depends on the light polarization at the exit of the Pockels cell which, in turn, depends on the voltage applied on the Pockels cell. In the presented setup, a full-scale negative voltage $V_{\mathrm{p}} = -V_{\max}$ leads to a pulse block, while a full-scale positive voltage $V_{\mathrm{p}} = +V_{\max}$ leads to the transmission of the full optical energy of the pulse. Finally, a zero voltage $V_p = 0$ leads to the transmission of 50% of the optical energy. This approach was chosen in order to reduce the maximum applied voltage to the non-linear crystal [10][11].

For the 3-level ΣΔ implementation presented here, these three different optical energy levels are sufficient while, for n-bit implementations, 2^n voltage levels are required and thus intermediate voltages within the range $V_{\mathrm{p}} \in (-V_{\max}, +V_{\max})$ must be selected. For such multilevel ΣΔ coding, the fidelity of the

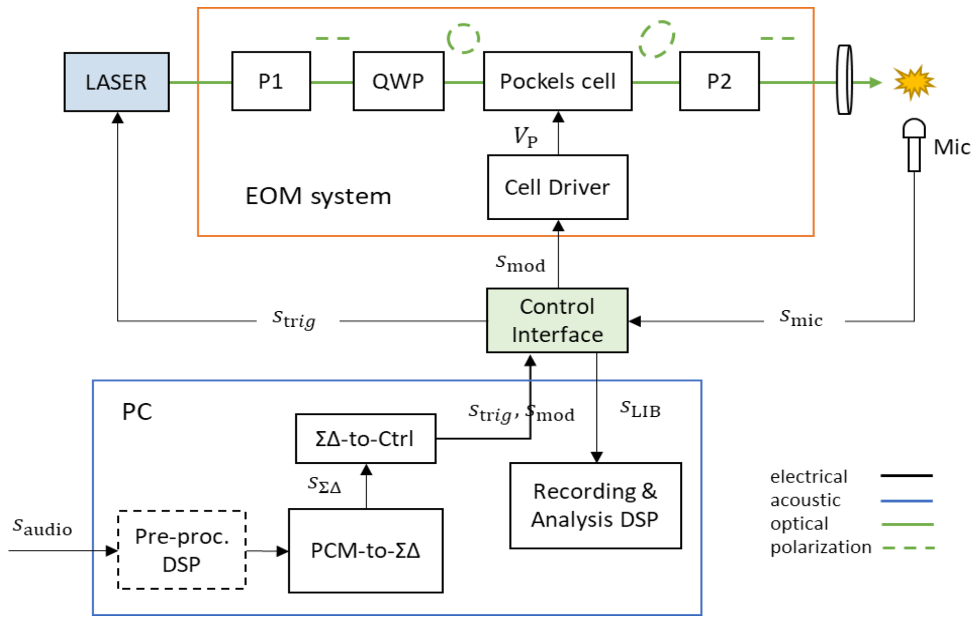

Fig. 6.2: Schematic diagram of the optoacoustic transducer prototype.

sound reproduction is susceptible to the accuracy of the reproduced pulse-to-pulse pressure amplitude, since the in-band frequency content of the generated acoustic ΣΔ stream depends on the acoustic pressure of each individual pulse. It is well known that the relation between acoustic pressure and optical energy is non-linear [16][17]; if this fact is neglected, the demodulated sound wave will potentially contain perceptible distortion in the band of interest. Hence, initial calibration is required for each particular setup, in order for the appropriate driving voltage levels to be selected to achieve precise reproduction of the pulse-to-pulse acoustic pressure levels. Nevertheless, since this aspect is not critical for the 3-level and 3-level implementations, the calibration process is not further discussed here.

Regarding the hardware components of the system, an Nd:YAG laser (EdgeWave, IS 200-2-L [19]), capable of emitting 532 nm pulses of ~ 9 mJ energy and ~10ns duration at a repetition rate of up to 8 kHz. For the optical amplitude modulation, a high damage threshold Pockels cell was used (BBO-4-40-AR532 double BBO crystal, EM500, Leysop [20]), driven by a high-voltage generator (HVG) (M2500, Leysop, [21][20]) with a full-amplitude frequency response of over 250 kHz and rise/fall times below 600 ns. An indicative test of the pulse amplitude modulation system for sine wave modulation of the optical pulses is shown in Fig. 6.4. With these specifications, the used EOM system could modulate the transmitted optical pulses at sufficiently high repetition frequencies to cover the entire audible range and will be used in the future for a full-range transduction prototype.

Finally, to achieve maximum optical-to-acoustic transduction, the pulses were tightly focused by a 75 mm lens. Focusing was done on two different target media:

a. ambient air
b. metal plates

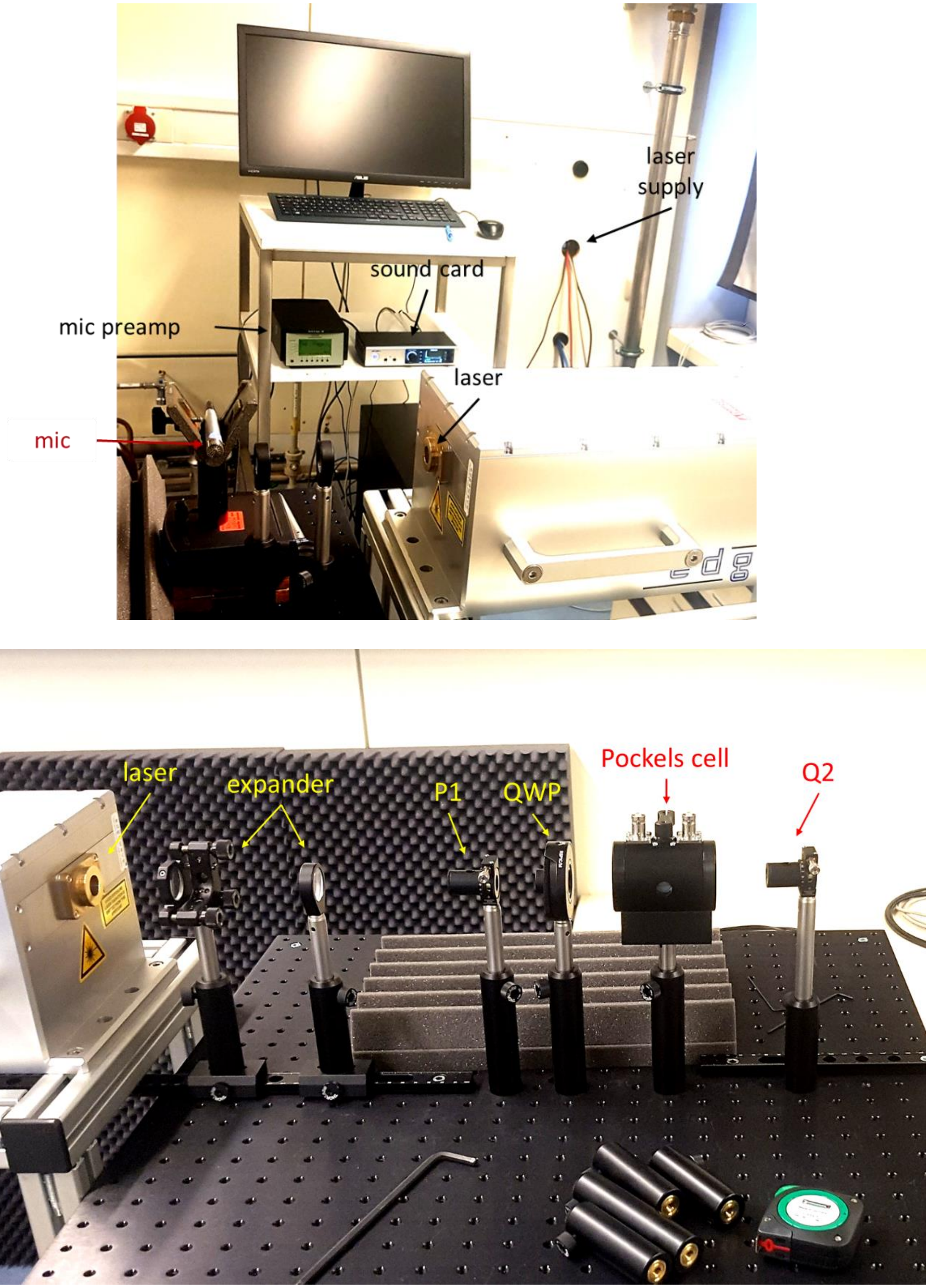

Fig. 6.3: Photographs of the optoacoustic transducer prototype a) driving audio interface and sound recording setup for the 1-bit ΣΔ implementation and b) optical setup for laser pulse amplitude modulation in the 3-level implementation.

which were placed at a distance of approximately 2 meters from the laser unit. The use of metal plates was necessary due to the limitations in the available optical energy of the laser unit, which allowed for optical intensities only marginally above the breakdown threshold of the air at the required repetition rates [19]. However, since the pulses need to pass through the EOM system, the remaining optical intensity was insufficient for breakdown in air, while it was sufficient for ablation on metal plates. Thus, the 1-bit ΣΔ implementation was evaluated for LIB directly in the air, while the 3-level ΣΔ implementation requiring pulse amplitude control, was tested for laser ablation on metal plates.

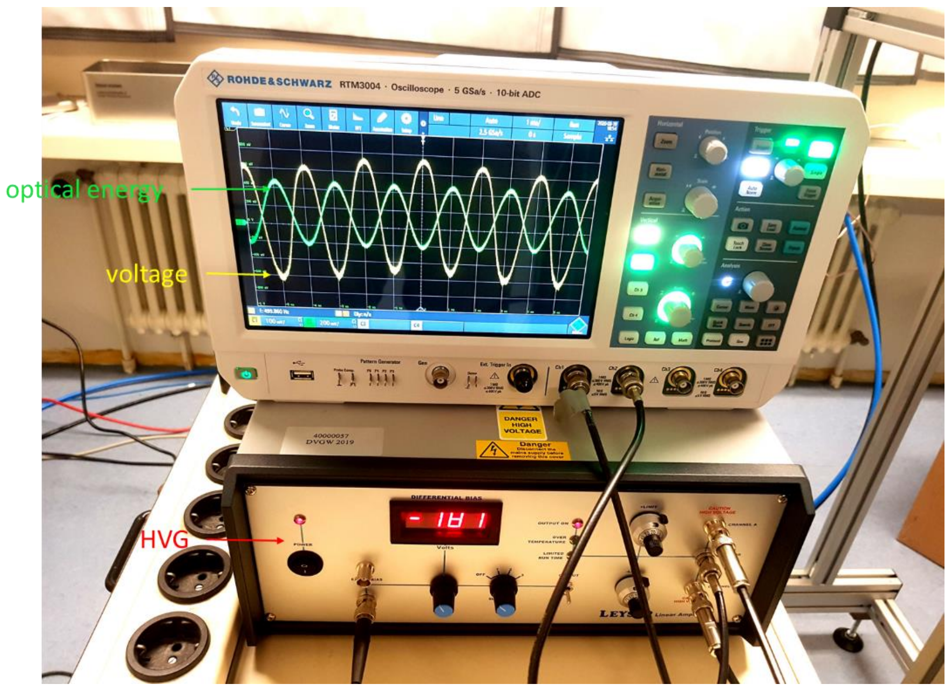

Fig. 6.4: Photograph from the test of the pulse amplitude modulation system, showing the high voltage generator, the modulating electric signal s_{mod} (voltage) and the output optical energy.

6.3 Signal processing methods

6.3.1 Audio signal modulation

The signal processing chain for the derivation of the control signals starts with a 16-bit PCM audio signal, which is upsampled (oversampled) by a factor of L and digitally low-pass filtered to suppress the spectral content above the in-band range, leading to the signal $s_{\mathrm{PCM,L}}$. The signal $s_{\mathrm{PCM,L}}$ is then converted into a ΣΔ stream by a 1st-order ΣΔ modulator, producing the signal $s_{\Sigma\Delta}$. Such a signal processing chain is depicted in Fig. 6.5. If the input is an analog signal, analog-to-digital conversion with an oversampling factor of R

has to be carried out before low-pass filtering. The rest of the process differs for 1-bit and multi-bit implementations and is presented separately.

6.3.1.1 Single-bit ΣΔ implementation

The process for generating s_{trig} from the ΣΔ stream is identical to the process used for the computational model (see subsection 6.4), with the only difference that the trigger signal consists of rectangular pulses instead of N-pulses. The characteristics of the laser trigger signal s_{trig}, particularly the pulse rise / fall times t_{rise} and t_{fall}, the total pulse duration t_{rect} and the minimum time interval between two consecutive pulses are dictated by the specifications of the laser. The position of each trigger pulse is provided by the $s_{\Sigma\Delta}$ bitstream, where each "one" denotes a "pulse" while a "zero" denotes a "no-pulse.

6.3.1.2 Multilevel ΣΔ implementations

Similarly to the 1-bit implementation, a multi-level implementation requires an optical pulse to be emitted by the laser for each non-zero signal level. However, the $s_{\Sigma\Delta}$ signal contains not only zeros and ones, but also intermediate levels with amplitudes that depend on the number of the encoding bits. For n bits, there are $2^n - 2$ intermediate levels and two consecutive levels differ by $\frac{1}{2^n-1}$. Moreover, the electro-optic modulator must be driven synchronously with the laser trigger in order to appropriately adapt the transmitted optical energy to the desired amplitude. The driving signal s_{mod} of the modulation is a PCM signal derived from the $s_{\Sigma\Delta}$ stream by quantization with resolution n. The resulting signal s_{mod} is delivered as a voltage $V_{\mathrm{mod}} \in [-2.5V, +2.5V]$ to the input of the Pockels cell driver.

6.4 Computational model

The computational model takes as inputs the output signal $s_{\Sigma\Delta}(n)$ of the ΣΔ modulator and the N-pulse signal $s'_{\mathrm{p}}(n)$ and gives as output the LIB pulse stream s_{LIB} and the in-band signal s^{R}_{audio}, as demodulated by low-pass filtering [10]. The model effectively describes the s_{LIB} signal as a ΣΔ stream where the impulses are substituted by laser generated N-pulses. Since the output of a regular digital ΣΔ modulator is a stream of impulses [13], the ΣΔ stream can be written as:

$$s_{\Sigma\Delta}(n) = \sum_{i=1}^{N_\delta} \delta(n - n_i) \tag{6.1}$$

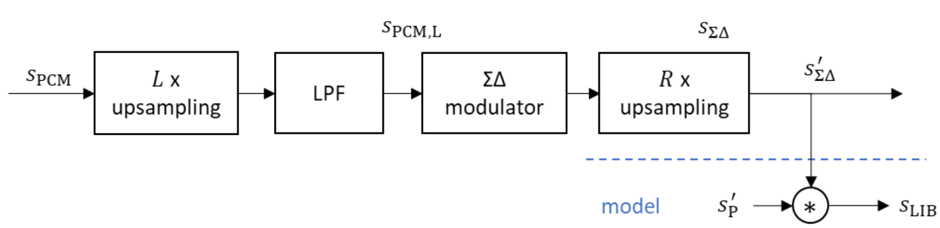

Fig. 6.5: Signal processing steps for the production of the reconstructed signals.

where $\delta(\cdot)$ is the Kronecker delta function, n_i is the time index of the i_{th} delta and N_δ is the total number of impulses in the modulated signal. Now, to substitute the delta functions with N-pulses, $s_{\Sigma\Delta}(n)$ needs to be convolved with the time profile s_{p} of the N-pulse [16][26]:

$$s'_{\mathrm{LIB}}(n) = s_{\Sigma\Delta}(n) * s'_{\mathrm{p}}(n) = \sum_{i=1}^{N_\delta} \delta(n - n_i) * s'_{\mathrm{p}}(n) \tag{6.2}$$

which gives:

$$s'_{\mathrm{LIB}}(n) = s_{\Sigma\Delta}(n) * s'_{\mathrm{p}}(n) = \frac{A}{N_{\mathrm{p}}} \cdot \left(\sum_{i=1}^{N_\delta} \delta(n - n_i) \right) * \Big(n \cdot \big(u(n + N_{\mathrm{p}}) - u(n - N_{\mathrm{p}}) \big) \Big) \tag{6.3}$$

where N_p is the length in samples of the N-pulse and $u(\cdot)$ is the unit step function. Equation (6.3) constitutes a time-domain description of the LIB acoustic pulse stream; however, it does not provide significant insight to the characteristics of the sound generated by the laser-sound system and it is more convenient to inspect the signal $s'_{\mathrm{LIB}}(n)$ in the frequency domain.

In Chapter 3, the mathematical description of a 1st-order ΣΔ modulator in the frequency domain was presented. It was shown that the frequency response of a 1st-order modulator can be written as [13]:

$$S_{\Sigma\Delta}(k) = S_{\mathrm{audio}}(k) + \mathrm{NTF}(k) \cdot E(k) \tag{6.4}$$

Hence, the DFT spectrum of the LIB pulse stream of Eq. (6.3) is the result of the multiplication between the frequency response of the modulator and the frequency spectrum of the N-pulse:

$$S'_{\mathrm{LIB}}(k) = S_{\Sigma\Delta}(k) \cdot S'_{\mathrm{p}}(k)$$

which leads to:

$$S'_{\mathrm{LIB}}(k) = S'_{\mathrm{p}}(k) \cdot S_{\mathrm{audio}}(k) + S'_{\mathrm{p}}(k) \cdot \mathrm{NTF}(k) \cdot E(k) \tag{6.5}$$

The $S'_{\mathrm{p}}(k)$ exhibits a 1st-order high-pass profile in the in-band range (see Chapter 3), and thus, the spectral magnitude of the linearized signal transfer function for the laser-audio system becomes:

$$|\mathrm{STF}_{\mathrm{LIB}}(k)| = |S'_{\mathrm{p}}(k)| \sim k \tag{6.6}$$

Accordingly, the linearized noise transfer function becomes:

$$|\mathrm{NTF}_{\mathrm{LIB}}(k)| = |S'_{\mathrm{p}}(k)| \cdot |\mathrm{NTF}(k)| \sim k^2 \tag{6.7}$$

which is a 2nd-order high-pass profile. Finally, the normalized frequency response of the laser-sound system can be written in terms of the spectrum $S_{\mathrm{audio}}(k)$ of the input signal as:

$$S'_{\mathrm{LIB}}(k) = k \cdot S_{\mathrm{audio}}(k) + k^2 \cdot E(k) \tag{6.8}$$

As shown in the next Results section, Eq. (6.6) - (6.8) are clearly verified by the simulated and measured signals.

6.5 Evaluation of the laser-sound prototype

6.5.1 Methodology

To demonstrate the functionality of the laser-sound optoacoustic transducer, systematic measurements of test and real acoustic signals reproduced by the prototype system were carried out and are compared with the predictions of the developed mathematical model. Fig. 6.6 outlines the experimental and modeling procedures for sound generation in ambient air. The input signal $s_{\text{audio}}(n)$, with n the discrete-time index, is typically obtained from a digital audio file and is directed into the modulator, where it is transformed into a ΣΔ bitstream. The modulator output $s_{\Sigma\Delta}(n)$ is used both to control the laser emission and as input to the computational model. In the physical system, the optical pulses are focused in the air causing breakdown and generating acoustic pulse trains, which are consequently captured and recorded by a microphone and data acquisition system ($s_{\text{mic}}(n)$ signal). The measured signals are post-processed in order to reduce measurement artefacts and noise, leading to the signal $s_{\text{LIB}}(n)$. The frequency spectra $S_{\text{LIB}}(k)$ of the reproduced acoustic pulse streams are obtained here via Discrete Fourier Transform (DFT), where k is the discrete frequency index. Moreover, single acoustic pulses $s_{\text{p}}(n)$ are captured and analyzed in order to generate the signal model $s'_{\text{p}}(n)$ of the acoustic N-pulse. The signal $s'_{\text{p}}(n)$ is used as an the second input to the computational model, which produces the simulated laser-generated acoustic signals $s'_{\text{LIB}}(n)$ and their respective DFT representation $S'_{\text{LIB}}(k)$. Finally, the signals $s_{\text{LIB}}(n)$ and $s'_{\text{LIB}}(n)$ are low-pass filtered and resampled to the effective bandwidth of the system, producing the reconstructed audio signals $s^R_{\text{audio}}(n)$. The signals $s^R_{\text{audio}}(n)$ are used for unofficial aural evaluations of the reproduced audio signals.

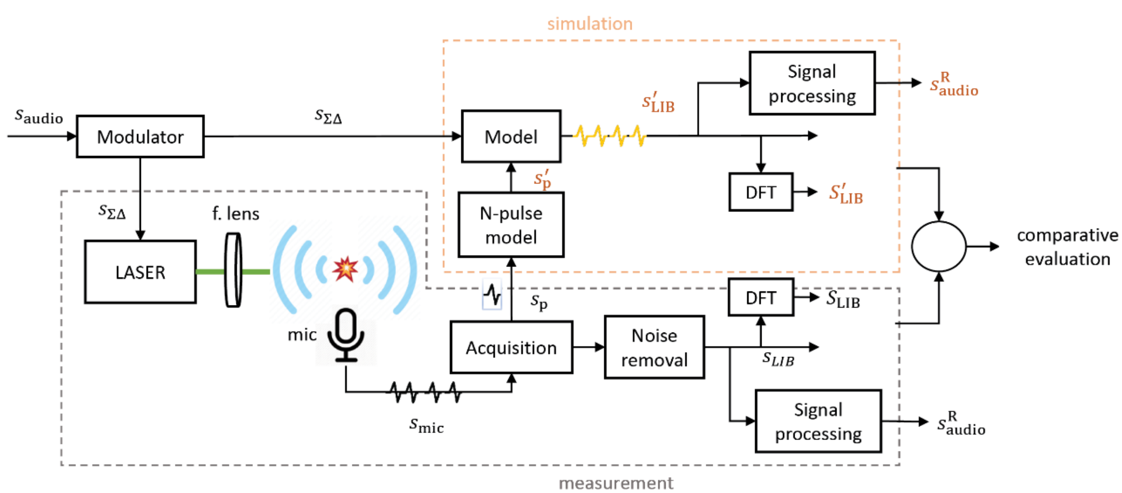

Fig. 6.6: Methodology block diagram for the experimental and computational evaluation of the laser-audio transducer prototype.

6.5.2 Experiments

In the experimental setup, the parameters and characteristics of the 1-bit ΣΔ modulation were largely dictated by the specifications of the laser system that was available for the implementation of the transducer prototype. The laser system allowed for a maximum optical pulse repetition rate of 20kHz, however, a repetition rate $f_{\text{laser}} = 4\text{kHz}$ was adopted for most of the experiments since, for rates higher than 4kHz, the optical energy dropped below the breakdown threshold and some optical pulses did not cause air breakdown, leading to "missing pulses". In such low repetition rates, the pulse-to-pulse time distance ($t_{\text{ptp}} \geq$ 250μs) is sufficiently large for the plasma to relax and the interaction volume to cool down. The plasma lifetime, as well as the duration of the thermoelastic expansion and collapse of the interaction volume, depend on the laser radiation parameters, such as pulse duration, wavelength, energy and focusing conditions. For identical laser parameters it has been observed that the plasma relaxes within a few tens of nanoseconds, while the full thermoelastic process relaxes within a few up to a few tens of microseconds [5][6]. As a result, each laser pulse of the ΣΔ pulse train is focused in neutral air of identical temperature and density, a fact that manifests also in the high repeatability of the acoustic pulses.

Due to the restriction in the available repetition rate, and in order to effectively demonstrate the proof-of-concept functionality of the system, a ΣΔ oversampling factor of $L = 2$ was adopted, together with a 1$^{\text{st}}$-order noise shaping. Consequently, the original sampling frequency of the input signals was set to $f_s = 2\text{kHz}$ (f_{laser}/L) allowing for an effective bandwidth of up to 1kHz according to the Nyquist criterion: $f_{\text{audio}} \in [20\text{Hz}, 1\text{kHz}]$. The Signal to Quantization Noise Ratio (SQNR) of such a 1$^{\text{st}}$-order 1-bit modulator is approximately 21 dB while for the 1.5-bit (3-level) modulator it is 24 dB [14]. However, in the 3-level implementation the SNR of the measured signal is further compromised by the use of a rotating metal target, as the one shown in Fig. 6.7. Although such restrictions compromise the frequency range and quality of the signals, the results clearly illustrate the principles introduced in this work and are adequate for validating the computational model. For this purpose, the experimental and computational results for a single sine wave input are presented and compared in the next subsections. The microphone was placed at a distance of 5 cm from the LIB breakdown spot. The microphone signal was digitized by the sound card (see Fig. 6.3) with a sampling frequency $f_s = 384\text{ kHz}$ and 24-bit resolution and recorded using the Audacity audio software [22] enhanced with the Aurora plugin [23].

6.5.3 Measurements processing

For the acoustic evaluation of the system by means of measured and simulated audio signals, provided as supplementary material, low-pass filtering was used to limit the frequency spectrum of the signals in the band-of-interest. Particularly, the acoustic pulse trains $s_{\text{LIB}}(n)$ and $s'_{\text{LIB}}(n)$ were filtered by an anti-

Fig. 6.7: Photograph of the metal plate used for the evaluation of the 3-level implementation of the transducer prototype based on laser ablation. The grooves formed by the material removal are apparent.

aliasing low-pass filter $s_{\mathrm{filt}}(n)$, with cut-off frequency equal to the Nyquist frequency of the original input signal $f_{\mathrm{filt}} = \frac{f_{\mathrm{s}}}{2}$. The band-limited signal was downsampled by a factor M to a resulting frequency f_{s} and the reconstructed audio signal was produced:

$$s^{\mathrm{R}}_{\mathrm{audio}}(n) = (s_{\mathrm{LIB}} * s_{\mathrm{filt}})(nM) \tag{6.9}$$

Additionally, the speech and music audio signals were low-pass filtered in the inband range to equalize the high-pass profile of the system's response (see Eq. (6.8)). In a full-specifications high-SQNR laser-sound system, the equalization can take place by preprocessing the input signal s_{audio}, as shown in Section 6.7.2. Finally, the signal processing steps taken for the audio samples of the supplementary material are shown in Fig. 6.8.

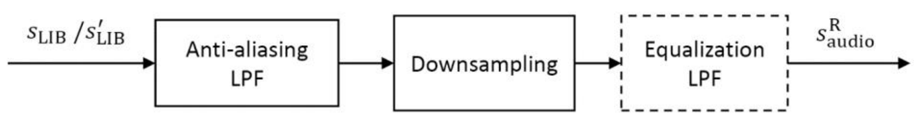

Fig. 6.8: Signal processing steps for the production of the reconstructed signals.

6.6 Results

For the evaluations, the following test signals were used:

1. single sine waves at central octave band frequencies from 31.5 Hz to 500 Hz
2. band limited sine sweep signals
3. excerpt from female speech [24] and music

Sine wave signals are commonly used as stimuli for the evaluation of acoustic systems and transducers [25] while they are also suitable for evaluating low-SQNR digital modulations, as they concentrate all of their energy in one frequency. The bandwidth of the prototype transducer allowed for reproduction of sine waves at the octave band central frequencies 31.5, 63, 125, 250 and 500 Hz. Moreover, sine sweep signals are commonly used for the evaluation of a system's impulse and frequency response, as they excite the system throughout the entire in-band range [27]. By deconvolution of the measured response to the sine sweep signal, the system's impulse response is obtained, from which, the frequency response is calculated via DFT. Here, logarithmic sine sweeps with a frequency range from 20 Hz to 1 kHz were used. The system's response was also evaluated for a female speech and a music sample. Due to the complexity of the frequency-domain profile of these signals, no related diagrams are shown here. The reproduction results are available for auditory evaluation at http://audiogroup.ece.upatras.gr/tools/laser_sound.php.

Finally, the simulations supporting the measurements were based on measured spectral profiles of the N-waves generated by laser-induced breakdown in the air and laser ablation on metal targets, accoriding to Eq. (6.5). The used spectral profiles are shown in Fig. 6.9 a) and b) respectively.

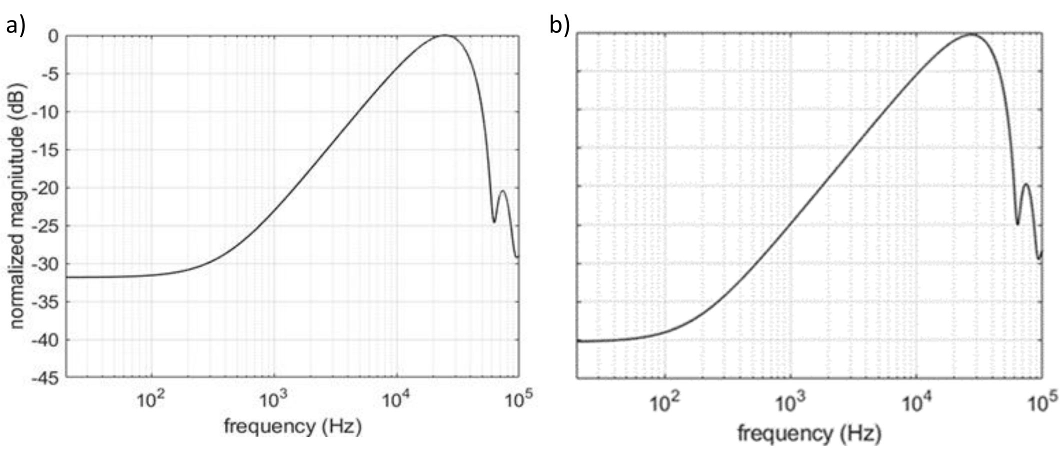

Fig. 6.9: Frequency spectrum of the acoustic pulses generated by a) laser-induced breakdown and b) laser ablation of a metal plate, measured at a bandwidth 20 Hz to 20 kHz and windowed in the time domain with a 47 μs symmetric Tukey window.

6.6.1 Single-bit ΣΔ tests in ambient air

6.6.1.1 Time and frequency profile of reporoduced sine wave

In the previous section, it was shown that the 1-bit ΣΔ approach is the simplest implementation, as it essentially requires only a focusing lens and a triggering mechanism. The absence of a pulse amplitude modulation system minimizes optical energy losses along the pulse propagation path, allowing for direct optoacoustic transduction in the air with the particular laser unit. Fig. 6.10 a) shows a part of a sinusoidal signal with frequency $f_{\text{sine}} = 125\text{ Hz}$, superimposed on its ΣΔ representation that is produced after the modulator stage. This ideal ΣΔ modulated sine wave is compared with the respective signal $s'_{\mathrm{LIB}}(n)$ as evaluated by the computational model (Fig. 6.10 b)) and the measured signal $s_{\mathrm{LIB}}(n)$ that is generated by the prototype system (Fig. 6.10 c)). From comparison of the Fig. 6.10 a)-c) it becomes apparent that the modulated, simulated and measured signals all constitute the same pulse train, which proves that the laser-audio system is able to reproduce the ΣΔ pulse sequences with high accuracy, essentially replacing the rectangular ΣΔ pulses with laser-generated N-pulses.

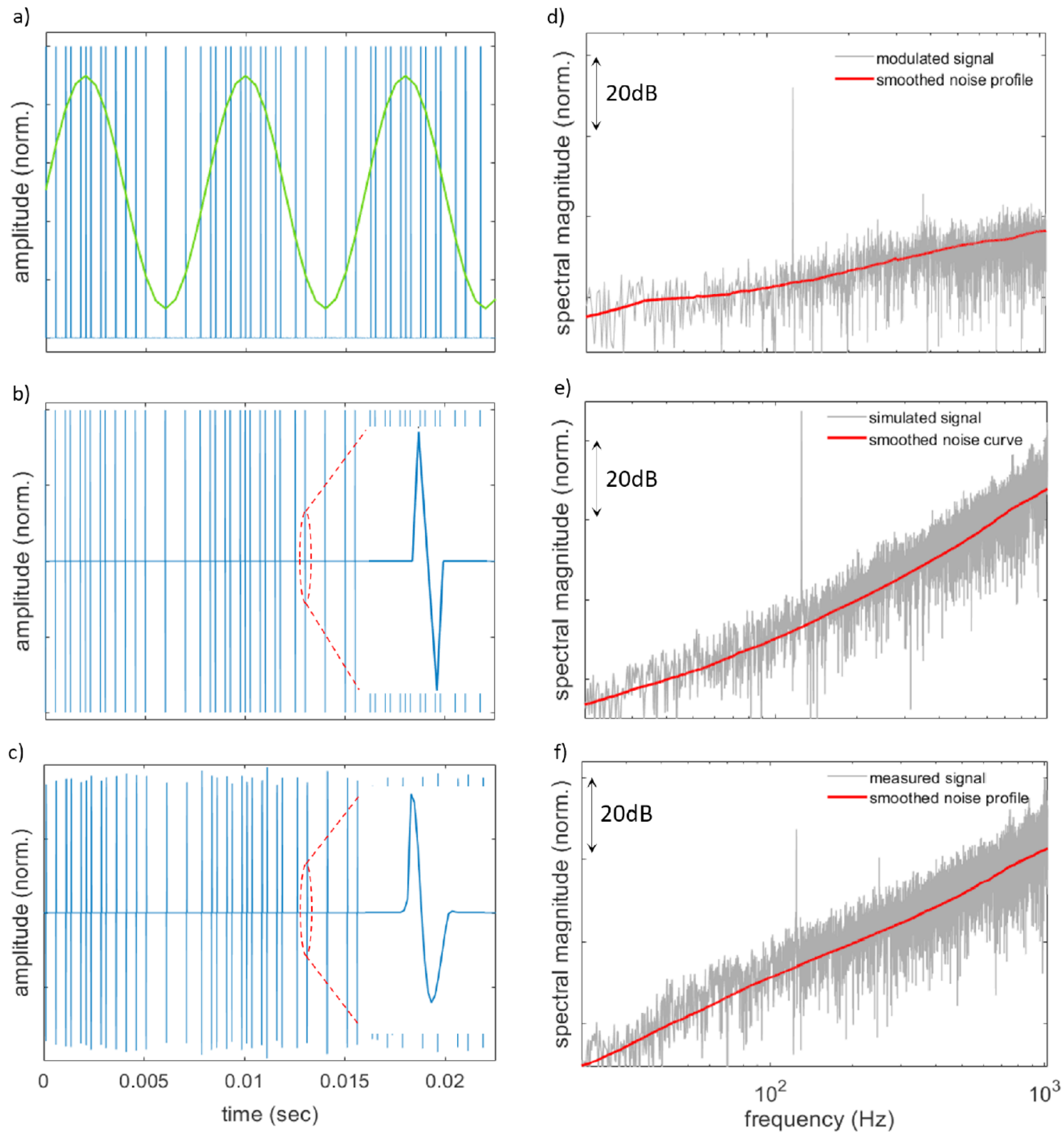

Fig. 6.10: Time-domain representations of a 125Hz sine wave signal a) encoded as a ΣΔ stream $s_{\Sigma\Delta}(n)$ of rectangular pulses, b) simulated as a LIB pulse stream $s'_{\mathrm{LIB}}(n)$ using the modeled ideal N-pulse signal $s'_{\mathrm{p}}(n)$ and c) reproduced from the laser-audio system $s_{\mathrm{LIB}}(n)$, d-e) frequency-domain representations of the signals within the inband range $[20\mathrm{Hz}, 1\mathrm{kHz}]$, as obtained via DFT.

Fig. 6.10 d)-f) show the corresponding frequency spectra of the signals as obtained via DFT within the inband frequency range. In the spectrum $S_{\Sigma\Delta}(k)$ of the ideal ΣΔ signal (Fig. 6.10 d)), the sine wave frequency is prominent at 125 Hz, approximately 35 dB higher than the noise floor in the neighboring frequencies while the characteristic noise shaping of the modulator can be observed as a 1st-order high-pass slope of the quantization noise floor. Fig. 6.10 e) shows the spectrum $S'_{\mathrm{LIB}}(k)$ of the simulated signal $s'_{\mathrm{LIB}}(n)$, as obtained by multiplying $S_{\Sigma\Delta}(k)$ by the spectrum $S'_{\mathrm{p}}(k)$ of a single modeled N-pulse. From Fig. 6.10 e) it can be seen that the spectral magnitude of the sine wave frequency is preserved, while the noise floor of $S'_{\mathrm{LIB}}(k)$ has a second-order high-pass profile as a result of the combined effect of the ΣΔ noise shaping and the spectrum $S'_{\mathrm{p}}(k)$ of the N-pulse (see Eq. (6.5)). The same spectral profile also manifests in the spectrum $S_{\mathrm{LIB}}(k)$ of the measured signal shown in Fig. 6.10 f), but here the noise floor is raised by approximately 10 dB, due to the acoustic noise introduced in the experiment. Also, in $S_{\mathrm{LIB}}(k)$ the second harmonic of the sine wave frequency can be seen in $S_{\mathrm{LIB}}(k)$, which indicates a potential mild non-linearity in the reproduction chain.

6.6.1.2 Discrete sine waves

Fig. 6.11 a) and b) show the overlaid frequency spectra of the measured and simulated sine waves at octave band central frequencies from 31.5 Hz to 500 Hz. For the sine wave encoding, pole optimization was used in the ΣΔ modulator [13], through which the impact of the noise shaper in the in-band range is minimized and an almost flat in-band profile of the noise floor is obtained (see also Chapter 3). The discrete sine signals were reproduced and recorded separately but are superimposed here on the same figure for convenience. It can be seen that the laser-sound system reproduces the frequencies of the sine wave inputs with high accuracy, while any differences in the magnitudes result from the spectral profile of the LIB pulse, as can be directly evaluated from Eq. (6.5). Moreover, the spectral profile of the noise

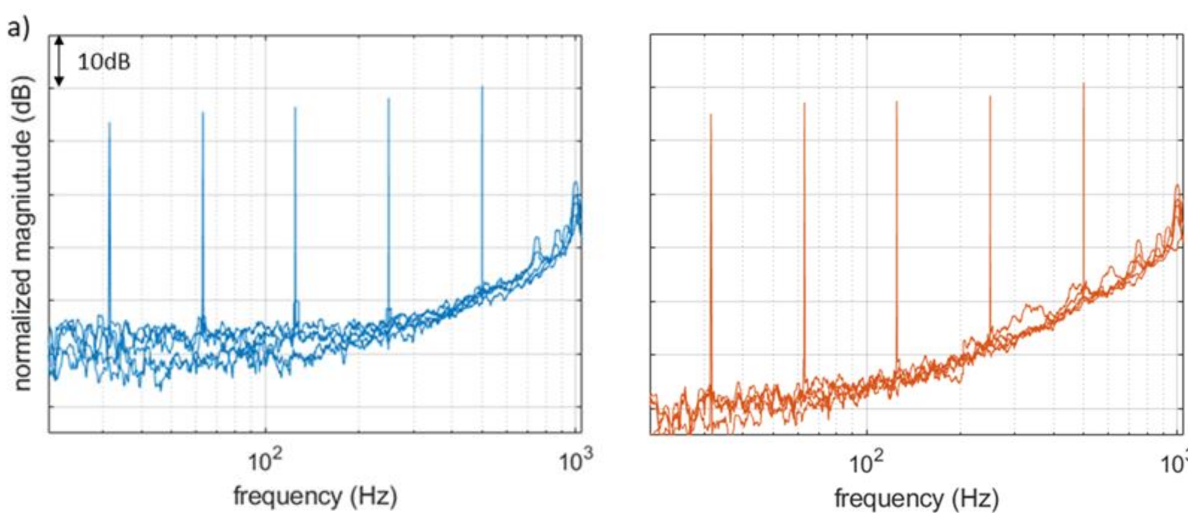

Fig. 6.11: Frequency spectra of successive sine wave signals with frequencies 31.5, 63, 125, 250 and 500 Hz, reproduced by the 1-bit ΣΔ laser-sound prototype, a) measured and b) simulated results.

floor also follows the predictions of Eq. (6.5). In the simulations of Fig. 6.11 b), the noise originates exclusively from the quantization introduced by the ΣΔ modulation and thus follows the spectral profile $S_p(k)$ of the pulse. In the measurements of Fig. 6.11 a), apart from the quantization noise, environmental acoustic noise is also present, raising the noise floor in the lower frequencies by approximately 10 dB. Nevertheless, above 250 Hz, the measurement and simulation noise floor coincide.

6.6.1.3 Impulse and frequency response

Fig. 6.12 a) shows the comparative plots of the simulated and experimentally measured impulse responses of the complete laser-sound transduction system, obtained via bandlimited swept sine excitation. As expected from Eq. (6.5), the system's impulse response in the in-band range effectively is the LIB N-wave, filtered by a 1 kHz low-pass filter, due to the frequency limitations imposed by the laser repetition rate. The good agreement between the simulations and measurements indicates that the behavior of the real system can be accurately predicted by the computation model, potentially also for the extended full audio bandwidth [10][11]. The comparative measured and simulated frequency responses of the system shown in Fig. 6.12 b) are also in good agreement, although some low-frequency additive acoustic noise is present in the measurements.

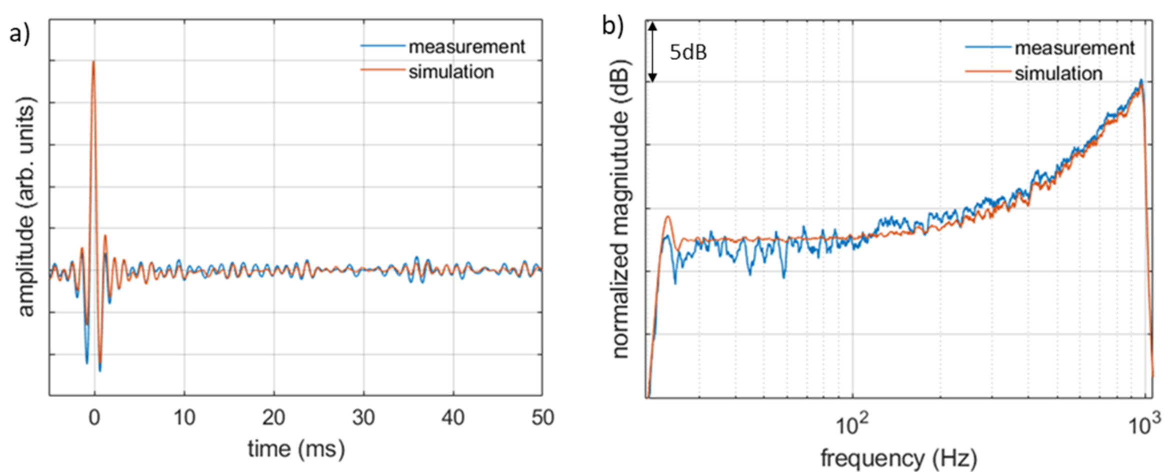

Fig. 6.12: Comparative measured and simulated responses of the 1-bit ΣΔ laser-sound prototype a) impulse response and b) frequency response. The sine sweep excitation was limited in the range 20 Hz to 1 kHz.

6.6.2 Three-level ΣΔ test signals

For the 3-level ΣΔ modulation scheme, the optical energy of the laser-sound prototype was insufficient to generate air plasma, since the rather small but non-negligible losses in the electro-optical modulation system reduced the already marginal pulse energy to a level below the breakdown threshold. For this reason, the experiments of the 3-level implementation were carried out using metal plates as target materials.

6.6.2.1 Discrete sine waves in octave frequencies

Fig. 6.13 a) and b) show the frequency spectra of the measured and simulated sine waves, respectively. Again, the laser-sound system reproduces the frequencies of the sine wave inputs with high accuracy. Here, the measurement noise appears 20 dB higher than in the simulations, which can be attributed to the additional noise produced by the etching of the metal plate during ablation, but also possibly due to secondary low-frequency acoustic radiation due to vibrations of the plate.

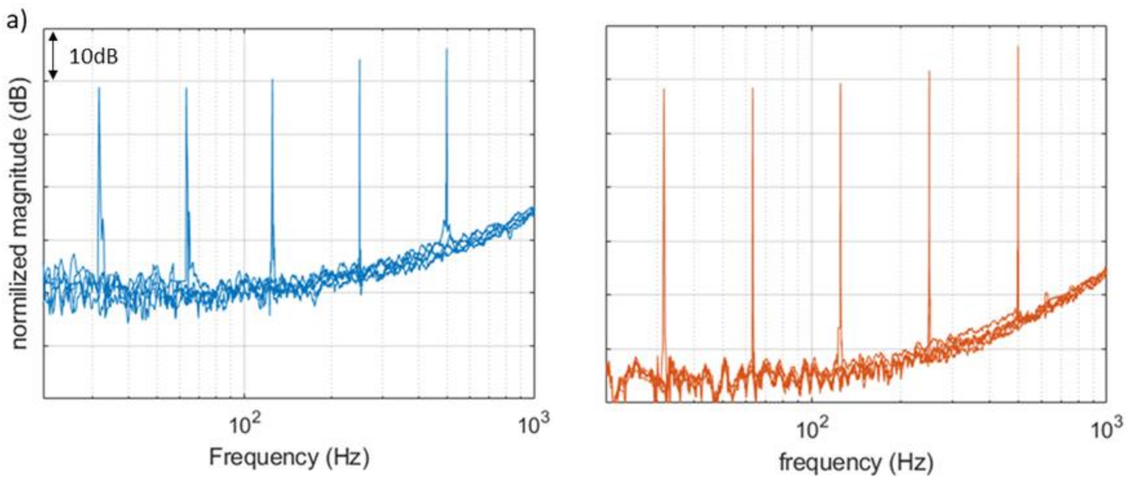

Fig. 6.13: a) Measured and b) simulated frequency spectra of sine wave signals with frequencies 31.5, 63, 125, 250 and 500 Hz reproduced by the 3-level ΣΔ laser-sound prototype on a metal plate.

6.6.2.2 Impulse and frequency response

Fig. 6.14 presents the impulse and frequency response of the 3-level laser-sound prototype system, where, as with the 1-bit ΣΔ system, a good agreement between the simulations and the measurements can be observed, except for a ~4 dB mismatch in the high frequencies. This can be attributed to the profile s_p' of the LIB acoustic pulse used for the simulation of the ablation-generated sound. Nevertheless, despite potential differences in the spectrum of laser-generated N-waves in the low frequencies, all the acoustic pulses exhibit the characteristic $S_p(k) \sim k$ spectral profile above 1 kHz [6][7][16]. Moreover, sound from vibrations of the metal plates could potentially contribute to the observed mismatch. To account for the contribution of the sound due to vibrations, it is necessary to estimate the mechanical response of such metal plates to the laser radiation. Such a task is left for the future and is not discussed further here.

6.7 Simulation of the ideal optoacoustic transducer

Despite the technical limitations of the presented experiments, the properties of the prototype system were found to be controllable, well-defined, and in a good agreement with the predictions of a linear

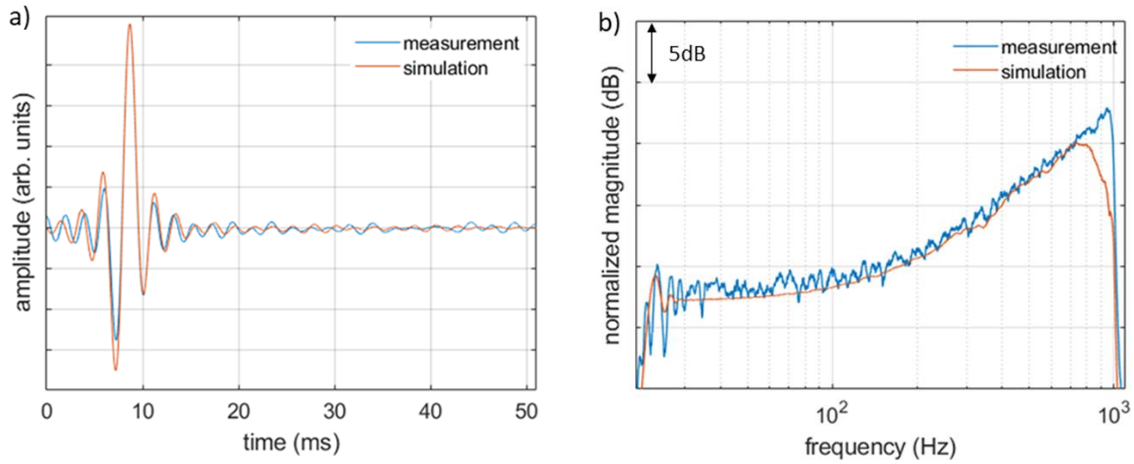

Fig. 6.14: Comparative measured and simulated response of the 3-level ΣΔ laser-sound prototype a) impulse response and b) frequency response. The sine sweep excitation was limited in the range 20Hz-1kHz.

computational model. The accuracy of the predicted results verifies that this computational model can be used for the evaluation of ΣΔ-based laser-sound systems in terms of their characteristics, and particularly, the profile s_p' of a single laser-generated acoustic pulse and the ΣΔ modulator implementation. This is demonstrated here by the use of the model to evaluate the performance of an ideal ΣΔ-based laser-sound system with an in-band range extending along the entire audible spectrum. The main physical limitation of such a system constitutes the duration of the cooldown process of the excited medium, which imposes restrictions on the permitted excitation frequency. In ambient air, typical cooldown times range from a couple of microseconds up to several tens of microseconds, depending on the amount of the deposited energy [5][6][16], allowing for a maximum optical excitation frequency at the same spot of several hundreds of kilohertz.

Considering these physical limits and a typical audio sampling frequency $f_s = 44.1\ \mathrm{kHz}$, an oversampling factor $R = 8$ could be employed, resulting in a laser pulse emission frequency of $352.8\ \mathrm{kHz}$. Note that, this is significantly lower than the oversampling factor used in typical 1-bit ΣΔ audio modulations, such as the Direct Stream Digital used in the Super Audio CD [28][29], which adopts an $R = 64$ and leads to a maximum pulse repetition frequency of $2.8224\ \mathrm{MHz}$. The low oversampling factor dictates for a high-order and multibit ΣΔ modulator in order to achieve a satisfactory Signal to Quantization Noise Ratio (SQNR), which is typically estimated through the formula [14]:

$$\mathrm{SQNR} = 6.02n + 3.01 \cdot \log_2 R \cdot (2L + 1) - 9.36L - 2.76 \tag{6.10}$$

where n is the number of bits and L is the modulator order. For a 6th-order, 5-bit modulator with x8 oversampling, the SQNR is approximately $88.57\ \mathrm{dB}$. However, the noise will not be uniformly distributed across the in-band range; by assuming a flat in-band quantization noise profile $E(k)$, the noise profile of the reproduced signal will exhibit a 1st-order high-pass profile due to the frequency profile of the N-pulse (see Eqs. (6.5) and (6.8)). For the entire audible range spanning approximately 10 octaves (3 decades), the noise floor at 20 kHz will be 60 dB higher than at 20 Hz.

It should be noted that, in a real system, the multi-level functionality can be achieved with high precision via the pulse amplitude control system. To account for the multi-level ΣΔ stream, Eq. (6.1) of the computational model has to be adapted as:

$$s_{\Sigma\Delta}(n) = \sum_{i=1}^{N_\delta} a_i \cdot \delta(n - n_i) \tag{6.11}$$

where $a_i \in [0,1]$ the quantized amplitude of the i_{th} ΣΔ impulse.

6.7.1 Simulation of sine wave reproduction

Fig. 6.15 shows the model's estimations on the reproduction of a 1kHz sine wave from the ideal laser-sound system. Particularly, Fig. 6.15 a) shows the DFT spectrum $S_{\Sigma\Delta}(f)$ at the output of the ΣΔ modulator; the effect of the pole optimization on the noise floor can be seen at the higher end of the in-band range, while the characteristic noise shaping profile begins at around 20 kHz and extends into the ultrasounds. Due to pole optimization, the quantization noise floor exhibits a flat spectrum in the in-band range and the normalized NTF can be written as:

$$|\mathrm{NTF}(k)| = 1, \qquad k \in [0, \frac{N_{\text{audio}}}{2}] \tag{6.12}$$

where, N_{audio} the total number of samples of the audio input signal. Moreover, Fig. 6.15 b) shows the simulated spectrum $S'_{\text{LIB}}(k)$ of the laser-generated acoustic pulse stream, where the NTF takes the predicted 1$^{\text{st}}$-order high-pass profile as a result of the multiplication by the spectral profile of the N-pulse (see Eq. (6.5) - (6.7)):

$$|\mathrm{NTF}_{\text{LIB}}(k)| \sim k, \qquad k \in [0, \frac{N_{\text{audio}}}{2}] \tag{6.13}$$

Fig. 6.15 c) shows the reconstructed time-domain signal $s^R_{\text{audio}}(n)$ which is produced by filtering of the simulated signal $s'_{\text{LIB}}(n)$ with a low-pass filter with cutoff frequency $f_{\text{filt}} = 20\,\text{kHz}$. The reconstructed signal has the time profile of a perfect sine wave, showing that the information of the input signal in the band of interest can be recovered from the laser-generated acoustic pulse train by simple low-pass filtering. It can be deduced that, in a real implementation of a laser-sound system, the required low-pass filtering with a 20 kHz cutoff frequency can be done directly by the human auditory system. Such a concept for the natural filtering of ultrasound frequencies has been successfully used in audio applications, for example in "sound from ultrasound" technologies for the generation of highly directional audio sources (see for example Audio Spotlight [30][31]).

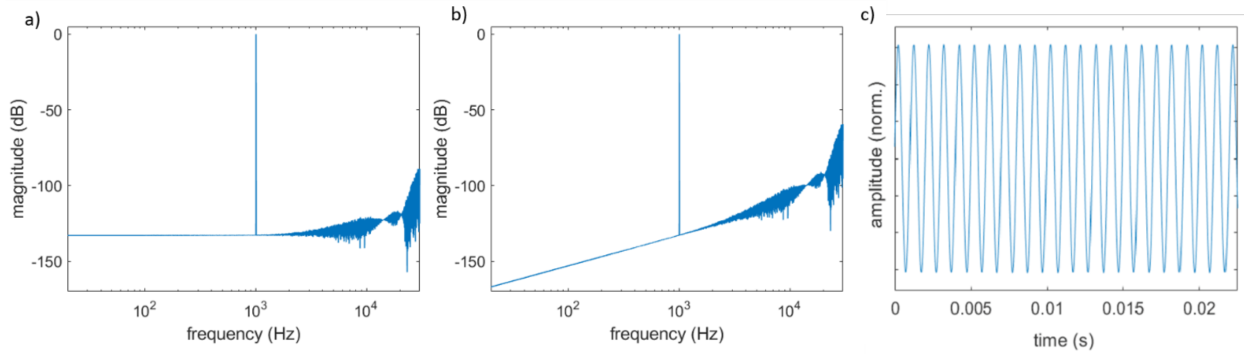

Fig. 6.15: a) $S_{\Sigma\Delta}(n)$, b) $S'_{\mathrm{LIB}}(n)$ and c) $s^{\mathrm{R}}_{\mathrm{audio}}(n)$ for a 1kHz sine wave input, simulated under consideration of an ideal optoacoustic transducer based on a state-of-the-art 160kHz pulsed laser system.

6.7.2 Frequency response equalization

A crucial characteristic of an ideal sound transducer is a flat in-band frequency response, which is expressed in terms of the system's signal transfer function as:

$$|\mathrm{STF}_{\mathrm{ideal}}(k)| = 1, \qquad k < \frac{N_{\mathrm{audio}}}{2} \tag{6.14}$$

To achieve such an STF in the in-band frequency range, the input signal needs to be filtered with the inverse filter $S_{\mathrm{inv}}(k)$ of the system's original STF, so that:

$$|\mathrm{STF}_{\mathrm{ideal}}(k)| = |\mathrm{STF}_{\mathrm{LIB}}(k)| \cdot |S_{\mathrm{inv}}(k)| = 1 \tag{6.15}$$

From Eq. (6.6) it emerges that $S_{\mathrm{inv}}(k)$ is the transfer function of a first order low-pass filter:

$$|S_{\mathrm{inv}}(k)| = \frac{1}{|S'_{\mathrm{p}}(k)|} \sim \frac{1}{k}$$

By applying such a filter on the input audio signal, the in-band frequency spectrum of the sound reproduced by the equalized laser-sound system becomes:

$$S'_{\mathrm{LIB,eq}}(k) = S_{\mathrm{audio}}(k) + E(k) \cdot S_{\mathrm{p}}(k) \tag{6.16}$$

Fig. 6.16 illustrates the simulated behavior of such an ideal laser-sound system with a 20 Hz to 20 kHz bandwidth. The frequency responses $S'_{\mathrm{LIB}}(k)$ and $S'_{\mathrm{LIB,eq}}(k)$ of the non-equalized and equalized ideal laser-sound systems are plotted along with the simulated acoustic spectrum reproduced by the equalized system for the 1 kHz sine wave input. The simulation of the system's frequency response was carried out by using as input a digital impulse signal $\delta(\cdot)$, which was consequently converted to a 5-bit ΣΔ stream and convolved with the time profile s_p' of the ideal N-wave. By comparing $S'_{\mathrm{LIB}}(k)$ with $S'_{\mathrm{LIB,eq}}(k)$, it becomes evident that the equalized system has a flat frequency response, unlike the 1$^{\mathrm{st}}$-order high-pass response of the non-equalized system, in accordance to Eq. (6.5) and (6.16), respectively. As is also evident from these equations and Fig. 6.16, the impulse response of such a system, limited to the in-band frequency range, would be identical to an LPF-corrected N-wave, or equivalently, to a triangular pulse with a duration from a few up to a few tens of microseconds. Moreover, from the simulated 1 kHz sine wave it can be seen that the noise floor of the system exhibits a 1st-order high-pass profile, as predicted by Eq. (6.16).

6.8 Estimation of the transduction efficiency

The transduction efficiency of a laser-sound system mainly depends on 3 sources of energy loss throughout the transduction chain: a) the ***electrical-to-optical*** energy conversion of the laser unit, b) the ***absorption of optical energy*** from the targeted medium and c) the ***optical-to-acoustic*** (thermal) energy conversion. To quantify the total energy losses for the presented prototype transducer and also estimate the theoretical efficiency of an ideal laser-sound transducer with optimal components and optimized working parameters, the following considerations can be done:

a) The power consumption of the used laser unit for a maximum optical output of 90W at 532nm wavelength is 1.2kW, corresponding to an efficiency $\eta_1 = 7.5\%$. The efficiency doubles for infrared pulses (1064nm). However, state of the art nanosecond or femtosecond lasers capable of fast laser-plasma excitation can achieve efficiencies of the order of $\eta_1' = 30\%$ [32].

b) The efficiency of the optical energy absorption from the air depends on optical parameters, such as the pulse duration, energy, wavelength and focusing conditions as well as on ambient parameters, mainly the humidity and temperature of the air. From measurements of the remaining optical energy after the focal spot it was found that in the presented experiments about one third of the optical pulse energy is

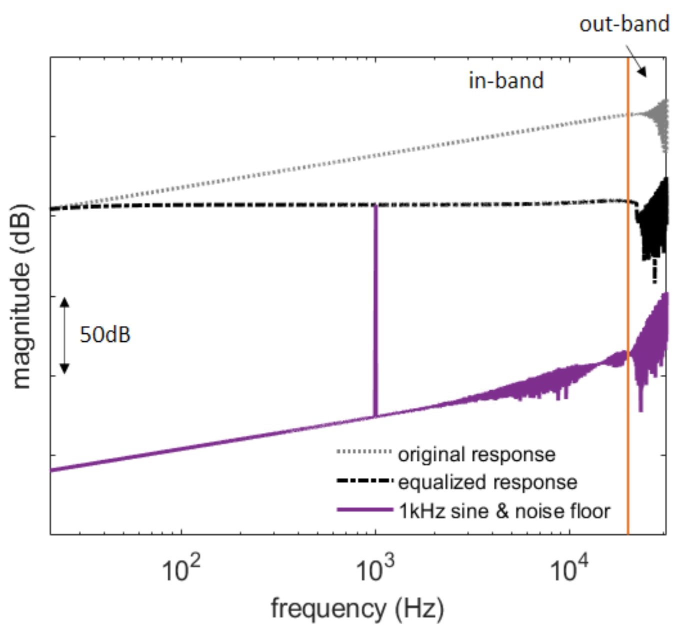

Fig. 6.16: Simulation of an ideal laser-sound system based on a 6th-order, 5-bit, x8 oversampling ΣΔ modulation with a theoretical SQNR of 88.57 dB. The equalized and non-equalized frequency responses of the system are shown, along with the simulated spectrum of the 1 kHz sine wave reproduced by the equalized system.

absorbed and thus, the efficiency of the energy absorption process is approximately $\eta_2 = 33\%$. However, as mentioned earlier, the optical intensity used here was close to the energy threshold for optical breakdown. In such low energies, the absorption efficiency is significantly lower than for energies well above the threshold. In studies with higher optical intensities [33], absorption efficiencies of more than $n'_2 = 80\%$ have been observed. Equivalent efficiencies are achieved when the laser pulses are focused on solid targets.

c) Finally, the absorbed optical energy is only partially converted into acoustical energy. This is due to losses, among others, in the form of optical and thermal radiation from the ionized volume that do not contribute to the thermoelastic expansion that generates the acoustic wave. The efficiency of this process can be estimated by calculating the total acoustic energy of a measured N-wave, according to the formula:

$$E_\mathrm{s} = \frac{4\pi r^2}{\rho_0 c} \cdot \int_0^{T_\mathrm{p}} p_\mathrm{N}^2(t) dt$$

where E_s is the total acoustic energy, ρ_0 is the air density, c is the speed of sound in air, r is the measuring distance and $p_\mathrm{N}(t)$ is the sound pressure of the N-pulse and T_p the duration of the pulse. For the typical laser parameters of the experiment in the ambient air, $T_\mathrm{p} \approx 60\ \mu\mathrm{s}$, peak pressure $p_\mathrm{max} = 25\ \mathrm{Pa}$ at $1\ m$ distance, results to $0.35\ \mathrm{mJ}$ total acoustic energy per pulse. For an $8\ \mathrm{mJ}$ pulse and 30% absorption, the absorbed energy is $E_\mathrm{a} = 2.4\ \mathrm{mJ}$, which leads to an optical-to-acoustic conversion efficiency:

$$\eta_3 = \frac{E_\mathrm{s}}{E_\mathrm{a}} = 15\%$$

which is in agreement with estimations given in [Oksanen].

By using the efficiency values corresponding to the prototype platform, we get a total transduction efficiency:

$$\eta = \eta_1 \eta_2 \eta_3 = 0.37\%$$

while by considering the improved working parameters and state-of-the-art devices, and by adopting a realistic improvement of the third efficiency parameter $\eta'_3 = 20\%$, the theoretical efficiency becomes:

$$\eta_\mathrm{imp} = 4.8\%$$

Note that, the theoretical limit of the efficiency of moving-coil electromechanical transducers is $\eta_\mathrm{em} = 4\%$ while the efficiency of common commercial transducers is $\eta_\mathrm{com} = 2\%$ [34].

6.9 Discussion

Although the physical principles of sound generation via laser-induced breakdown have been known for some time [1][2][3][4], to the best of the authors' knowledge, the laser-sound platform presented here together with the computational model, is the first functional prototype achieving laser-driven reproduction of arbitrarily complex continuous sounds without the need for a demodulation device. The functionality of the transducer was demonstrated at a proof-of-concept level (Technical Readiness Level 3) by experimental evaluation of the reproduction of sinusoidal signals, sine sweeps and typical speech and music signals. From the close agreement of the predictions of the linear model with the experimental results, it can be assumed that the ΣΔ-driven laser-sound system exhibits a linear functionality in the in-band frequency range.

Although not thoroughly addressed in the presented experimental evaluation, there is evidence that laser-driven sound sources can exhibit directional characteristics that can be potentially controlled via the laser radiation parameters. The work by Bolaños, Eskelinen, Delikaris-Manias, Pulkki et.al. [40][41] has demonstrated the possibility of using laser-induced breakdown to generate massless sound sources with arbitrary directionality by forming virtual volumetric clouds of plasma point clouds in the air. Also, the LIB sound sources can be inherently directional in the audible spectrum, depending on the geometry of the generated plasma volume, which, in turn, depends on the laser pulse duration and focusing conditions, especially for femtosecond pulse excitation where elongated plasma threads can be formed in the air [42][26][43][44][45]. Directional sound waves generated by laser excitation have also been observed on solid targets [46].

It has to be noted that, the acoustic spectrum generated by the laser-sound system extends well beyond the audible range up to the ultrasounds, due to:

a) high-frequency quantization noise from ΣΔ noise shaping and
b) strong spectral components on the laser pulse repetition frequency and its harmonics, which are typical for pulse modulation signals.

According to Eq. (6.16), the system's out-band acoustic energy originating from the ΣΔ modulation is shaped by the spectral profile of the laser-generated acoustic pulse. Also, from the mathematical expression of the N-pulse given in Eq. (6.3), it can be seen that its spectral profile only depends on its duration [6][16], with longer pulses exhibiting more energy in the low frequencies and having low energy in the ultrasounds. Hence, longer N-waves result to weaker out-band acoustic energy, without affecting the in-band spectrum.

Moreover, although imperceptible to the human ear, the high ultrasonic energy generated by the laser-sound system could impose potential hazards or limitations in real-world applications. Strong ultrasounds are known to cause distress or hearing problems to humans and animals such as dogs, cats, bats etc. [35]. However, the ultrasonic frequencies are significantly attenuated as they propagate through the atmospheric air. For example, a 100 kHz sine wave is attenuated by 10 dB after propagating over a 3m distance from the source and by 30 dB for a 10m distance [36][37]. This mitigates the potential hazards posed by the out-band energy of the laser-sound system, although further investigation of this issue is required. In addition, the system entails the risk of skin or eye exposure to intense direct or reflected radiation, which can cause severe health hazards. Such risks need to be addressed in real installations by selecting appropriate beam trajectories and by using beam dumps after the breakdown spot in the air, or appropriately coated non-reflective target surfaces.

The need for high pulse repetition rates, as the one adopted in the simulations of section 6.7 could potentially impose difficulties on the implementation of real laser-sound systems with equivalent specifications, as it results to a pulse-to-pulse time distance of $t_{\mathrm{ptp}} = 2.8\ \mu\mathrm{s}$, while the relaxation time of the thermoelastic phenomenon is usually longer [5][6]. Considering two consecutive laser pulses in such an implementation, the conditions of the air in the focal spot at the moment of arrival of the second pulse, such as temperature, pressure and particle density, will deviate from equilibrium. For even higher laser repetition rates, for example of a few MHz used in common ΣΔ audio formats [28][29], the second pulse would be focused in air plasma, in which case the focusing conditions and light-matter interaction phenomena are much different. Double pulse air breakdown has been studied in several works [38][39], from which it becomes evident that the optical absorption of the second pulse is significantly enhanced, leading to a stronger composite thermoelastic phenomenon. As a result, under such a fast, consecutive excitation, the acoustic behavior of the plasma sound source will deviate from the behavior described here. However, due to the complexity of the phenomenon, in-depth analysis is necessary for the description of the generated sound. In order to avoid this unexpected behavior, several solutions could be adopted, such as:

- the use of ultra-short laser pulses to reduce the duration of the thermoelastic phenomenon,
- rapid pulse-to-pulse micro-shifting of the laser focus to direct each pulse at different positions in the air,
- the use of specially designed solid targets, such as rotating metal disks.

Nevertheless, double- or multi-pulse radiation schemes could also be considered for the shaping of complex sound waves, as well as for the increase of the total efficiency of the optoacoustic transduction.

Conclusions

In this Chapter, a novel laser-driven optoacoustic transducer based on laser-driven plasma generation in ambient air or on metal targets was presented. The laser-sound system achieves controlled reproduction of arbitrary sound signals through an electrical-to-optical-to-acoustic signal transformation chain. In particular, an audio signal encoded as a digital ΣΔ stream is initially transcoded into an appropriately modulated, in time and amplitude, stream of laser pulses, which is subsequently transformed into acoustic N-waves via laser-induced breakdown or laser ablation at the targeted spots.

The hardware structure and signal processing of this prototype experimental platform was described for 1-bit and 3-level digital audio implementations and respective experimental results were presented and analyzed for the reproduction of test signals, particularly sine waves, sine sweeps and speech and music samples. Due to limitations in the repetition rate and energy of the available laser unit, a maximum 4 kHz repetition rate was used for the 1-bit transduction directly in the ambient air, allowing for a ΣΔ oversampling factor of 2 and a 1 kHz effective bandwidth. The 3-level implementation was carried out via laser ablation on metal plates with a repetition rate of 8 kHz and an oversampling factor of 4, leading to the same effective bandwidth.

Moreover, a linear computational model describing the system's functionality as the convolution of the ΣΔ audio stream with the time profile of the laser-generated acoustic N-wave was developed. The experiments and computational evaluations were found to be in excellent agreement and showed that the physical system exhibits a 1^{st}-order high-pass frequency response in the in-band range, due to the spectral profile of the N-wave. The system's impulse response corresponds to an N-shaped pulse with a duration of a few microseconds, while it was shown that it can be equalized by low-pass prefiltering of the input audio signal.

The good agreement between the experiments and the computation model allowed for simulated predictions of a laser-sound system that would not be restricted to the repetition rate of the current experiments. The simulated system was based on a 6^{th}-order 5-bit ΣΔ modulation with x8 oversampling, providing a total 88.57dB SQNR and requiring a laser repetition rate of $352.8\ \mathrm{kHz}$. The system also incorporated appropriate signal pre-processing to achieve an equalized in-band frequency response. The simulations demonstrated that such an implementation would enable perfectly linear optoacoustic transduction with near-ideal transient time-domain and flat frequency-domain responses within the audio frequency range.

The physical, signal processing and energy-related challenges of the laser-sound transducers, such as the hazard of exposure to intense optical radiation and the high-energy ultrasonic emission of the system, were briefly discussed, but should be carefully addressed in the future. Nevertheless, the presented experimental and computational evaluations indicated the feasibility of the evolution of such systems and their suitability to numerous current and future audio applications.

References

[1] Nelson, P., Veyrie, P., Berry, M. & Durand, Y. Experimental and theoretical studies of air breakdown by intense pulse of light. Physics Letters 13, 226-228 (1964).

[2] Raizer, Y. P. Breakdown and heating of gases under the influence of a laser beam, Soviet Physics: Uspekhi. 8(5), 650 - 673 (1966).

[3] Zel'dovič, J. & Rajzer, J. *Physics of shock waves and high-temperature hydrodynamic phenomena*. (Acad. Pr., 1970).

[4] Zhang, Z. & Gogos, G. Theory of shock wave propagation during laser ablation, Physical Review B 69, 235403 (2004).

[5] Harilal, S., Brumfield, B. & Phillips, M. Lifecycle of laser-produced air sparks. Physics of Plasmas 22, 063301 (2015).

[6] Kaleris, K., Orphanos, Y., Bakarezos, M., Dimitriou, V., M., Tatarakis, M., Mourjopoulos, J. & Papadogiannis, N. On the correlation of light and sound radiation following laser-induced breakdown in air, Journal of Physics D: Applied Physics (2020).

[7] Gómez Bolaños, J., Delikaris-Manias, S., Pulkki, V., Eskelinen, J. & Hæggström, E. Laser-induced acoustic point source for accurate impulse response measurements within the audible bandwidth. The Journal of the Acoustical Society of America 135, EL298-EL303 (2014).

[8] Matamura, A., Nishimura N. & Liu, B. Y. Filterless multi-level delta-sigma class-D amplifier for portable applications, 2009 IEEE International Symposium on Circuits and Systems, pp. 1177-1180, (2009).

[9] AN-1497 Filterless Class D Amplifiers, Application Report, Texas Instruments, Dallas (2013).

[10] Kaleris, K., Stelzner, B., Hatziantoniou, P., Trimis, D. & Mourjopoulos, J. Laser-sound: optoacoustic transduction from digital audio streams. Nature Scientific Reports 11, 476 (2021).

[11] Kaleris, K., Stelzner, B., Hatziantoniou, P., Trimis, D. & Mourjopoulos, J. Laser-sound: audio reproduction from digital ΣΔ streams, under review.

[12] Kaleris, K., Stelzner, B., Trimis, D. and Mourjopoulos, J., Vorrichtung und Verfahren zur Wiedergabe mindestens eines akustischen Signals (DE Patent subm. No 10 2021 200 293.5), Deutsches Patent- und Markenamt (DPMA), submitted Jan 2021.

[13] Pavan, S., Schreier, R., & Temes, G. C. Understanding delta-sigma data converters. Hoboken, NJ: Wiley (2017).

[14] Van Ess, D. Signals from Noise: Calculating Delta-Sigma SNRs (Rep.). San Jose, California: Cypress Semiconductor.

[15] Janssen, E., & Van, R. A. Look-ahead based sigma-delta modulation. Dordrecht: Springer (2011).

[16] Oksanen M. & Hietanen, J. Photoacoustic breakdown sound source in air. Ultrasonics 32, 327-331 (1994).

[17] Ghosh, S. & Mahesh, K. Direct Numerical Simulation of the Thermal Effects in Plasma/Turbulence Interaction 45th AIAA Aerospace Sciences Meeting and Exhibit (2007).

[18] Gómez Bolaños, J., Delikaris-Manias, S., Pulkki, V., Eskelinen, J. & Hæggström, E. Laser-induced acoustic point source for accurate impulse response measurements within the audible bandwidth. The Journal of the Acoustical Society of America 135, EL298-EL303 (2014)

[19] Is-series. (n.d.). Retrieved April 05, 2021, from https://www.edge-wave.de/web/en/produkte/short-pulse-systeme/is-serie/

[20] Pockels cells for ELECTRO-OPTIC Q-SWITCHING and modulating. (n.d.). Retrieved April 05, 2021, from http://www.leysop.com/em500.htm

[21] M1000 and M2500 high Voltage amplifiers for driving Pockels cells and other electro optic components from leysop. (n.d.). Retrieved April 05, 2021, from http://www.leysop.com/m1000-m2500.htm

[22] Audacity Team. Web site: https://audacityteam.org/. The name Audacity® is a registered trademark of Dominic Mazzoni.

[23] AURORA acoustic plugins for Adobe Audition. (n.d.). Retrieved April 05, 2021, from http://pcfarina.eng.unipr.it/Aurora_XP/index.htm

[24] B&O, Music for Archimedes. Copenhagen: Hansen and Munch (1991).

[25] IEC 61260-1, Electroacoustics – Octave-band and fractional-octave-band filters (2014).

[26] Kaleris, K., Orfanos, Y., Bakarezos, M., Papadogiannis, N. & Mourjopoulos, J. Experimental and analytical evaluation of the acoustic radiation of femtosecond laser plasma filament sound sources in air. The Journal of the Acoustical Society of America 146, EL212-EL218 (2019).

[27] Farina, A. Advancements in Impulse Response Measurements by Sine Sweeps, AES Convention 122, p. 7121 (2007).

[28] Melchior, V. High-resolution audio: a history and perspective. J. Audio Eng. Soc. 67(5), 246–257 (2019).

[29] Nuijten, P., Reefman, D. Why Direct Stream Digital (DSD) is the best choice as a digital audio format, AES Convention 110, 5396 (2001).

[30] Yoneyama, M., Fujimoto, J., Kawamo, Y. & Sasabe, S. The audio spotlight: An application of nonlinear interaction of sound waves to a new type of loudspeaker design, 73, 1532-1536 (1983).

[31] Pompei, J., Audio spotlight: Sound from ultrasound, Journal of the Acoustical Society of America, 145(3):1714-1714 (2019).

[32] Barnes, N. P. Solid-state lasers from an efficiency perspective. J. Sel. Top. Quantum Electron. 13(3), 435 (2007).

[33] Bakarezos, M., Tatarakis, M., Brezas, S. & Papadogiannis, N. A., Internal Report, CPPL, (2016).

[34] Rossi, M. Acoustics and Electroacoustics, Artech House, Norwood, MA (1988).

[35] Acton, W., Exposure to industrial ultrasound: Hazards, appraisal and control. Occupational Medicine, 33(3), 107-113 (1983).

[36] Stuart, J. R. & Craven, P. A Hierarchical Approach to Archiving and Distribution, proceedings of the 137th AES Convention, 9178 (2014).

[37] Kay, G.W.C. & Laby, T.H., Tables of Physical and Chemical Constants, section 2.4.1, online at NPL, http://bit.ly/1rkaKGv

[38] Papeer, J. et al. Multi variable control of filamentation of femtosecond laser pulses propagating in air. J. Phys. B At. Mol. Opt. Phys. 48, 094005 (2015).

[39] Henis, Z., Milikh, G., Papadopoulos, K. & Zigler, A. Generation of controlled radiation sources in the atmosphere using a dual femtosecond/nanosecond laser pulse. J. Appl. Phys. 103, 103111 (2008).

[40] Eskelinen, J., Hæggström, E., Delikaris-Manias, S., Bolaños, J. & Pulkki, V. Beamforming with a volumetric array of massless laser spark sources-Application in reflection tracking. The Journal of the Acoustical Society of America 137, EL389-EL395 (2015).

[41] Delikaris-Manias, S., Bolaños, J. G., Eskelinen, J., Huhtakallio, I., Hæggström, E., Pulkki, V., Auralization of source radiation pattern synthesized with laser spark room responses. Journal of the Audio Engineering Society, 64(10), 720-730 (2016).

[42] Point, G. Energy deposition in air from femtosecond laser filamentation for the control of high voltage spark discharges, PhD thesis, Laboratoire d'Optique Appliquée, Ecole Polytechnique, Palaiseau, France (2015).

[43] Kaleris, K., Orphanos, Y. Bakarezos, M. Papadogiannis, N., & Mourjopoulos, J. The effect of plasma geometry on the acoustic radiation of laser filaments, proceedings of Forum Acusticum (2020).

[44] Jones, T., Hornstein, M., Ting, A. & Wilkes, Z. Intense underwater laser acoustic source for Navy applications. The Journal of the Acoustical Society of America 125, 2556-2556 (2009).

[45] Hornstein, M., Jones, T., Ting, A. & Nicholas, M. Directivity and frequency control of an intense underwater laser acoustic source for navy applications. The Journal of the Acoustical Society of America 127, 1985-1985 (2010).

[46] Krylov, V. V. Directivity patterns of laser-generated sound in solids: Effects of optical and thermal parameters. Ultrasonics, 69, 279-284 (2016).

Chapter 7

Conclusion

Contents

7.1 Conclusions

This thesis was dedicated to the study of physics and engineering aspects of sound reproduction via massless laser-generated plasma sources. Particularly, it attempted a breakthrough in sound transduction technology by introducing a novel laser-sound system that enables the direct transcoding of pulsed audio streams into acoustic N-pulse streams via laser-induced breakdown in ambient air and laser ablation on metal targets. In this respect, a prototype transducer was experimentally and analytically evaluated at a proof-of-concept level, proving the linear and controlled functionality of potential laser-sound systems in the audible frequency range. Moreover, this work presented new phenomenological models for the estimation of the sound generated by laser-plasma sources in terms of the parameters of the laser radiation, as well as a novel method for the calculation and analysis of the DFT spectrum of Uniformly-sampled Pulse Width Modulation (UPWM) signals derived from random input signals. The ultimate goal of this work is to provide the computational tools and cover the fundamental engineering aspects of an alternative transduction technology that will address the deficiencies of the existing electromechanical transducers by enabling spatial audio reproduction and rendering of moving directional sound sources in holographic audio scenes.

7.1.1 Laser-plasma sound emission

On the physics part, we studied the correlation between light and sound radiation following laser-induced breakdown from tightly focused nanosecond pulses with several tens of millijoules energy, using a combined experimental, analytical and signal processing methodology. We also studied the acoustic radiation of elongated laser-generated plasma threads called plasma filaments.

With respect to light-sound correlation in LIB

LIB light radiative process

From the time-resolved recordings of the emitted light signal, and by considering the light radiative mechanisms and their characteristics, we could identify the constituents of the optical signal's time profile and associate them to their generating physical processes, namely Bremsstrahlung, electron recombinations, de-excitations and thermal radiation. By using signal processing techniques, we obtained an estimation of the time profile of the thermal radiation component.

LIB sound radiation model

The thermal component was used as a heat source in a linear wave equation model that allowed us to estimate the acoustic frequency spectra of the laser-generated acoustic waves. The model could reproduce the spectra of the acoustic N-pulses with satisfactory accuracy for laser pulses with energies of 40, 60, 80 and 100 mJ, clearly demonstrating the correlation between the emitted light and sound signals following LIB. Such a correlation, apart from the fundamental interest, exhibits also practical interest, since the measurement of the thermal radiation is significantly simpler and does not require as specialized equipment as the corresponding acoustic measurements.

Analysis of LIB acoustic spectra

By comparison of the frequency spectra of the N-pulses generated by optical pulses with different energies, it became apparent that an increase in the incoming energy leads to a spectral shift of the acoustic pulse towards the lower frequencies. Moreover, by comparison of the optical signals generated by laser pulses with different energies, it emerged that the increase in optical energy leads to a clear increase in the duration of the thermal phenomenon, namely, longer expansion and collapse times. In turn, the extended thermal phenomenon leads to wider acoustic pulses, which results to the spectral shift towards the lower frequencies.

With respect to the acoustic radiation of plasma filaments

Acoustic line source model

Moreover, we studied the characteristics of the acoustic radiation of laser plasma filaments by developing a simple phenomenological model based on the classical line source model. To imprint the characteristics of the filament in the model, the elementary source excitation was substituted by the pressure profile of the acoustic N-pulse generated by a point-like plasma source, while the initial pressure along the axis of the filament was weighted according to the axial distribution of the filament's plasma luminescence.

Analysis of acoustic directivity and spectra

We also analyzed the acoustic directivity and frequency spectra of a plasma filament experimentally, by measuring the emitted sound with a microphone at different angles with respect to the filament's axis. The filament, in analogy to the classical acoustic line sources, exhibits enhanced acoustic emission in the direction perpendicular to the filament's axis, while in this direction its acoustic spectra resemble the spectra of the elementary N-pulse. By moving towards the filament's axis, the acoustic pressure progressively fades and interference patterns appear in the frequency spectrum. Also, by analyzing the directivity in frequency bands we demonstrated that the filament becomes less directional in the lower frequencies, as expected. Comparison to the evaluations of the model showed that there is very good agreement for both the filament's acoustic directivity and frequency spectra.

Impact of plasma geometry on the filament's radiation

Furthermore, we used the model to evaluate the impact of the geometry of the plasma channel on the emitted sound. Four different filament lengths were considered, 3.5, 7, 14, and 28 cm, along with four axial pressure distributions with Gaussian, Lorenzian and 4^{th} and 6^{th} order super-Gaussian shape. The simulations showed that the length of the plasma channel has a strong impact on the directivity of the acoustic radiation, with the 3.5 cm filament being almost omnidirectional in the audible range (maximum deviation of ~ 3 dB) and the 28 cm filament being strongly directional (maximum deviation of ~ 22 dB). On the contrary, the acoustic radiation showed weak dependence on the pressure distribution, with the smoother distributions (Lorenzian, Gaussian) leading to slightly more directional emission than the steeper super-Gaussians.

Radiation physical model

Finally, we outlined a complete physical model based on the linear wave equation with a heat source and presented preliminary results from the evaluation of a scaled model of the filament. The model proved to be able to accurately capture the characteristics of the filament's acoustic radiation, namely its directivity and typical interference patterns in the spectrum.

7.1.2 Laser-sound optoacoustic transduction

On the engineering part, we designed, developed and evaluated a novel laser-based optoacoustic transducer capable of reproducing continuous complex sound waves via pulsed massless plasma point sources.

With respect to the laser-sound transduction model

Initially, we developed a simple computational model that describes the transcoding of pulsed audio signals into acoustic N-pulse streams through the linear convolution of the pulsed audio stream with the time-profile of a single N-pulse. The model was validated by comparison with experimental evaluations of the real transducer prototype, showing very good agreement. Hence, we showed that such a model can be used for the design and evaluation of any laser-sound system that is based on plasma generation from pulsed lasers and driven by pulsed audio streams.

With respect to the transducer prototype

We have developed a working prototype that is able to transcode digital audio ΣΔ streams into acoustic N-pulse streams. Two distinct implementations of the system were presented:

a. a 1-bit implementation with 4 kHz sampling rate and an oversampling factor of 2, with direct laser-induced breakdown in the air and
b. a 1.5-bit (3-level) implementation with 8 kHz sampling rate and an oversampling factor of 4 with laser-ablation on metal plate

The sampling rate restrictions were imposed by the limitations of the available laser repetition rate, while the need for a metal target in the 1.5-bit implementation was due to the limited laser pulse energy. In both implementations, the ΣΔ audio streams were derived by a 1^{st}-order ΣΔ modulator with either flat or 1^{st}-order high-pass profile of the noise floor, achieving an effective audio bandwidth of 1 kHz and Signal to Quantization Noise Ratios (SQNR) of 21 dB and 24 dB, respectively.

Laser radiation control techniques

We developed a novel method for triggering laser pulse emission by directly routing a pulsed audio stream to the trigger input of the laser unit, through an audio interface. Moreover, we demonstrated that for the multilevel implementations, an electro-optic modulator can be used to modulate the amplitude of the emitted optical pulses in real time.

Prototype performance evaluation

For the evaluation of the transducer, we adopted a parallel experimental and analytical approach by carrying out systematic recordings of the reproduction of test audio signals, and particularly sine waves and sine sweeps. The experimental results were compared with simulations via the simple linear model, showing good agreement, thereby confirming the well-defined, predictable, and strongly linear functionality of the prototype in the effective bandwidth range. Moreover, we analyzed the sine sweep recordings to estimate the prototype's impulse and frequency response, which clearly demonstrated the rapid and linear response of the system.

We also carried out a preliminary investigation of the energy efficiency of the laser-sound system, showing that the main sources of energy losses in the laser plasma sound transduction are the electrical-to-optical energy conversion process of the laser, the imperfect absorption of the optical energy from the medium and the lossy energy transfer from the free electrons to the heavy particles of the ionized medium. In this regard, the prototype's efficiency was estimated at about 0.35%, while it was shown that an optimized system could reach an efficiency of more than 4%, which is the theoretical efficiency limit of the current electromechanical technology.

Simulation of an ideal laser-sound transducer

The experimental validation of the model allowed us to carry out simulations of an ideal high-specifications laser-sound transducer able to perform within the full audible range, based on realistic component requirements. Particularly, a laser unit with 352.8 kHz repetition rate was assumed along with a 6^{th}-order 5-bit pole-optimized ΣΔ modulator with an oversampling factor of 8 and an effective bandwidth of 22.05 kHz. The simulations demonstrated the possibility to perfectly reconstruct the original audio signal from the reproduced N-pulse stream by application of a high-order low pass filter with a 20 kHz cutoff frequency, a process that is naturally done by the human auditory system. Moreover, we demonstrated the possibility to accurately equalize the frequency response of the system by applying a 1^{st}-order low pass filter to the input signal.

7.1.3 Analysis of UPWM DFT spectra

By analyzing the frequency spectra of Uniform-sampling PWM signals, we observed that when the input signal is random (i.e. noise signal) and its samples are independent and identically distributed random variables (iid RVs), the DFT of the UPWM signal in the out-band range only depends on the statistics of the amplitude distribution of the samples. In this respect, we developed a method for the calculation of the UPWM DFT coefficients directly from the statistical moments of the input signal. Particularly, we showed that, given an ergodic generating random process, the random variables obtained via Fourier series analysis of the UPWM signal are unbiased estimators of the true mean of the Fourier coefficients of the UPWM signal. Moreover, we showed that when the samples of the input signal are not independent RVs, only the Fourier coefficients on the harmonic frequencies of the PWM carrier can be derived from the statistics of the generating process. Finally, we also derived analytical closed-form expressions for the Fourier coefficients of UPWM signals originating from input signals following Gaussian, Laplacian, arcsine and uniform distributions.

It was shown that, this method allows for the estimation of the UPWM DFT spectra in the out-band range without knowledge of the particular time-series of the input signal, when the input signal can be modeled using random models. Out-band frequency components of UPWM signals can be This effectively facilitates the design of UPWM systems, since the strong spectrum at the output of the system is such as class-D amplifiers, where an output stage filter is necessary for the suppression of the excessive out-band components.

7.2 Long term vision

Laser-sound could potentially open up new horizons in audio reproduction, as it has several advantages over the established moving-coil electromechanical technology:

a. It enables the unbounded positioning of massless sound sources within the listening space, by focusing the laser beam in the air or on specially coated solid surfaces.

b. The digital ΣΔ modulated bitstreams triggering the laser can be directly demodulated into acoustic waves without the need for digital-to-analog conversion, wired connections and power-consuming electromechanical transduction units.

c. Moving focus techniques, such as moving mirrors, could be adopted for fast shifting of the acoustic source, enabling the real-time rendering of moving sound objects.

d. It is also suitable for remote sound reproduction via transmission and direct demodulation of signals over very long distances, without the need for a local receiver or power supply, as the optical pulse stream carries both the audio information and the power required for the reproduction.

e. The support of direct sound reproduction from digital modulations allows for the implementation of fully digital audio reproduction chains without moving parts.

f. Laser-sound will potentially enable directivity control via virtual volumetric arrays of point-like plasma sources or elongated plasma threads. In contrast to the electromechanical transducers, the in-band frequency response of optoacoustic transducers is well-defined and stable, as the system is free of moving parts and is not subject to constructional or material defects.

g. Moreover, the plasma sources are capable of generating strong broadband impulse-like signals, which are useful in applications where the rendering of rapid sound events is required, as for example in acoustic measurements.

h. Finally, it is anticipated that laser-sound technology can reach or even surpass the current electromechanical technology in terms of power efficiency, which is less than 2% for the direct emission of the typical moving-coil commercial loudspeakers, while the theoretical maximum is below 4% (see also Chapter 6). It is estimated that an optimized laser-sound system can achieve an efficiency higher than 4%, depending on the wall-plug efficiency of the driving laser unit, the optical absorption efficiency and the optical-to-sound coupling. The latter is intrinsic to the optoacoustic transduction and depends on the parameters of the laser pulse, however, there are only few references to the particular dependence in the bibliography and a systematic study should be carried out in the future.

Based on these advantages, the long-term vision of this work is the reproduction of controlled holographic sound via laser-driven spatially unbounded virtual sound sources at varying distances from the optical source, without the need for localized transduction devices. The envisaged laser-sound system will be able to precisely reconstruct any desired sound projection pattern, with sufficient power and well-defined time-frequency acoustic characteristics, making it suitable for future all-digital holographic sound reproduction systems. For the adoption of the technology in end-user applications, there are several obstacles to be overcome:

a. Current state-of-the-art lasers capable of generating breakdown at high repetition rates are costly; however, their price is gradually decreasing due to progress in laser technology and a quick raise in their demand for scientific and commercial applications.

b. Safety issues due to direct or reflected optical radiation from the laser have to be addressed in installations where there is a possibility of skin or eye exposure. Laser beam paths should be directed away from the listeners while beam blockers or specially coated absorptive surfaces should be used to stop the beam to avoid potential reflection.

c. As presented in the simulations of the ideal optoacoustic transducer, for high laser repetition rates the consecutive excitation of the interaction volume before complete relaxation of the thermoelastic phenomenon could lead to acoustic behavior that deviates from the behavior outlined in the presented experiments and model. In this case, the impact of dual or multiple pulse excitation on the generated sound needs to be studied, or the focus of the laser needs to be rapidly shifted for pulse-to-pulse excitation in different spots. Nevertheless, multi-pulse radiation schemes could also lead to an increase in the overall transduction efficiency, since optical energy deposition in a plasma is more efficient than in neutral air, while it also requires significantly lower optical intensity.

d. Strong ultrasounds generated by the laser-sound system in the out-of-band frequency range, although imperceptible by the human auditory system, can potentially cause distress to animals or humans. Thus, the propagation range of such ultrasounds needs to be studied and potential mitigation techniques need to be developed.

Nevertheless, due to its unique and unprecedented capabilities, laser-driven audio reproduction could become a complementary technology, or even an attractive alternative, to the established electromechanical transduction for a variety of commercial applications.

7.3 Future work

During this thesis, several topics related to the physics of laser-induced breakdown and the engineering of laser-sound generation have emerged that require further investigation. A comprehensive list of these topics is provided below.

7.3.1 Physics of laser induced breakdown

Complete light-to-sound computational model

Regarding the physics, systematic experiments on the dependence of the LIB acoustic pulses on the laser radiation parameters, such as duration, wavelength, energy and focusing conditions, have been carried out and a simple computational model has been outlined. In the near future, this model will be completed in order to systematically describe the dependence of plasma-generated sound waves from the laser pulse parameters.

Impact of chirp on femtosecond LIB acoustic radiation

Moreover, preliminary experiments with chirped femtosecond pulses have shown a dependence of the acoustic characteristics of the generated N-pulse, but also of the light-to-sound conversion efficiency, on the amount of pulse chirp. Such a dependence effectively means that the sound generated by breakdown of gases from femtosecond pulses could be fine-tuned via the rearrangement of the optical frequencies within the laser pulse. These findings could potentially be explained by the outlined optical absorption model via the introduction of a spatio-temporal variation of the laser pulse frequency. The ultimate goal of such work is to develop a complete computational model that takes as input the parameters of the optical radiation and the targeted medium (gas, liquid or solid) and gives at the output the time profile of the generated N-pulses in 3D space.

Laser plasma filaments for specialized acoustic measurements

Laser plasma filaments, potentially reaching lengths of several hundreds of meters, constitute unique acoustic sources with special geometrical characteristics, as they approximate one dimensional line sources with near-ideal cylindrical acoustic emission. For this reason, apart from their interest for the rending of directional acoustic objects in a future laser-sound system, they are also useful for acoustics applications, i.e. for the evaluation of acoustic scale models or real-scale listening spaces, focusing on particular surfaces or simulating the acoustic emission of line-array loudspeaker systems.

7.3.2 Laser-sound transducer

Virtual evaluator

A virtual platform is going to be developed for the auditory evaluation of ideal laser-sound systems under realistic working conditions, and particularly the system's:

a. acoustic performance in a large-scale open-air sound installation with real-time rendering of moving acoustic sources
b. potential to transduce sound signals over large distances,
c. technical and safety challenges to be addressed for its adoption in commercial applications.

Such a virtual evaluation system will significantly advance the technical readiness of the laser-sound system without the need for costly experimental installations.

Full audio range transducer

A new prototype will be developed according to the specifications of the simulated ideal laser-sound transducer presented here. It is anticipated that the high-specifications prototype will be capable to precisely reproduce audio signals in the entire audible frequency range.

Alternative audio modulation schemes

The implementation of different modulations schemes, such as Pulse Width Modulation (PWM) or Pulse Amplitude Modulation (PAM) which were presented in Chapter 3, will also be investigated in terms of acoustic performance and efficiency. Particularly for PAM, preliminary experiments have already been carried out with the presented prototype, showing both advantages and disadvantages over the ΣΔ modulation implementation. A block diagram of the system architecture is shown in Fig. 7.1 However, further systematic tests are required to assess the acoustic parameters and reproduction quality of PAM or PWM laser-sound systems.

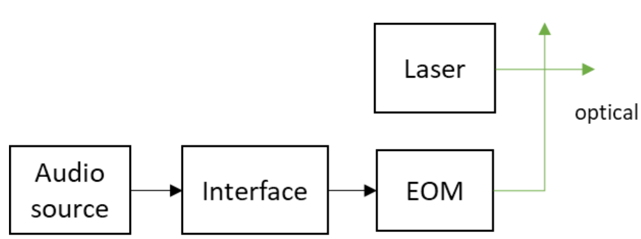

Fig. 7.1: Block diagram of a PAM-driven laser-sound system.

LIB inside acoustic resonators

Finally, the controlled spectral shaping of the laser-generated acoustic signal via the use of enclosures acting as acoustic resonators will be experimentally and analytically studied. Such a system driven by 1-bit ΣΔ streams is shown in Fig. 7.2. As expected, preliminary experiments and simulations performed in the frame of this thesis have shown that the resonator spectrally shapes the acoustic N-pulses in a linear manner, a process that can be described by multiplication of the N-pulse spectra with the resonator's frequency response. Further research has to be carried out to estimate the required resonator geometries and materials for achieving particular acoustic results in the in-band range as well as efficient filtering in the ultrasonic range.

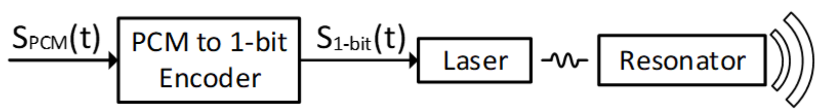

Fig. 7.2: Block diagram of a 1-bit ΣΔ laser-sound system with sound spectral shaping via a resonator.

7.3.3 PWM signals from random inputs

The proposed method for the calculation and analysis of the out-band DFT spectra of Uniform-sampling PWM signals from random inputs could be also applied to analog Natural-sampling PWM signals. Due to their wide adoption in engineering applications, NPWM signals have been thoroughly studied for deterministic input signals and several expressions of their frequency spectra have been presented. However, to the best of our knowledge, the possibility of expressing the spectra of NPWM signals in terms of the statistics of random input signals has hitherto not been examined. Such an approach would significantly enhance the applicability of the proposed analysis method to a wide variety of systems and applications, potentially also to different carrier-based modulation methods.